Efficient Design, Integration and Optimization of Highly Miniaturized Filters for RF/Wireless Applications

von Diplom-Ingenieur
Mohamadou Baba
aus Berlin

von der Fakultät IV - Elektrotechnik und Informatik
der Technischen Universität Berlin
zur Erlangung des akademischen Grades

Doktor der Ingenieurwissenschaften
- Dr.-Ing. -

genehmigte Dissertation

Promotionsausschuss:

Vorsitzender:	Prof. Dr.-Ing. Ernst Obermeier
1. Gutachter:	Prof. Dr.-Ing. Dr. E.h. Herbert Reichl
2. Gutachter:	Prof. Dr.-Ing. habil. Gerhard Mönich

Tag der wissenschaftlichen Aussprache: 20.02.2008

Berlin 2008

D 83

Kurzfassung

Seit den letzen Jahrzehnten verzeichnet der Markt für drahtlose Kommunikationssysteme enorme Wachstumsraten. Dabei ist der Wunsch nach leichten, kompakten, leistungsfähigen und multifunktionalen Geräten der Konsumelektronik immer größer. Zur Erfüllung dieser Forderungen sind viele Forschungsaktivitäten zu höheren Integrationsdichten elektronischer Systeme im Bereich der Systemtechnik sowie der Aufbau- und Verbindungstechnik notwendig.

In Sende- und Empfangseinrichtungen nachrichtentechnischer Hochfrequenzschaltungen werden zahlreiche passive Komponenten für den Entwurf und die Realisierung der Sub-Systeme (wie z.B. Filter, Verstärker, Oszillator etc) verwendet. Hochfrequenz-Filter gehören zu den wichtigsten Komponenten der Sender- und Empfängerschaltungseinrichtungen. Sie werden nicht nur zur Signalsselektion, sondern auch zur Impedanzanpassung verwendet. Viele dieser Komponenten beanspruchen größere Volumina und werden daher diskret realisiert. Durch ihre Integration werden enorme Platzersparnisse und damit auch Systemsminiaturisierung erreicht.

Durch den technologischen Fortschritt auf dem Gebiet der Aufbau- und Verbindungstechnik in den letzen Jahren, insbesondere im Bereich der Multi-Chip-Module (MCM) für System-in-Package (SiP) Technologien, stehen beachtliche Entwicklungen im Hinblick auf die Hochfrequenzschaltungsintegration zur Verfügung. Diese Technologien eignen sich deshalb sehr gut zur Integration von Hochfrequenz-Filtern, wobei Restriktionen zu beachten sind, die sich aus technologisch bedingten Entwurfsregeln bzw. aus der Hochfrequenzschaltungstechnik ergeben.

Im Rahmen dieser Arbeit, wurde eine Methodologie für den Entwurf und die Integration von Hochfrequenz-Filtern entwickelt. Spiralförmige Spulen mit verschiedenen elektrischen Längen wurden entworfen. Durch die Verwendung ihrer Induktivitäten sowie ihrer parasitären Kapazitäten wurden Bandpass-Filter in unterschiedlichen Topologien und Konfigurationen entworfen und in MCM-L für SiP- Technologie integriert. Die Ausnutzung der parasitären Kapazitäten führte zur Reduzierung der Komponenten-Anzahl im Designentwurf und damit zu einer Design-Miniaturisierung.

Für die Design-Implementierung der Bandpass-Filter zweiter Ordnung wurden folgende Design-Topologien und -Konfigurationen abgeleitet: Gap-Topologie, Tap-Topologie, Lateral-Konfiguration, Vertikal-Konfiguration mit Versatz zwischen den Resonatoren und Vertikal-Konfiguration ohne Versatz zwischen den Resonatoren.

Für die Design-Implementierung in Vertikal-Konfiguration ohne Versatz zwischen den Filter-Elementen wurden Fenster in den Metall-Zwischenlagen vorgesehen, um die elektromagnetische (EM) Kopplung zwischen den Filterelementen zu ermöglichen und zu kontrollieren.

Dieser Entwurf und die Integration erfolgt über den intensiven Einsatz von elektromagnetischen Feldsimulationen auf Basis der Momentenmethode (MoM). Die Einflüsse von Design-Topologie/Konfiguration in Hinblick auf die Miniaturisierung sowie Effizienz von Filtern wurden analysiert. Die Design-Implementierung mit Gap-Topologie in Vertikal-Konfiguration ohne Versatz zwischen den Resonatoren zeigte einen positiven Einfluss auf die Filter-Selektivität, aber auf Kosten der Filter-Sensitivität.

Die Einflüsse von technologischen Schwankungen auf die Filter-Charakteristik wurden ebenfalls analysiert. Die Filterbandbreite ist deutlich sensitiver gegenüber Toleranzen der Substratdicke im Vergleich zur Toleranz der Material-Dielektrizitätskonstante.

Auf Basis der entwickelten Methoden wurden Filter entworfen, integriert und optimiert. Für die Validierung der Methoden sowie für die Verifikation der Design- und Modellierungstechniken wurden einige der entworfenen Filter fabriziert und messtechnisch charakterisiert. Eine sehr gute Übereinstimmung der Parameter zwischen gemessenen und simulierten Test-Strukturen wurde erzielt.

Die Design-Integration der vertikalen Konfiguration ohne Versatz zwischen den Filter-Elementen hat ein Miniaturisierungspotential von bis zu 27 % erwiesen ohne deutliche Veränderung der Einfügedämpfung innerhalb des Durchlassbereichs.

Abstract

The emergence of wireless applications due to enormous interest in mobile communication services has caused an ever increasing demand in miniaturized, highly functional and low cost electronic products. One possibility to meet these requirements is the high level integration of many components into a module platform.

In RF circuit blocks of wireless radios, many discrete and off-chip surface-mounted devices such as filters, duplexers, and diplexers still exist and are space-consuming. Integrating these components leads not only to a substantial reduction in board size as well as in weight, but improves also the reliability and decreases the development cost. Therefore, an efficient design concept for their integration is required.

Due to the technological progress in the fields of the integrated circuits (ICs) packaging over the past few years, particularly in the field of the multi-chip-module (MCM) based system-in-package (SiP) technology, considerable developments concerning RF circuit design has been made. Therefore, this technology is well suitable for the integration of RF filters, while restrictions have to be considered, which derive from technologically dependent design rules as well as RF circuitry.

In the framework of this work, a methodology for efficient design and integration of RF filters was developed. The design made use of spiral-shaped microstrip inductors designed with different electrical lengths. By the use of the inductances as well as the parasitic capacitances of these inductors, bandpass filters were designed in different topologies and configurations, and implemented using MCM-L based SiP technology. Using of the parasitic reactance led to a substantial reduction in component count as well as in circuit design size.

For the implementation of second order bandpass filters, the following design topologies and configurations were derived: “gap topology”, “tap topology”, “lateral configuration”, “vertical configuration with off-set between the resonant elements”, and “vertical configuration without off-set between the resonant elements”.

For the filter design implementation in “vertical configuration without off-set between the resonant elements”, ground planes designed with electromagnetic (EM) windows were placed between the resonant elements in such a way to control the EM coupling happening between the resonant elements.

The EM simulations of the filter design structures were performed by means of the full-wave solver “Agilent Momentum” that employs the Method of Moments (MoM) codes for the discretization of the total structures. The impacts of the design topologies/configurations on the filter performances as well as on the circuit design miniaturization were analyzed. The design implementation with “gap topology” in “vertical configuration without off-set between the resonant elements” improved the filter selectivity, but at the cost of the sensitivity.

Sensitivity analyses for the design parameters have been performed in order to predict the impacts of the tolerances (due to the manufacturing process fluctuations) on the filter characteristics. The bandwidth is most sensitive against the substrate thickness tolerances.

Based on this methodology, filters for various applications were designed, integrated and optimized. For the experimental validation of this design methodology as well as verification of the modeling accuracy and analysis method, test samples were fabricated and tested through on-board RF measurements. There was a good correlation between measurement and simulation data.

The design implementation in vertical configuration without off-set between the resonant elements offered a potential of filter size reduction up to 27 % without noticeable performance degradation within the passband.

Acknowledgments

This project was carried out in the Department of System Design & Integration (SDI) at the Fraunhofer Institute for Reliability and Microintegration (FhG-IZM) in Berlin, where I have been working for more than six years.

I would like to express my thanks to Prof. Dr.-Ing. Dr. E.h. Herbert Reichl (head of FhG-IZM) for his supervision and his foresight in identifying this problem as an important research area, and Dr.-Ing. Stephan Guttowski and his team (from SDI), who has approved me working as staff member in the department. I also express a lot of thanks to the entire staff, for their collaboration and understanding.

I would like to express my sincere thanks to Prof. Dr.-Ing. Dr. h.c. Hans-Günther Wagemann from the Technische Universität Berlin (TU Berlin), not only for his supervision, but also for his support and motivation, during my studies of Electrical Engineering at the TU Berlin.

I would also like to thank Prof. Dr.-Ing. habil. Gerhard Mönich from TU Berlin for reading my thesis and serving on my oral examination committee.

It is a great pleasure and honor to express my gratitude to everybody, who supported me in one way or another as I worked through this dissertation.

And finally I wish to thank GOD for giving me the strength, power and knowledge to accomplish this work.

Berlin, November 2007 Mohamadou Baba

In the loving memory of my mother,

Ina Ramatou Danladi, who died on 10th June 1999, and who supported and encouraged me keeping interest on my education.

Contents

Kurzfassung

Abstract

Acknowledgments

Contents

List of Acronyms and Abbreviations

List of Acronyms and Abbreviations

1G, 2G, 3G	First, Second, Third Generation of standards in mobile communication
ACP	Air-Coplanar-Probes
ADC	Analog-to-Digital-Converter
AC	Alternating Current
AMPS	Advanced Mobile Phone System
BCB	Benzocyclobutene
BPF	Bandpass Filter
BWA	Broadband Wireless Access
BW	Bandwidth
BAW	Bulk Acoustic Wave
BiCMOS	Bipolar Complementary Metal-Oxide Semiconductor
CDMA	Code Division Multiple Access
CMOS	Complementary Metal-Oxide Semiconductor
CTE	Coefficient of Thermal Expansion
DAC	Digital-to-Analog-Converter
DUT	Device under Test
DQPSK	Differential quaternary phase shift keying
DCS	Digital Cellular System
DC	Direct Current
DECT	Digital European Cordless Telecommunication
DSSS	Direct Sequence Spread Spectrum.
EM	Electromagnetic
EMI	Electromagnetic Interferences
ESD	Electrostatic Discharge
FR4	Flame Retardant 4 (type 4 glass epoxy)
FDMA	Frequency Division Multiple Access
FBW	Fractional Bandwidth
FSK	Frequency Shift Keying
FDD	Frequency Division Duplexing

FEM	Finite Elements Method
FBAR	Film Bulk Acoustic Resonators
FDTD	Finite Difference Time Domain Method
GFSK	Gaussian Frequency Shift Keying
GMSK	Gaussian Minimum Shift Keying
GSG	Ground-Signal-Ground
GSM	Global System for Mobile communications
HIPERLAN	High Performance Radio Local Area Network (ETSI, Europe)
HFSS	High Frequency Structures
HDI	High Density Interconnect
HPF	Highpass Filter
HTCC	High Temperature Co-fired Ceramic
HPSK	Hybrid Phase Shift Keying
HTS	High Temperature Superconductor
HF	High Frequency
IC	Integrated Circuit
I/O	Input and Output
IF	Intermediate Frequency
ITFS	Instructional Television Fixed Services
IR	Infrared
ISS	Impedance Standard Substrate
IL	Insertion Loss
I/Q	In-phase and Quadrature
ISM	Industrial, Scientific, and Medical
IS 95	Interim Standard 95
LCP	Liquid Crystal Polymer
LNA	Low Noise Amplifier
LO	Local Oscillator
LTCC	Low Temperature Co-fired Ceramic
LRM	Line-Reflect-Match
LRRM	Line-Reflect-Reflect-Match
LPF	Lowpass Filter
MESFET	Metal-Semiconductor Field-Effect Transistor
MIM	Metal-Insulator-Metal

MoM	Methods of Moments
MCM	Multi Chip Module
MCM-C	Multi Chip Module Ceramic
MCM-D	Multi Chip Module Deposited
MCM-L	Multi Chip Module Laminate
MMDS	Multichannel Multipoint Distribution Service
MEMS	Micro-Electro-Mechanical Systems
N.N.	Nomen Nominando (der Name ist noch zu benennen)
OFDM	Orthogonal Frequency Division Multiplex
O-QPSK	Offset Quadrature Phase Shift Keying
PCS	Personal Communications Services (U.S.)
PCN	Personal Communications Network (Europe)
PDC	Personal Digital Cellular (Japan)
PCB	Printed Circuit Board
PACS	Personal Access Communication System
PTFE	Polytetrafluoroethylene
PWB	Printed Wiring Board
PA	Power Amplifier
PHS	Personal Handy Phone System (Japan)
QPSK	Quadrature Phase Shift Keying
RF	Radio Frequency
RL	Return Loss
RX	Receiver
Rx	Receive
SoC	System-on-Chip
SiP	System-in-Package
SMT	Surface Mounted Technology
SOLT	Short-Open-Load-Thru
SF	Shape Factor
SAW	Surface Acoustic Wave
TDMA	Time Division Multiple Access
TDD	Time division duplexing
Tg	Glass transition temperature
TE-	Transverse Electric

TEM-	Transverse Electromagnetic
TM-	Transverse Magnetic
TRL	Thru-Reflect-Line
TLM	Transmission Line Matrix
TX	Transceiver
Tx	Transmit
TX/RX	Transceiver/Receiver (or Transmitter)
Tx/Rx	Transmit/Receive
U-NII	Unlicensed National Information Infrastructures
U-ISM	Unlicensed Industrial, Scientific, and Medical
UMTS	Universal-Mobile-Telecommunications-System
UHF	Ultra-High Frequency
VHF	Very High Frequency
VLF	Very Low Frequency
VSWR	Voltage Standing Wave Ratio
VNA	Vector Network Analyzer
W-CDMA	Wideband Code Multiple Division Access
WPAN	Wireless Personal Area Network
WLAN	Wireless Local Area Network
WWAN	Wireless Wide Area Network
Wi-Fi	Wireless-Fidelity
WiMAX	Worldwide Interoperability for Microwave Access
WCS	Wireless Communication Service

Chapter 1

Introduction

1.1. Motivation

The fast-growing wireless market with the emergence of new wireless standards has created an increasing demand for multi-band and multi-standard base-station/mobile-handsets products with increased functionality and performance, while still meeting the requirements of smaller, lighter and cheaper.

These new standards, which set these requirements, involve more complex designs of RF transceiver circuits, where many passive components are intensively used for building of active devices such as amplifiers, oscillators, as well as for building of passive devices like filters.

Filters are required to perform different functions like impedance matching or RF signal selection. Examples of filters in RF front-ends are pre-select filters, and image-reject filters. Image-reject filters are responsible for the rejection of the image signals, which are unwanted signals generated by the mixer and other components. Pre-select filters are needed for the selection of desired frequency bands while at the same time elimination of any undesired signals that may be present at the antenna's output at much higher power levels. These pre-select filters are often realized as duplexer, which serve to separate transmit signals from receive signals, which lie in an adjacent frequency band. Without these duplexers, the strong transmit signal would leak into the receiver section and saturate the low-noise-amplifier (LNA), making therefore the receiver to lose sensitivity to the weak receive signal. Generally, most of these passive components are realized as discrete components and therefore occupy more space.

Integrating these passive components leads to a substantial reduction in board size as well as in weight. This is the main focus in this work. Integrated passive filter components can be realized in embedded form. There are many different definitions for this term over the literatures. Based on the definition given by Ulrich and Schaper [1.1], the integrated passive filters in this work are filters whose structures are housed inside the layers (ML1, ML2, ML3, etc) of the first interconnect substrates (PCB), which give them the sub-designation of embedded passive filters.

Other advantages related to the embedded passive filters are improvement of electrical performance and reliability, as well as reduction of development cost.

Many different RF/wireless technologies are available, which can be used for the integration of RF/microwave filters.

Due to the technological progresses in the fields of semiconductor technologies over the past few years, particularly in the field of silicon technology, considerable development concerning RF circuit design has been made. RF circuits can be integrated using RF system-on-chip-(SoC) technology. Despite the advantage of its maturity, this technology is still too expensive for products with shortened life-cycle. Therefore, the market trends show that RF system-in-package (SiP) technology is the preferred technology to implement RF transceiver modules (e.g. RF front-ends). This technology provides a quicker development cycle and cost-effective design development.

Thus, the development of more integrated passive modules in SiP technology can be seen as the market trends over the coming years, and with the ever increasing requirements for higher miniaturization and higher volume integration, the market for surface mount technology (SMT) will be shrinking.

Therefore, to prevent system manufacturing, RF filters for signal pre-selection must be efficiently designed. So far, a variety of methods has been used to design and integrate these RF filters. However, the majority of these methods used up to date leads to the development of space-consuming and expensive filters. Consequently, the requirements needed for highly miniaturized and cost-effective RF/wireless systems cannot be met.

1.2. Goal and Structure of the Work

The main goal of this work is the development of a design methodology that leads to the integration and miniaturization of RF filters for wireless applications. To reach this goal, following approaches are used:

(1) Filter design: The filter consists of coupled inductors, the structures of which are designed with rectangular-shaped spiral line of physical length θ equal to π or $\pi/2$, depending on the design topology. The inductor length is related to the filter center frequency that is approximately equal to the inductor self-resonance frequency. These inductors are capacitively coupled to each other, and are realized with inductive or capacitive input/output-ports. They provide inductances as well as parasitic capacitances due to the inter-turn and ground plane effects. These parasitic capacitances, in addition to the capacitances resulting from the inter-inductor coupling, make up the overall required electric energy. Thus, using of these parasitic reactances leads to a substantial reduction in components count as well as in overall design size.

(2) Design analysis: Electromagnetic (EM) field simulations are performed using quasi-static and full-wave solver in order to determine more accurately and faster the RF behaviors of each filter design structure. Different EM field solvers are employed in combination in order to realize the maximum advantages of competitive analysis, in solving Maxwell's equations, and determining the EM field scatterings within the structures under test. Circuit models of each filter structure as well as methods for the extraction of model parameters are developed.

(3) Technological implementation: For the illustration of this novel design methodology, filters for various applications are developed and implemented in a low-cost multi-chip-module laminate (MCM-L) technology.

(4) Design optimization: The impacts of the tolerances due to the manufacturing process fluctuations on the filter performances are studied. The impact of the design topologies and configurations on the filter characteristics are also investigated.

(5) Fabrication and test: Test structures with adapters that represent the interface between probe-tips and devices-under-test (DUT) are developed for the verification of the design approach as well as the accuracy of the modeling method.

This dissertation is organized as followed. Chapter 2 outlines the state-of-the art in the design and integration of RF filters for wireless applications. The methods used for the design and modeling of these filters, as well as the technologies used for their integration are described. Chapter 3 exposes the novel design methodology, which is illustrated in Chapter 4 through the implementation of different RF filters for various wireless applications such as Wi-Fi and WIMAX. The impact of the tolerances as well as the design topologies and configurations on the filter characteristics are exposed. The approach used for the design downscaling is also presented in this chapter. Chapter 5 outlines the experimental characterization of the test samples through RF measurements. Finally, the last chapter summarizes the results of this work.

Chapter 2

State-of-the Art in the Design and Integration of RF/Microwave Filters

2.1. Wireless Communication Systems and Circuits

The most common wireless communication systems (e.g. cellular telephones) guide information by modulating the electromagnetic (EM) wave through different EM spectra such as radio frequencies (VLF, LF, HF, VHF, UHF, L-band, and S-band), microwaves (3 to 30 GHz), or millimeter-waves (30 to 110 GHz).

From the 1st generation (1G) of mobile phone up to the 3rd generation (3G), there has been an emergence of new wireless technologies. The transmission of voice and data happens in different areas, which can be categorized mainly into [2.1] wireless wide area networks (WWAN), wireless metropolitan area networks (WMAN), wireless local area networks (WLAN), and wireless personal area networks (WPAN). Each area is distinguishable through its distance of operation and data transfer rate.

Wireless voice can be transmitted through digital cordless systems using different standards [2.2] such as DECT (880-1900 MHz), PHS (1895-1918 MHz), PACS (1850-1910 MHz, 1930-1990 MHz), or through digital cellular systems using different standards like IS-54/136 (869-894/824-849 MHz), GSM (935-960 MHz / 890-915 MHz), PDC (940-956 MHz / 810-826 MHz), DCS1800, DECT, PCS1900, etc., while wireless data communication rely on existing analog cellular networks (e.g. cellular network modems), or digital cellular systems whether cordless or cellular.

Frequency spectrum licensed for use by 3G systems falls roughly in the 800 MHz to 900 MHz range, in the 1700 MHz to 1900 MHz range, and in the 2500 MHz to 2700 MHz in most world regions [2.2]. Although many different 3G mobile phone technologies exist worldwide, the most competing ones are W-CDMA/UMTS (wideband code multiple division access / also known as universal mobile telecommunication system), CDMA2000 (code division multiple access). Table 2.1 & 2.2 give an overview for some important communication network technologies for 2G and 3G cellular phone operation [2.2]-[2.5].

In personal- and local-area, most of the wireless products have air interfaces that use low-power RF spread spectrum technology operating in the unlicensed industrial scientific and medical (ISM) bands, though there are also some products, which use licensed spectrum ranges [2.3]. The operation distance covered in WPAN, WLAN, WMAN, and WWAN is 0–10 m, 10–100 m, 100–1000 m, and 1–10 km, respectively. For the most products, the data rates are up to 1 Mbps (for WPAN, and WWAN), 50 Mbps (for WLAN), and 80 Mbps (for WMAN).

Table 2.1 Wireless communication technologies for WPAN and WLAN Standards

Area	WPAN (0–10 m, up to 2.4 Mbps)		WLAN (10–100 m, up to 54 Mbps)	
Standard and market name	802.15.4 ZigBee	802.15.1 Bluetooth	802.11a Wi-Fi	802.11b/g Wi-Fi
Operation frequency	2.4 GHz	2.4 GHz	5 GHz	2.4 GHz
Tx/Rx spectrum	2402–2480 MHz	2402–2480MHz	5250–5350 MHz 5725–5825 MHz	2400–2483 MHz
Modulation	QPSK	GFSK	GFSK	BPSK/ QPSK
Data rate up to	0.25 Mbps	1 Mbps	54 Mbps	11 Mbps/ 54 Mbps
Range up to	20 feet (6 m)	30 feet (10 m)	100 feet (30 m)	300 feet/100 feet (100 m / 30 m)
Application	Cable replacement	Cable replacement	LAN, Internet	LAN, Internet
Tx-power (max.)	Low power 200 mW	Medium power	High power 5 W	High power 5 W / 1W

Table 2. 2 Wireless communication technologies for WMAN, and WWAN Standards

Area	WMAN (0.1–1 km, up to 80 Mbps)		WWAN (1–10 km, up to 2.5 Mbps)	
Standard / Market Name	802.16d WiMax (fixed)	802.16e WiMax (portable)	3G CDMA2000	3G W-CDMA/UMTS
Operation Frequency	2–11 GHz	2–6 GHz	0.8GHz / 0.9GHz/ 1.8GHz / 2 GHz	1.8 GHz / 2 GHz / 2.5 GHz
Tx/Rx spectrum		2400–2600 MHz		1920–1980MHz (Tx) 2110–2170MHz (Rx)
Modulation	OFDM	GFSK	OFDM	HPSK
Data Rate	Up to 75 Mbps	Up to 30 Mbps	Up to 2.4 Mbps	Up to 2.4 Mbps
Range	Typically 4–6 miles	Typically 1–3miles	Typically1-5miles	Typically 1–5 miles
Application	Cable replacement	Cable replacement	Voice, video, multimedia	Voice, video, multimedia
Tx-Power Output (max)	High power	Low power 10mW	Medium power	High power 600–3000 mW

2.2. Architectures of Wireless Transceivers

Transceivers are examples of wireless circuits. Figure 2.1 shows the photography of a wireless transceiver for mobile cellular operation (voice and data).

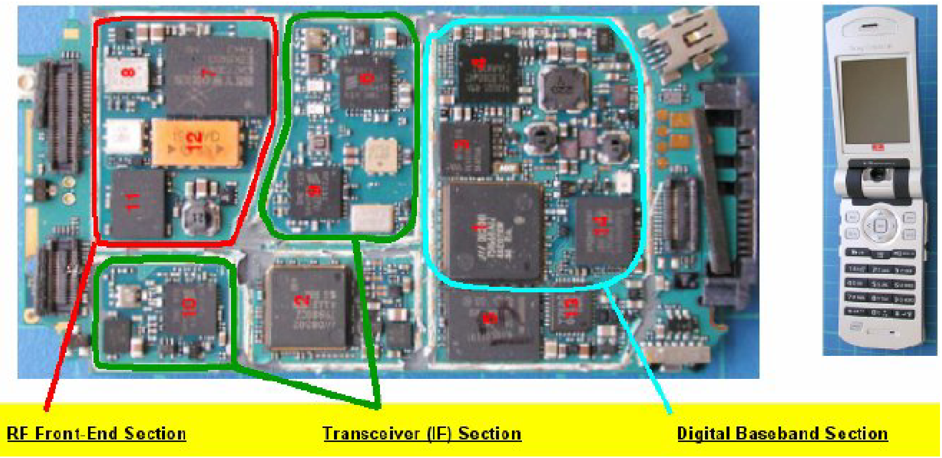

Figure 2. 1 Sony-Ericson wireless phone transceiver as illustration of a wireless circuit [2.3]

The basic function of transceivers is to perform the bidirectional transfer of information between the baseband processor and the antenna. There are two types of RF transceivers: full-duplex and half-duplex. In a full-duplex transceiver, the transmitter and receiver operate simultaneously. An AMPS analog cellular phone is a good example. In a half-duplex system, such as GSM, either the transmitter or the receiver may be on in a time slot.

Transceivers consist in transmit and receive chains. On the transmit chain, analog voice is digitalized and analog to digital converted using ADCs. The digitalized voice and data are coded and compressed. After that, redundancy is added through the channel coding process. The next step in the transmit chain is the encryption of the coded interleaved bit stream. The final compressed, error-protected, encrypted bit stream must then be modulated in the format defined by the appropriate standard. The modulated bit stream in the transmit chain is then back converted to the analog domain using a pair of DACs (one each for I and Q). The final stage of the transmit chain includes an RF modulator, which must convert the baseband I and Q signal up to the appropriated carrier frequency for a cellular system that will be on the order 2 GHz for UMTS system, for example. This up-converted signal is then amplified by a power amplifier, passed through the antenna switch / duplexer and finally transmitted from the antenna.

On the receive mode, the signal is passed through the duplexer/switch and down-converted using one or more mixing stages before it is demodulated into baseband I and Q components. The number of mixing stages depends on the architecture, which is used (whether heterodyne or homodyne). The remainder of the receive path consists of relatively straightforward implementations of the reverse processes described for the transmitter including decryption, channel decoding and de-interleaving, voice decompression (or decoding), and digital-to-analog conversion to drive the handset speaker. Each of these chains consists in many subsystems such as filters, amplifiers, mixers, and oscillators.

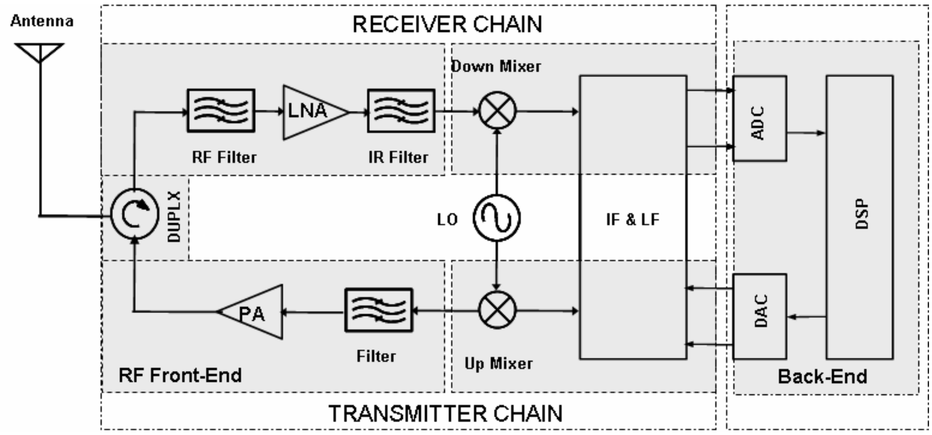

Figure 2. 2 Simplified block diagram of a cellular phone

Figure 2.2 shows an example of a cellular phone block diagram that may be divided into different subsystems (e.g. RF front-end section, IL & LF sections, and back-end section). In the analog RF front-end section for instance, many passives are intensively used in building of active devices, as well as in building of passive devices. These passive elements constitute more than 50 % of the components ranging from simple resistors, capacitors, and inductors to surface mounted matching circuits, high-frequency components for RF and IF filtering, such as SAW filters, antenna switches/duplexers. These components constitute a significant portion of the actual and related costs in today’s implementation of wireless terminals.

Different transceiver architectures are available. These are generally classified into homodyne, heterodyne and mixed architectures, depending on the conversion mode. An overview of some existing receiver architectures is given in the following.

2.2.1 Heterodyne Receivers

Heterodyne receivers (also called super heterodyne) are widely utilized for current wireless applications. Historically, heterodyne was the first practical receiver architecture implemented for cellular phone systems. A block diagram of a heterodyne receiver with two frequency translation steps is illustrated in Figure 2.3.

In this architecture, the signal received at the antenna is first filtered before being amplified by a low-noise amplifier (LNA) (e.g. by 10 to 20 dB). The signal is then further filtered by an image-reject (IR) filter before being frequency translated to an intermediate frequency (IF) by the first local oscillator (LO). At the IF stage the signal is further filtered by an IF filter and amplified before being frequency translated to base-band. Two parallel signal paths, in-phase (I) and quadrature (Q), are obtained at base-band after two-step frequency translation. Finally the I and Q signals are further amplified and filtered by low-pass filters, respectively, before being converted to digital signals by the analog-to-digital converter (ADC).

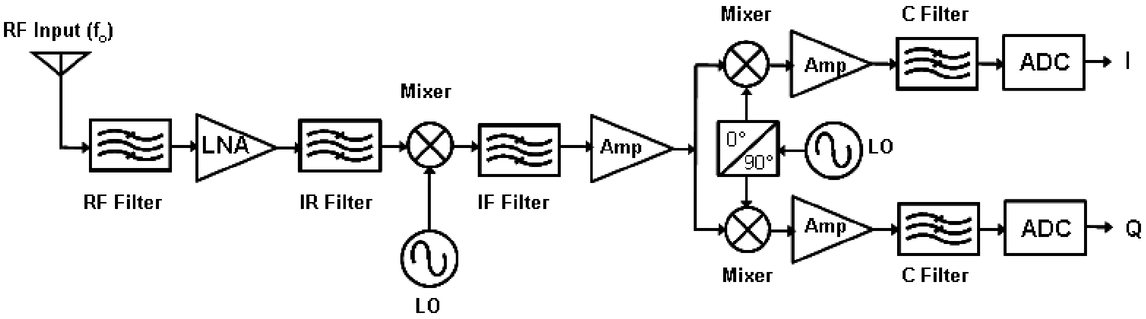

Figure 2.3 Heterodyne receiver architecture

Heterodyne receivers are popular due to their high selectivity and excellent sensitivity with low power consumption. The requirements of filters are not tight and the risk of oscillation for the receivers is reduced, since the gain is distributed to several frequencies. However, the multiple stages of filtering with discrete components are required. The extra filtering in heterodyne arises from the image problem due to a real sinusoidal LO used in the first step of the frequency down-conversion. The need for a large number of external components (e.g., IF filter) complicates the high level of integration [2.6].

2.2.2 Homodyne Receivers

In homodyne receivers (also called direct conversion receivers, or zero-IF receivers), the signal is downconverted directly to the baseband. There is no IF stage and, thus, the structure is simpler and more suited for high integration than the heterodyne receiver.

The direct conversion architecture has the advantage of low power consumption (since the RF signal is downconverted to baseband directly) and minimal component count; this architecture is suitable for multi-standard applications. The channel filtering can be implemented both in the analog domain and in the digital domain (at the baseband). Another advantage of this architecture is that there is no image reject problem, since no IF exists before the input signal is translated to baseband.

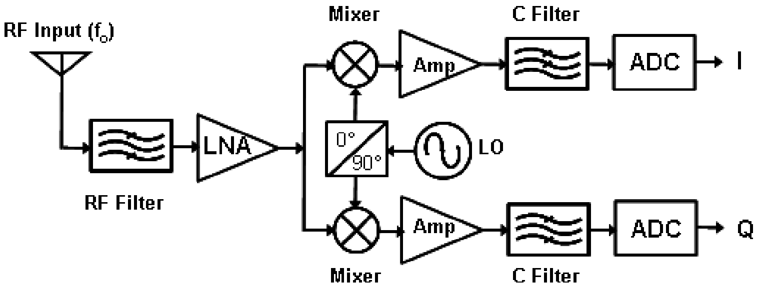

Figure 2. 4 Homodyne receiver architecture

However, several problems such as DC-offset and flicker noise are associated with these direct conversion architectures. The DC-offset is the most critical problem, which would degrade the receiver performance significantly without careful consideration. There are many sources of DC-offset problems. One of them is the LO self-mixing. Due to the imperfect isolation between the LO and the RF port of the mixer, the LO signal can couple to the RF signal path and mix with itself, and thus resulting in a DC component (DC-offset).

In addition to the DC-offset problem, flicker noise caused by active components within the receiver chain may also degrade the receiver performance, especially in narrow bandwidth systems such as GSM.

2.2.3 Image-Reject Receivers

In each heterodyne receiver, an image-reject filter is used to suppress the image problems. However, the requirements imposed on this filter are very tight (very high Q-factor, higher steepness) making its integration difficult. The image-reject architectures can be used in order to ease the design of the receiver while providing image-rejection. There are different realizations of image-reject receivers and one of them, the Harley architecture [2.7], is shown in Figure 2.5.

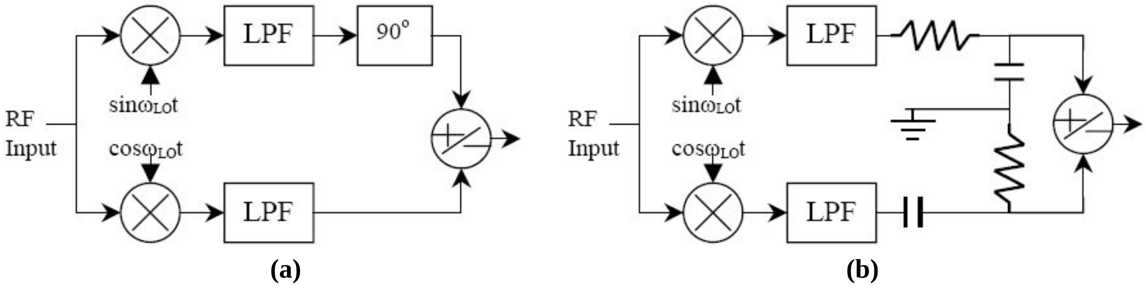

(a) (b)

Figure 2. 5 a) Harley architecture and b) typical implementation

In image-reject receivers, the RF signal is first mixed with quadrature phases of the local oscillator (LO) signal. After filtering both mixer outputs with a low-pass filter, one of the resulting signals is shifted by 90°. Therefore, the sum of the two final signals cancels the image band to yield the desired signal, while the subtraction removes the desired band and selects the image.

The main drawback of this architecture is that the receiver is very sensitive to the phase errors of the local oscillator signals [2.6], which causes incomplete image cancellation. Also, in the typical implementation of the Harley architecture as shown in Figure 2.5 (b), mismatches of the R and C in the two signal paths due to process variations affects the image cancellation process.

2.2.4 Low-IF Receivers

A low-IF receiver is presented in Figure 2.6. The architecture is a mixed-architecture and combines the good properties of image-reject receivers and the zero-IF receivers. In low-IF receivers the input signal is first down-converted using I/Q mixing, thus effectively avoiding the image problem (i.e. signal and image do not convert to the same frequency). The image and any other unwanted signals are then attenuated by a complex bandpass filter.

In this architecture, IF is non-zero and is much lower than in the conventional image-reject receiver. The low intermediate frequency (usually below 1 MHz) facilitates the use of low-frequency/low-power circuit structures, which are more suitable for the full integration of transceivers than the circuit structures of the image-reject receivers. Furthermore, the amplification and filtering can be done in the baseband, and the DC-offset problem is thereby eliminated by converting the RF signal to a low IF (instead of directly to baseband) which is AC coupled.

The DC-offset and 1/f noise problems posed by zero-IF architecture can be overcome with this low IF architecture.

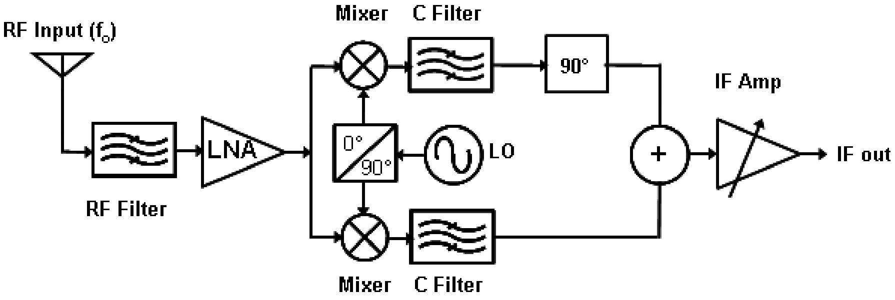

Figure 2. 6 Low IF architecture

Unfortunately this places the (undesirable) image frequency very close to the desired signal which implies critical RF front-end filtering. To overcome this image problem the design implements an integrated image-reject mixer by using I/Q mixing followed by a summer, effectively cancelling the image frequency instead of using off-chip components to filter it. This approach has proven to be very popular in low-cost highly integrated transceivers (including Bluetooth).

Whichever of these architectures is employed in design of wireless transceivers: the receiver must be sensitive and selective. It must be able to detect even a weak signal among many other, possibly stronger signals. Therefore a good receiver must have an accurate local oscillator frequency, good low noise amplifiers, and first of all, very good filters.

2.3. Functions of Filters in Wireless Circuits

Filters are very important components of telecommunication systems. They are required to perform different functions like impedance matching or signal selection. Although similarities exist between impedance matching circuits and filter circuits just by looking at their schematics, there are distinct differences between these functions.

2.3.1 Filters for Impedance Matching

In RF systems the optimum power transfer is one of the important design considerations. The power transfer needs to be maximized from one system block to another. This is achieved by means of matching networks. Matching networks are some type of electrical interconnections that are required between each building block. They are realized using strictly reactive and lossless components in order to achieve power conservation and to achieve usable gain from the active device (transistors) at microwave frequencies. Figure 2.7 shows an example of such filter structures used as matching network in the design of a dual-band power amplifier [2.8] consisting of two stages of MESFET transistors.

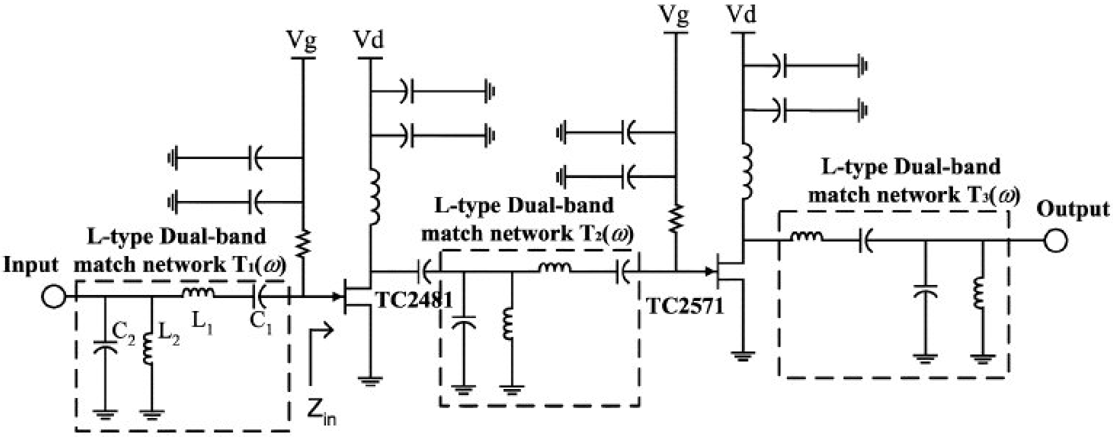

Figure 2. 7: Dual-band power amplifier consisting of two stages of MESFET transistors using filer structure as matching network [2.8]

Impedance matching is more flexible and allows a creative designer to specify the topology. For example, if one needs to match a load impedance of $Z_L = (R_L + jX_L)\Omega$ to $Z_0 = 50\ \Omega$ within a narrow frequency band, one can virtually get the same performance by using a highpass or lowpass circuit configuration. While the passband performances are very close for both circuits, the out-of-band performances are significantly different.

2.3.2 Filters for Signal Selection

The functions of filters in wireless circuits are mostly to reject the unwanted signal frequencies, while permitting a good transmission of the wanted ones. Depending on the circuit requirements, these filters can be designed as lowpass, highpass, bandpass, or bandstop.

For the optimal operation of transceivers the isolation of both the transmitter and receiver have to be very large (e.g. 120 dB).The isolation between both the chains can be done using a duplexer (filter consisting of two bandpass circuits), or a switch. Switches are mechanical, electrical, or electronic devices that open or close circuits, complete or break an electrical path, or select paths or circuits. The losses of a switch are usually less than those of a duplexer.

Filters in a transmitter chain are needed to meet the output noise requirements of the transmitter, since in some cases the transmitter noises can leak into the receiver via the duplexer and destroy the receiver sensitivity. The technology of choice for filters preceding the power amplifier (PA) is SAW. For output duplexers, ceramic Bandpass filters are also used. Ceramic filters have lower insertion loss and thus have less detrimental effect on the transmitter efficiency.

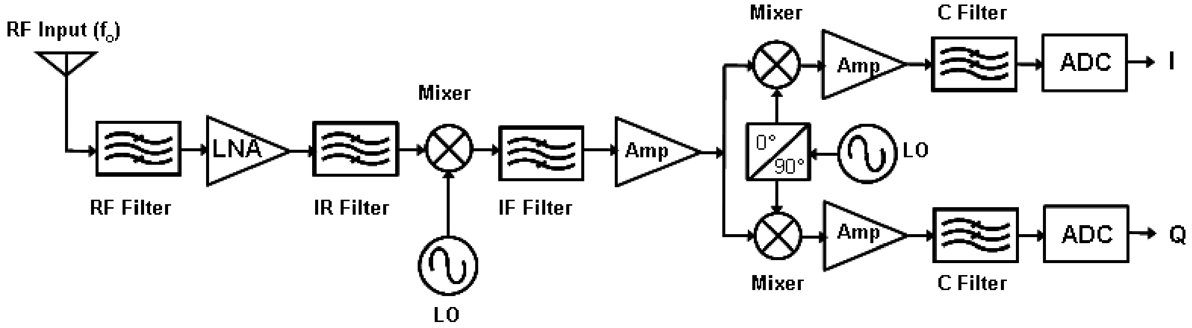

Figure 2. 8 Filters located at different stages in a receiver circuit chain to perform various functions

In receiver chains, many different filters are used (as illustrated in Figure 2.8) to perform various necessary functions. These functions are explained in the following.

RF Preselect Filters

The purpose of RF preselect filters in receivers (RF Filter in Figure 2.8) is to select the desired frequency band to be received, and to eliminate any undesired signal. These filters are typically realized in the form of a diplexer or duplexer. Duplexers connect the antenna to the transmitter (Tx) and receiver (Rx) and provides isolation between the Rx and Tx chains. These filters protect the receiver from saturation by interfering signals at the antenna and determine the receiver selectivity. Without the duplexer, the strong transmitted signal would leak into the receiver section and saturate the low-noise-amplifier, causing the receiver to lose sensitivity to the weak receive signal. Diplexers connect the antenna to a dual band transceiver and allow one frequency band to pass between the antenna and transceiver (e.g., connection of a GSM800- and PCS1900- dual band transceiver with antenna).

Ceramic coupled-resonator filters are commonly used for front-end receiver filters or duplexers. Lower-cost discrete LC filters are also used, especially in half-duplex transceivers where strong interference from the system's own transmitter is not an issue, and thus lower out-of band rejection is acceptable.

Image Reject Filters

Image-reject filters (IR Filter in Figure 2.8) placed after the LNA are used to protect the RF mixer from out-of band interferer signals as well as to reject the undesired signals, generated by the RF mixer and other components. Without image rejection filtering, any signal present at the image frequency will be downconverted to the same intermediate frequency (IF) and will corrupt the desired signal.

The bandwidth of IR filters, centred at the carrier frequency (f_c), must be sufficiently wide to pass the modulation sidebands in the desired channel without distortion. The image frequency has to be suppressed by at least 10 dB in order to meet the system noise figure (NF) [2.7]. To meet the system requirements, RF receivers generally need about 65 dB of image rejection. SAW filters are typically used to provide image rejection. Low-cost LC filters can also be used at the expense of lower rejection levels.

Intermediate Frequency (IF) Filters

Intermediate frequency filters (IF Filter in Figure 2.8) are designed to receive the entire RF passband and to reject spurious frequencies and image frequencies in particular. These IF filters narrow in and select the desired channel from the entire passband; they provide thereby additional selectivity to the receiver. These filters help to prevent out-of-channel noise and help to minimize the loss, thus improving the sensitivity of receivers.

SAW filters are the components of choice for most IF filter applications. They provide the best out-of-band rejection at reasonable size and cost. Crystal and LC filters can also be used at the expense of lower performance.

Baseband Channel Filters

In baseband sections of wireless transceivers, filters for signal selection are required, e.g. anti-aliasing filters located before the A/D converter (C Filter in Figure 2.8) and reconstruction filters after the D/A converters. These kinds of filters are generally lowpass and remove the unwanted channels appearing at higher baseband frequencies, after downconversion. These filters are typically realized on-chip using silicon- or GaAs-technologies, for example.

As can be seen throughout this section, many filters are required in wireless transceiver circuits, and particularly in the analog RF section. Since many of these filters are discrete or surface-mounted, integrating them will lead to a substantial reduction in board size as well as in weight. For a successful integration however, efficient design and analysis methods are required. The contributions made so far are discussed in the next section.

2.4. Filter Design Structures

Microstrip RF/microwave filters can be designed using lumped elements LC structures, or using distributed resonant structures. These design techniques are presented as follows.

2.4.1 Inductor Design Structures

The key building blocks of lumped-element filters are inductors and capacitors. Such filters are realized through the series and/or parallel connection of L and C. The ability to accurately design and model these inductors and capacitors for accurate values is the key for the development of modern RF and wireless circuits.

Inductors can be designed in different layouts, such as straight-line, meander-line or spiral-line. The spiral-line can be circular, octagonal, hexagonal, or rectangular shaped. The use of one or any other layout depends on the electrical performances that must be obtained as well as the ease of the realization. Figure 2.9 illustrates an example of a spiral square-shaped inductor layout.

Figure 2. 9 Inductor layout with spiral square shape

Enormous efforts have been invested around the world in the design and analysis of inductors with the objective of increasing their performances per chip area [2.10]-[2.16].

Loop and meander shaped inductors are simple and easily to be realized. The most advantage of these layouts is that the technological efforts are lower (since only a single metallization layer process is required). However, inductors realized using these kinds of layouts, are limited to applications, where lower inductance values (up to 1 nH) are required. Furthermore, meandered layouts can contribute to the decrease of the total inductance value, since the current in adjacent tracks flowing in opposite directions can lead to a significant decrease in the overall inductance values.

For applications, where higher inductance values are required, inductors designed using various spiral shapes have been intensively employed in multilayer integration technologies [2.14]. One of the metal layers, usually the bottom, is used for the underpass, and the connection between the spiral and the underpass is made by the vias in the dielectric layer.

2.4.2 Capacitor Design Structures

There are various design layouts for integrated capacitors [2.21]-[2.24], the most important used in analog RF design are the interdigital and metal-insulator-metal (MIM) layouts. Figure 2.10 shows the design of a capacitor with interdigital layout.

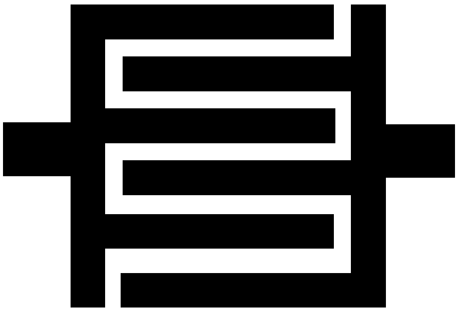

Figure 2. 10: Capacitor design with interdigital layout

Interdigital capacitor designs comprise of a number of thin parallel conducting strips inter-linked alternately to give a total of the capacitor structure. The maximum capacitance value is limited by the physical size, and the maximum useable operating frequency is limited by the distributed nature of the fingers. This layout is limited for capacitance values up to 1 pF, and even a 0.5 pF interdigital capacitor will measure approximately 400 x 400 µm² [2.22]. Nevertheless, since interdigital capacitors do not use dielectric films, they have a very good capacitance tolerance. Hence they are ideal candidates for tuning, coupling and matching, where small capacitance values are required and precise values are necessary.

By far the most popular layout of capacitors is the metal-insulator-metal (MIM) structure. MIM capacitors are formed by sandwiching a layer of dielectric with relative dielectric constant ε_r between two metal plates. It is mostly used for designing LC filters for RF/microwave applications [2.23]. The important design parameters of MIM capacitors are the metal plate area (A), and the dielectric thickness (d). MIM capacitors provide the largest capacitance value per unit area, due to the very thin dielectric layer sandwiched between the metal electrodes. Capacitance values can be determined by $C = A\varepsilon_0\varepsilon_r/d$, where the C-values are ranging between 0.1–20 pF [2.22].

2.4.3 Resonator Design Structures

Transmission line resonator design structures consist in a combination of multi-lines of at least one quarter guide wavelength. Using these structures, filters components with different filtering characteristic can be realized. Various design structures for RF/microwave filters are available [2.9], [2.25], and the most popular include end-coupled, edge-coupled, interdigital and hair-pin filters. Figure 2.11 shows filters designed with end-coupled, parallel-coupled, interdigital, and hair-pin structures.

Research activities worldwide made so far in the design of wireless filters using resonator design structures are reported in [2.9, 2.25, 2.26, 2.31, and 2.33].

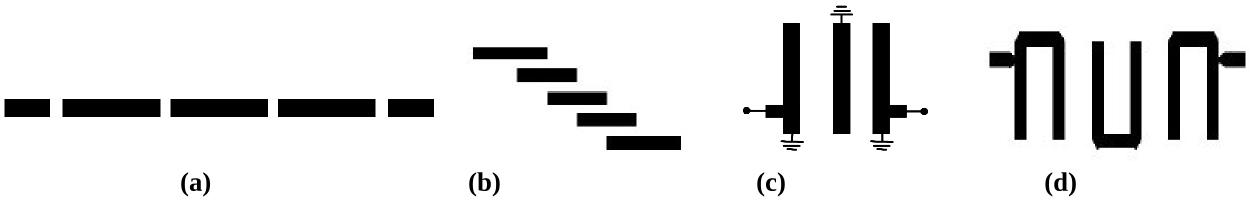

Figure 2. 11 Example of bandpass filter design structures a) end-coupled, b) edge -coupled, c) interdigital, and d) hairpin lines

End-Coupled Lines

End-coupled line filters consist of open-end microstrip resonators of approximately a half wavelength long. The resonators are coupled to other ones through gap-spacing. This layout has been used in the design of bandpass filters. But it has the disadvantage of being space-consuming.

Edge-Coupled Lines

Edge-coupled (or parallel-coupled) line filters [2.25] consist of half-wavelength resonators arranged so that adjacent resonators are parallel to each other along half of their length. The parallel arrangement gives relatively large coupling for a given spacing between resonators, and thus, this filter topology is particularly convenient for designing wide-band filters in comparison to the coupled-end filter topology, described above. Filters based on this topology have been intensively studied e.g., the 7.5 x 7.5 mm^2 bandpass filter [2.26]. The draw-backs of this design lie mainly in the larger dimensions that it occupies.

Interdigital Lines

These filter design structures consist of parallel-coupled quarter wavelength lines, which alternate between the short- and open-circuited ends, as shown in Figure 2.11.c. Generally, the physical dimension of the resonators can be different (different line width/length). The resonators are separated each other by a spacing S. Taped lines with a characteristic impedance Z_t, which may be set to equal the source/load impedance Z_0, are used at input/output of the filter.

Interdigital filters find most applications at higher microwave frequencies above 8 GHz or so, especially for broad bandwidths [2.9]. Interdigital filters have the advantage of perfectly arithmetical symmetry, compared to filters with other design structures like combline design structure. Such symmetry gives better phase and delay characteristics, and it is simpler to design linear phase filters which use cross coupling between nonadjacent resonators.

Hairpin-Lines

Hairpin line filters consist of folded parallel coupled half-wave resonators into a “U” shapes (see Figure 2.11.d). In this design, the orientation of the hairpin resonators alternates, causing the electric and magnetic couplings to tend to add, and thus resulting in maximum coupling for a given spacing between resonators [2.30]. Many other papers about these designs have been published (e.g., [2.31-2.33]). Although this layout is desired for most RF/microwave applications, however, it is very poor for the case of wide band filters, since for this purpose very large spacing between resonators will be required.

Thus, a lot of work has been made, so far in the design of filters using different design structures. These examples were succeeded by means of rigorous design analysis. Various analysis methods have been employed, and the next section presents the most important ones of them.

2.5. Modeling and Analysis Techniques

Filter dimensioning is one of the very important steps in the development processes. It requires rigorous analysis that accounts for all high frequency phenomena like coupling effects, skin-/ proximity effects, higher modes interactions, dispersion, etc. A set of modeling and analysis tools must be efficiently chosen for a successful design.

The techniques of modeling and analysis can be grouped into circuit and electromagnetic (EM) analysis. In circuit analysis, the quantities of interest are mostly the scalar quantities such as currents and voltages, while in electromagnetic analysis the quantities of interest are mostly the vector quantities, like magnetic fields and electric fields. These different techniques are presented as follows.

2.5.1 Circuit Network Analysis

Circuit network analysis is the starting point in many development processes of filter design, and it enables the analysis of the circuit networks, the optimization of the circuit topology, and the investigation of the circuit network parameter variations (since parameters fluctuations can occur during the design realization).

In circuit analysis, equivalent circuit models of filter structures are built using basic elements such as L, C, and R, while in circuit optimization, the effect of parameter variation (sensitivity) on circuit behaviors is studied, which enables the prediction of circuit performances.

The disadvantage of circuit analysis is that the high frequency effects (like coupling, interaction of higher order modes, dispersion, etc) can not be accounted for. Therefore, electromagnetic analysis must absolutely be applied to overcome these drawbacks.

2.5.2 Electromagnetic Analysis

Electromagnetic analysis is very important in the development of RF/microwave filters. Various electromagnetic analysis methods are available and each of them has its advantages and disadvantages. These methods can be classified in different ways.

Depending on the domain of solution, the time domain and frequency domain analysis are distinguished. The frequency domain (or time-harmonic) methods enable the study of the structures in a limited broadband, while the time domain (or transient) methods have the advantage of analyzing the structures in a wide broadband. Many frequency-domain codes are available, e.g., methods of moment (MoM), finite elements method (FEM), etc. Likewise, many time-domain analysis methods are available, e.g., the finite difference time domain method (FDTD), the transmission line (TLM) method, etc. These methods can also be classified depending on the structure that they can handle, for instance, 3D, 3D-planar (or 2.5D), 2D structures. Additionally, in all structures, the distinction between time domain and frequency domain formulations can also be made:

The 2.5D methods are methods for solving problems where the fields depend on three space dimensions, while their source (the current) are mainly confined to a plane with two space dimensions. The 2.5 algorithms mesh (or subdivide) the surfaces of planar metals. With these methods an arbitrary number of homogenous dielectric layers are allowed, and an arbitrary planar metal pattern can then be placed at the interface between any pair of dielectric layers. The interlayer connections are formed by the vias, and this is where the half dimension comes from in the 2.5D description. One is somewhere in between a strictly planar structure and a completely arbitrary 3D structure. MoM is generally used to handle these types of structure. The numerical effort is generally higher compared to 2D methods.

The 3D methods are methods for solving problems where the fields and source functions depend on three space dimensions. These codes mesh a 3D volume. The more popular volume mesh codes employ the FEM, and FDTD methods. Although the volume mesh codes can solve a very broad range of problems, its drawback is the larger time needed for the analysis. It typically takes longer to setup and run a 3D problem compared to a surface meshing or cross-section problem.

Among all these numerical algorithms, MoM, FEM, and FDTD are very popular and are therefore described in the following: MoM is based on an integral form and solves Maxwell’s equations for current surfaces. The integral function is then discretized in basic functions, whose matrices are solved numerically. This method uses Green functions for the approximation and analysis of the structures. The method analyzes 3D conductor structures, but provides results for horizontal current distribution. It is implemented in tools such as Agilent Momentum, or Sonnet. The most Advantage of MoM is its analysis speed. FEM is one which fully analyzes any 3D arbitrary structure. This method performs volume meshing and solves the field and current quantities in horizontal and vertical axis-directions. FEM is implemented in a commercially available tool such as Ansoft HFSS. The most advantages of this tools is that it has the ability to account for high frequency effects in conductor structures as well in dielectric structures, since volume meshing can be performed. However, when very high accuracy is required, the analysis time and the computation memory size can be very large, which could be inefficient for the aspect “time to market”. FDTD analyses any arbitrary 3D structure. The structure is exited by an excitation impulse signal and the electromagnetic quantities are given in time domains as results. These results are obtained in frequency domains by applying the Fourier transformation (FT). FDTD is implemented in a tool such as CST Microwave Studio. The most advantage of this tool is its computation speed, and its broadband analysis at one time. More details concerning all these techniques are given in [2.36]-[2.38].

2.6. On-Chip Integrated RF/Microwave Filters

2.6.1 On-Chip Integrated Passive Filters

There are different design techniques that can be used for the integration of RF/microwave filters. Design techniques such as MEMS, HTS, or SAW, etc. can be used for the implementation of passive on-chip filters. Figure 2.12 shows the classifications of the on-chip realization techniques [2.39].

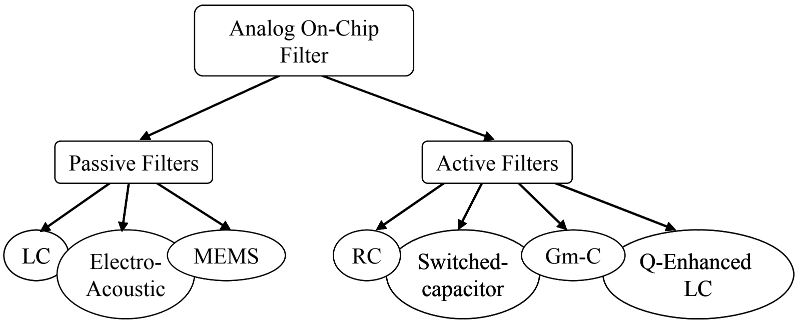

Figure 2. 12 Taxonomy of on-chip filter design realizations

LC Filters

Wireless filters designed on-chip using LC components have the advantages of small size and mass, low-cost in mass production, and high reliability. Due to the technological progresses in the field of semiconductor technologies over the past few years, particularly in the field of silicon technologies, considerable developments concerning radio frequency circuit design have been made. For instance, high performance bandpass and lowpass filters using lumped capacitors, inductors and transformers were successfully realized using a 0.4 µm SiGe BiCMOS process on 2000 Ω-cm silicon, and reported in [2.40]. In this publication, a 1.9 GHz BPF has been designed using three-inductors and a single transformer, while a 1.7 GHz LPF has been designed using a high-Q inductor and metal-insulator (MIM) capacitor. Eisener et al. [2.41] reported a successfully implemented lumped element transmitter bandpass filters for GSM and PCN/PCS applications with a passband insertion loss of 1.45 dB. And quite recently, a 2.4 GHz lowpass and a 5 GHz high-pass passive LC filter were successfully realized on high resistive silicon substrate for WLAN transceiver [2.42]. Designing and integrating narrowband BPF for wireless applications remains, however, the major challenge due to the substrate and metallization losses. Enormous efforts have been invested in novel design techniques such as to reduce or eliminate these losses.

Different methods of reducing substrate losses were investigated [2.56]-[2.57]. Pattern ground shields (PGS) [2.20] were introduced in inductor design in order to impede the penetration of the EM-fields into the semiconducting substrate. Although PGS eliminates the eddy current losses, it increases at the same time the parasitic capacitances which reduce the operation frequency range of the device. Furthermore some technical processes used to get the above mentioned reduction of substrate losses do not belong to the standard silicon technologies. The eddy current losses in standard processes can also be reduced by increasing the dielectric thickness between conducting metal loops and silicon substrate as well as by using high resistive silicon substrate in designing on-chip passives [2.56]-[2.57].

Conductor losses are other issues to be overcome, when designing high-Q on-chip passive components. These losses can be reduced by replacing the traditional aluminum metallization by copper or gold metallization, stacking of many metallization layers such as to obtain a thick metal layer, and many others. Recently, a record quality factor of about 13 for an 10 nH inductor on conventional 5 Ω-cm silicon substrate was demonstrated using a novel metallization add-on module, called "Saddle add-on metallization (SAM)" [2.48]. Although great improvement is obtained, this approach can be costly and is therefore not the viable solution for low-cost applications.

High Temperature Superconductor (HTS) Filters

The reduction of conductor losses has also been investigated by means of the HTS technique. Indeed, using superconducting film materials [2.49]-[2.55], instead of conventional conductor films material, can reduce substantially the component losses. Although great improvement can be obtained, however, the drawback of this approach is the operating temperature, named critical temperature that is limited to approximately below 100 Kelvin. Furthermore, for alternating current (AC) flow, the resistance of the HTS material does not go to zero below the critical temperature. This HTS material resistance increases with increasing frequency, hence, limiting this technique to low power application.

MEMS Filters

The substrate losses can also be reduced using MEMS technique [2.58]-[2.67]. Indeed, high quality passive on-chip components are realized by using micromachining techniques to remove the substrate partly underneath the inductor loops. This results in a substantial reduction of the substrate eddy current losses due to the less penetration of the magnetic fields into the semi-conducting substrate. Although this technique has the ability to enhance greatly the performance of passive components, however, this option is mechanically less stable, and is not preferred for the subsequent packaging.

Electro-Acoustic (On-Chip SAW) Filters

A monolithic integration of electro-acoustic filter structures on semiconductor substrate is also highly desirable to minimize the outer dimension of cellular phone. On-chip electro-acoustic filters can be grouped into two major categories: Bulk acoustic wave (BAW), and surface acoustic wave (SAW) devices. In the literature, BAW devices usually refer to either thin film resonators (TFRs) or film bulk acoustic resonators (FBARs) in order to emphasize their construction and crystal resonator-like behaviour.

A great deal of effort has been investigated in alternative possibilities of implementing passive filter structures on-chip using electro-acoustic techniques, e.g. [2.68]-[2.73]. On-chip surface acoustic wave filters have been reported [2.68]. These filters were based on resonator structures, and were designed on ZnO/GaAs structures. The ZnO film had an optimized thickness of 1.7mm, the thickness of the substrate material (GaAs), and the electrodes material (titanium and gold) were 16 nm and 64 nm, respectively. These filters offered a low insertion loss and a bandwidth of 25 MHz in the 900 MHz frequency range. But, the stopband attenuation (~6 dB) was poor, which could be improved by increasing the number of the resonator structures. In [2.69], silicon-integrated SAW filters using a ZnO- SiO_2-Si layered structure were reported. The piezoelectric

ZnO layer enabled the generation and detection of surface acoustic waves by using aluminum interdigital input/output transducers, located at the ZnO- SiO_2 interface.

The drawback associated with SAW integration techniques are the additions and/or modifications of technology processes; and relatively large chip areas are required. Furthermore, there are some limitations in performance such as the decrease of RF power handling with increasing frequency, limitations in maximum frequency and robustness, and modest power handling and ESD sensitivity.

Fortunately, some of these issues can be overcome by using FBAR integration techniques, which offer the advantages of:

- robustness at frequencies up to 10 GHz,
- ability to handle very reasonable power levels up to several Watt without the need for exotic metallization schemes,
- appropriateness for frequency bands above 800 MHz (because the technology offers excellent Q-values up to 1500), and
- lower temperature coefficients (lower than in SAW filters).

2.6.2 On-Chip Integrated Active Filters

On-chip active filters make use of active components and can be realized using various design techniques including RC, switched-capacitor (SC), transconductor-capacitor (Gm-C), and Q-enhanced-LC (QE-LC) design techniques.

RC Active Filters

RC active filters are filters based on operational amplifier (op amp-RC) resonators obtained by replacing the inductor L in the LC resonator with an op amp-RC circuit that has an inductive input impedance [2.22]. This design can be realized using different op amp circuit configurations. This RC active filter circuit approach has two properties that make its production in monolithic IC form difficult, if not practically impossible; these are the need for large-valued capacitors and the requirement of accurate RC time constants. An alternative design that is more natural to the IC implementation is the switched-capacitor filter design technique.

Switched-Capacitor Filters

Switched-capacitor (SC) filter design technique is based on the realization that a capacitor switched between two circuit nodes at a sufficiently high rate is equivalent to a resistor connecting these two nodes [2.22].

In all cases, active filter based on RC and SC design techniques are difficult to be realized at low power and above few MHz, due to frequency response limitations and parasitic poles associated with the operational amplifiers on which they are based [2.39]. And whenever, which of the both techniques is used for their realization, these filters have a limited dynamic-range [2.39]. But, other useful approaches such as transconductor-capacitor and Q-enhanced filter design techniques can be used for the integration of wireless filters.

Transconductor-Capacitor Filters

Transconductor-capacitor (Gm-C) filters are active filters in which no inductors are needed. Such filters have no parasitic poles and can achieve operation at RF frequencies of hundreds MHz and above. Unfortunately, the performance of such filters in radio applications is limited by technological factors (such as low quality factor and small fractional bandwidth) as well as fundamental factors (such as insufficient dynamic range performance at low power: the dynamic range is the ratio of peak signal voltage before compression to integrated noise-floor voltage) [2.39]. In spite of these limitations, many papers have been published about wireless radio designs using this filter design approach. Andreani et al. [2.75] reported a CMOS Gm-C IF filter for Bluetooth applications. The analog IF bandpass has been implemented with the Gm-C technique, where each inductance is replaced by a gyrator and capacitance. In [2.74], a fully integrated 900 MHz CMOS wireless receiver with on-chip RF and IF Filters and 79 dB image rejection has been presented. The 70 MHz channel-selection IF filter was constructed with three Gm-C biquads in cascade. Another approach used to realize high performance RF on-chip active filters is the Q-enhancement technique.

Q-Enhanced-LC Filters

The most popular approach to design high performance on-chip active filters for wireless applications is through the Q-enhanced-LC (QE-LC) filter design technique, which makes use of negative resistance to boost the quality factor in a lossy LC tank [2.76]. The negative resistance consisting in active components compensates for the effects of passive component losses on passband insertion loss and frequency selectivity.

So far, on-chip active filters based on QE-LC design technique have been investigated around the world and the most contributions made up to date are published in [2.77]-[2.84]. In [2.78], a 3-pole Chebyshev BPF employing on-chip passive elements with Q-enhancement technique was designed to achieve an insertion loss of 0 dB and a passband of 60 MHz around the center frequency of 2140 MHz. The Q-enhanced technique was based on a coupled-inductor negative resistance generator. In contrast to conventional negative resistance generators, this technique compensated the resonator losses without introducing distortion in the filter response in the passband. This filter, which was fabricated in a 0.25 μm CMOS process, consumed 7 mA from a 2.5 V supply and occupied an area of 1.3 x 2.7 mm².

Clearly, for their small size, the on-chip active design techniques are very attractive. But the drawbacks associated with these active filter designs, such as the need for automatic frequency- and Q-tuning, poor noise figures, instability and nonlinearity would make them unlikely to be used for applications such as RF band preselections, where high power and low noise are important. These drawbacks can be overcome by using embedded (off-chip) integration technologies, which are discussed in the next section.

2.7. Off-Chip Embedded RF/Microwave Filters

One of the competing packaging technologies in today’s electronic packaging is the multi-chip-module (MCM) integration technique. This approach, which is very important for system-in-package (SiP) integration, offers a promising platform for packaging of integrated circuits and associated subsystems. This technology enables the integration of the RF front-end wireless circuits with high performance RF filters.

The major advantages of MCM technologies over individually packaged chips are [2.85]:

- Higher packaging efficiency (area of chips to area of board), due to the fact that the bare chips can be placed much closer together than the chips in single packages,

- Better electrical performance, due to the shorter distance between chips and hence, reduction of substrate wiring length,
- Greater reliability, due to the reduction of the number of interconnects between the chip and the board,
- Lower cost (in high volume), because of the elimination of the individual IC packages and the reduction of substrate size.

The most important forms of MCM substrates are: organic laminated multilayer board structures (MCM-Ls), thick-film or co-fired multilayer ceramic (MCM-Cs), and multilayer thin-film structures on semiconductor or ceramic base layer, with deposited metal conductors and dielectrics (MCM-Ds). Each of them has its place in RF/microwave technologies and can be used for the embedding of high performance wireless filters.

2.7.1 MCM-L Embedded Filters

Technology Description

The organic multilayer multi-chip-module laminate (MCM-L) technology is derived from organic PWB fabrication, and it uses copper, nickel, and gold metal traces separated by fibre-glass-reinforced organic laminates (commonly), with plated through-holes or vias interconnecting the layers. For the integration of RF components, this technology is the least expensive of the three major MCM technologies, but it provides the lowest density, a poor dimensional and electrical stability of laminate materials with both temperature and humidity, and a high coefficient of thermal expansion (CTE).

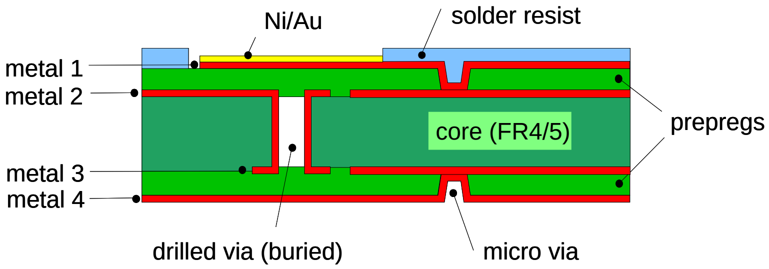

Figure 2. 13 Cross-section of a typical MCM-L substrate

Figure 2.13 shows a typical MCM-L substrate, which consists of a core substrate laminated with thin organic multilayer prepregs on either side of the core. Prepreg is a shortform expression for "pre-impregnated" fibers. It is fiberglass impregnated with a polyimide, epoxy or other resin system, which has been partially cured during the coating operation. These layers are used to separate conducting layer in a multilayer circuit board [2.85].

The core layer contains buried vias; and the prepregs contain blind vias. The both top and bottom side of the board can be connected by through-vias. The number of substrate layers can be varied up to about 10 layers. Typical minimal values of line width and space (differing for different manufacturers) are 25-75 µm. The minimal via diameter is about 100-150 µm. The minimal substrate thickness is 50-150 µm depending on the basic material, and the minimal line thickness is 15-20 µm. These typical values are summarized in Table 2.3.

Table 2.3 Typical design measures for MCM-L substrates

Minimal design values of FR4 substrates				
Number of layers	Via size	Line width/space	Line thickness	Dielectric thickness
10	100-150 μm	25-50 μm	15-20 μm	70-150 μm

The most important MCM-L material parameters that are critical for the performance of RF/microwave circuits are the dielectric constant (DK), dissipation factor (DF), coefficient of thermal expansion (CTE), and thermal conductivity (TK). Gold, nickel or copper metallization layers are usually used in the MCM-L technologies. The number of substrate layers can be varied up to about 10 layers. Typical parameter values for a FR4 material are given in Table 2.4.

Table 2.4 Typical properties of MCM-L substrates

FR4 substrates				
DK	DF	Metallization	CTE in (x, y, z)-directions	TK
3.5-5.0	0.02-0.03	Cu/Ni/Au	14-20 (x, y), 50-70 (z)	1-2 (W/mK)

Filter Design and Integration using MCM-L Technology

Enormous efforts have been investigated in designs and integration of RF filters and the most contributions made so far, are documented in [2.86]-[2.95]. In [2.86], a dual-band filter with excellent loss performance for WLAN applications in ISM 2.4–2.5 GHz and UNII 5.15–5.85 GHz frequency bands has been reported. This filter was based on the novel “dual behavior resonators” technique. The insertion loss and return loss at the central frequency were -2.4 dB and -15 dB for the 2.4 GHz band, respectively, and -1.8 dB and -10 dB for the 5 GHz band, respectively. The filter size was 8 x 15 mm² and it has been fabricated using the LCP based multilayer packaging technology. The LCP substrate has been characterized by a dielectric constant of 2.9 and a dissipation factor of 0.002. The LCP substrate and conductor thickness were 275 μm and 9 mm, respectively. The drawback of this design is that it occupied much size, since it was based on planar lateral coupled resonator design technique. In [2.23], several filters based on lumped element components (LC) for WLAN applications have been realized and characterized. A 2.4 GHz LPF (realized using two embedded inductors and 3 capacitors) was designed in organic laminated FR4 substrate. The filter insertion loss was better than -0.5 dB in the pass-band with 2^{nd} and 3^{rd} harmonic rejection better than -33 dB and -45 dB, respectively. The filters size was 1.8 x 2.6 mm². Although excellent performance was obtained, this filter realized with lumped elements design technique needed too many components, and this is its disadvantage.

Weng et al. [2.91] have presented a dual-band BPF design using an inexpensive commercial FR4 GD (glass-epoxy double-sided) substrate. The proposed BPF was centred at 11.3 GHz, with a fractional bandwidth of 14 %, and an insertion loss of -2.7 dB. It was designed in a low-cost quasi-micromachined and laminated multi-chip-module (MCM-L) technology, with a substrate thickness of 0.4 mm and original relative dielectric constant of $\varepsilon_r = 4.4$. The ground plane thickness was 0.2 mm; the thickness of the FR4 layer and of the supported layer was 0.4 mm. In spite of the miniaturized dimension, the electrical performance could be improved, by the use of low loss dielectric material.

Recently, Gye-An Lee et al. have presented a compact filter and duplexer design using L-shaped multilayer spiral inductor resonators [2.94]. The dimensions of this filter were 1740 x 1740 μm^2. This design has presented an excellent miniaturization potential. However, the methods used for the dimensioning of this filter are missing in this publication.

Chuang [2.95] presented a dual band microstrip filter using a single set of open loop resonators. The dual-bands centered at 1 GHz and 2.2 GHz presented a bandwidth of 50 MHz and 115.6 MHz, respectively. It was designed and fabricated on an FR4 substrate with εr of 4.2 and a thickness of 0.8 mm, with dimensions of about 2.1 x 4.9 mm^2. The only disadvantage of this resonator filter design technique is its larger size.

Despite the technological advances made so far in the integration of RF/microwave filters in the organic MCM-L technology, the incessant growing telecommunication market with increasing new wireless applications involves new products with ever growing needs of miniaturization. MCM-L technology has proved its potential of lower cost implementation of RF/microwave filters. The lack of higher packaging density is its major drawback, the MCM-C integration technology, discussed in next section, can be used to overcome this disadvantage

2.7.2 MCM-C Embedded Filters

Technology Description

The MCM-C technology is based on three different ceramic substrates: thick film multilayer (TFM), high temperature co-fired ceramic (HTCC) and low temperature co-fired ceramic (LTCC).

In TFM technology, the multilayer is processed serially, layer by layer. Each layer is printed and fired separately at 850-1000 °C. In HTCC and LTCC technologies the process is carried out in a parallel way and all foils are co-fired in a single step by building a multilayer structure. The main difference between HTCC and LTCC is the material of the foil and the firing temperature. HTCC foils consist of alumina and are fired at 1600-1800 °C in hydrogen atmosphere. Only W and Mo can be used as conductors because of the high firing temperature. LTCC foils are made from alumina filled glasses or glass ceramic material. The foils are co-fired at 850-1000 °C. The most promising for the future is the LTCC technology [2.96].

LTCC structures consist of dielectric foils, external and internal conductors, surface and buried passive elements, thermal and electrical conductive vias. Additional circuits and elements are added on the top of the structure using various assembling methods. LTCCs have a number of advantages over other MCM-C structures. Co-firing at 850 °C enables to use typical thick film materials and processing. Higher conductivity metals such as gold, silver or copper replace tungsten or molybdenum used in HTCC modules.

A great advantage of LTCC technology is that the basic ceramic foil can be modified to give dielectric materials with different electrical and physical properties. The dielectric constant can be varied in a wide range from 4 to 12. The coefficient of thermal expansion can be adopted to match alumina, gallium arsenide, or silicon. Further advantages of LTCC technology are lower $\tan\delta$ and better controlled dielectric properties (ε_r, $\tan\delta$ and thickness), higher integration and packaging density, and higher performance electronic packaging, design flexibility and reliability, cost-effectiveness for realization of high-Q RF/Microwave components due to the higher dielectric constant and lower dielectric dissipation factor.

Obviously, there are also disadvantages associated with LTCC technology and amongst those is: shrinkage. However, with well-controlled processes, the shrinkage can be kept within a narrow window. During the firing process there is tape shrinkage of between 12-16 % occurring in the X and Y dimensions and slightly more in the Z one.

Table 2.5 Typical properties of MCM-C substrates

Material Parameters	Thick film	LTCC	HTCC
DK	9-10	9	5
DF at 1 MHz	0.004	0.001-0.01	0.001-0.01
Metallization	Au, Cu, Pd, Pt-Au, Pt-Ag	Au, Cu	Mo, W
CTE (10−6/K)	7.1	7	3-5
TK (W/mK)	26	15-20	1-5

The dielectric constant (DK), the dissipation factor (DF), the coefficient of thermal expansion (CTE), and the thermal conductivity (TK) are the most important material parameters which are critical for performance of RF/ microwave circuits. Typical parameter values for MCM-C substrates are given in Table 2.5.

Gold or copper metallization layers are usually used in the LTCC technologies, since the co-fired temperature is below the melting point of these conductor materials.

Depending on the basic material, the coefficient of thermal expansion of LTCC substrate lies between (3−5).10-6/K, the dielectric constant is between 5−10, and the dissipation factor is between 0.001 and 0.01. Low loss is desirable for the transmitted and received signals, whereas a low dielectric constant is important for high-speed signal processing. Also, high insulation resistance and dielectric strength are desirable.

Table 2.6 Typical design measures for MCM-C substrates

Minimal design values of LTCC substrates				
Number of layers	Via size	Line width/space	Line thickness	Dielectric thickness
30	200 µm	70-125 µm	15-20 µm	75-150 µm

The number of substrate layers can be varied up to about 30 layers. Typical minimal values of line widths and spaces (differing for different manufacturers) are 75-125 µm. The minimal diameter of the vias is about 200 µm. The minimal thickness of substrate layers is70–150 µm depending on the basic material. The minimal metallization thickness is 15–20 µm. The typical design measures of LTCC substrate are given Table 2.6.

Filter Design and Integration using LTCC Technology

Enormous efforts have been invested worldwide in the design of RF/microwave filters using LTCC technology, and the most contributions made up to date are reported in [2.97]-[2.101]. A dual-band BPF centered at 2.4 and 5.2 GHz has been designed [2.97] using multilayer LTCC substrate, "Dupont 951", which has a dielectric constant of 7.8 and a layer thickness of 1.7 mil and 3.6 mil. This filter was designed using semi-lumped element structures, and had presented a fractional bandwidth of 8.1% and 5.7% with minimum insertion loss of -3.15 dB and -3.9 dB, respectively. Its total filter dimension was 106 x 70 mil². Likewise in [2.98], a dual-band BPF using stepped impedance resonators with hairpin configuration has been designed and fabricated using LTCC technology. The filter with a dimension of 590 x 590 mil² was designed on Taconic's substrate with dielectric constant and dissipation factor of 10 and 0.001, respectively, and has been designed to operate at 2.4 GHz and 5.2 GHz respectively. Miyake et al. have also in [2.99] presented a dual-band filter fabricated in LTCC technology. This filter was designed using a combination of two staked BPFs operating at two different frequency bands 900 MHz and 1900 MHz. The total dimension of the filter was 3.2 x 4.5 x 2.0 mm³. Despite the excellent electrical performance of all these BPFs, their large dimensions make them inappropriate for the high miniaturization of wireless radio systems.

Wing-Yan Leung et al. [2.100] have proposed different lumped-element circuit topologies, which can be used to design BPFs with two transmissions zeros located at arbitrary frequencies. Based on these topologies, 2.4 GHz BPFs have been designed with lumped-element parallel plate capacitors and spiral-shaped inductors. "DuPont 951 tape" substrate with a dielectric constant and dissipation factor of 7.8 and 0.001, respectively, was used. The filter dimension was roughly 215 x 100 mil², and exhibited an insertion loss and a 3-dB-bandwidth of about -4.2 dB and 110 MHz, respectively. Recently, image reject (IR) BPFs for dual-band WLAN front-end module have been proposed [2.101]. The proposed BPFs were designed using two resonators with inter-digital capacitors to reduce the size. The dimension of the fabricated 802.11b/g BPF was 3.3 x 2.5 x 0.63 mm³; this filter exhibited an insertion loss and attenuation of -2.2 dB and -20 dB in 2.4-2.5 GHz band. Similarly, another fabricated 802.11a BPF had a size of 2.8 x 1.8 x 0.63 mm³ size, and presented an insertion loss and attenuation of -2.5 dB and -20.5 dB in the 5.725-5.825 GHz band.

Clearly, because of its low-cost and high performance, LTCC technology is a future-oriented technology, but for highly density packaging, another technology like MCM-D can also be used. This is reviewed in the next subsection.

2.7.3 MCM-D Embedded Filters

Technology Description

The thin-film multilayer multi-chip-module with deposited interconnect (MCM-D) technology results from a sequential deposition of metal layers and dielectric layers on a substrate carrier. Both the metal and dielectric layers are especially deposited in the form of thin-films and pattern by a photolithographic pattern transfer process. The substrate base layer or carrier must be very smooth and flat. Polished metal plates, ceramics, glass and semiconductor wafers have been used. The dielectric layers are usually polyimide or benzocyclobutene (BCB). The temperatures of deposition process are in the range of 200 °C for BCB up to 400 °C for polyimide.

In today's MCM-D technology, silicon is usually used as substrate base layer, because it is readily available, very smooth and flat, and relatively low-cost material and, more important, it matches the coefficient of thermal expansion of the dielectric layers, or low-stress polyimide, and of course, the silicon die. The fabrication processes are similar to those used in the manufacture of ICs; all of the features are photo-lithographically defined. The conductor layers are usually sputter-deposited copper, aluminum, or gold. The first layer deposited on silicon carrier can be either a conductor or a dielectric, depending on the circuit design. Typical MCM-D substrate build-up is shown in Fig. 2.14.

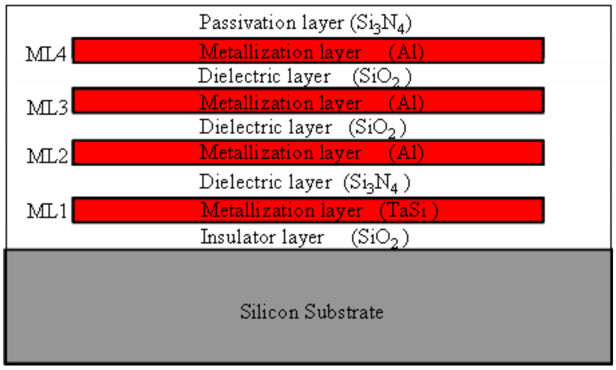

Figure 2. 14 Multilayer MCM-D substrate

One of the most important advantages of the MCM-D technology is the capability of high reproducibility of small metal pattern features and precise dielectric thickness control. In addition, it allows the realization of passive components in multilayer technology, reducing therefore the chip and substrate size as well as cost. This technology yields the highest circuit density while being the most process intensive and expensive of the three MCM technologies [2.85]. Although MCM-D tends to be expensive per unit substrate area, it can be cost-competitive, especially in large volumes.

Table 2.7 Typical properties of MCM-D substrates

Material Parameters	Inorganic dielectric on Silicon	Organic dielectric on Silicon
DK	3.6-4.0	2.4-4.0
DF at 1 MHz	0.03-0.3	0.002-0.006
Metallization	Al	Cr/Cu/Au
CTE (10−6/K)	2-3	2-3
TK (W/mK)	145	145

The most important substrate parameters are dielectric constant, dissipation factor, coefficient of thermal expansion (CTE), and thermal conductivity. The dielectric above the silicon substrate can be organic or inorganic. For organic dielectric over the silicon, the dielectric constant and the loss tangent are 2.4–4.0 and 0.002–0.006, respectively. For inorganic dielectric over the silicon, these parameter values are 3.6–4.0 and 0.03–0.3, respectively. These substrate parameters are summarized in Table 2.7.

Table 2.8 Typical design measures for MCM-D substrates

Minimal design values of MCM-D substrates				
Number of layers	Via size	Line width/space	Line thickness	Dielectric thickness
5	20 µm	20 µm	5 µm	1-10 µm

Typical feature (line widths and spaces, via-diameters, etc) sizes can be less than 25 µm, depending on the metal thickness and exact process flow. The typical design measures for MCM-D substrates are given in Table 2.8.

Filter Design and Integration using MCM-D Technology

A great deal of effort is investigated worldwide in the design of RF/microwave filters in MCM-D technology, and most of papers made so far are published in [2.102]-[2.106]. Recently, Zoschke et al. [2.103] have reported a realization of several passive filters, such as lowpass, bandpass, as well as bandstop passive filters, having a cut-off and center frequency of 2.4 GHz. The thin film build up was based on copper and benzocyclobute with a dielectric constant of 2.65. Instead of silicon, polished ceramics (Al_2O_3) have been used as substrate base carrier to prevent the substrate loss. These filters were realized using a combination of lumped element inductors and capacitors. A bandpass filter, which could be used for wireless applications such as Bluetooth, has been successfully realized with an insertion loss and a bandwidth of -1.6 dB and 600 MHz, respectively. Although excellent high performances have been met, this design used many single L and C components. This was the main drawback of this design.

Contrary to the Al_2O_3 used in [2.103], silicon was used as substrate base carrier in [2.104] for the realization of bandpass filters. A dual-behavior-resonator (DBR) filter with center frequency of 50 GHz, an insertion loss of -10.684 dB, and a 3-dB-passband of 3 GHz, was realized on 10 µm-thick BCB. MoM was used for the analysis, and the filter dimensions were 5826 x 2094 µm². The drawback of this design is that it required more size, since it was realized using lateral design topology. Another BPF centred at 2.4 GHz was designed in a Si-BCB technology and reported by [2.105]. The filter was also realized in 10 µm-thick BCB using 4 µm thick conductive gold metal layers. Its insertion loss and a 3-dB-bandwidth was 1.1 dB of 12.5 GHz, respectively, and its dimension was 2.25 x 1.2 mm².

Hartung has also reported [2.106] a successful realization of several filters (LP, HP, BP) in a frequency band from 0.2 to 2.5 GHz. These filters have been designed using lumped element inductors and capacitors. In this publication, the influence of the properties of the silicon substrate base carrier on the filter performances was investigated. As result, the best performance was obtained on highly resistive silicon substrate.

In [2.102], a 5.25 GHz BPF was realized in MCM-D technology using lumped element inductors and capacitor. The design consisted of two parallel LC resonators, which are coupled to each other and to their input and output terminals with lumped element capacitors. The dimension of the whole filter was 3164.6 x 1974.3 µm², and it bandwidth and insertion loss was 450 MHz and -2.5 dB, respectively.

2.8. Summary

RF filters can be designed using inductive/capacitive or resonant structures. Although the most popular realization forms are discrete and surface-mounted, enormous efforts have been made so far, in the design and integration of these filters using on-chip or off-chip integration approaches, with the objective of decreasing the component count and increasing the integration density as well as the performance.

The on-chip integration approaches are important, particularly for system-on-chip (SoC) packaging. Wireless filters using passive as well as active structures have been successfully realized. Passive on-chip filters introduce less noise, consume less power, and have wider bandwidth and linear operating range than their active equivalents. Unfortunately, they are limited to lower electrical performances, and are therefore not well suitable for RF signal pre-selection. Generally, on-chip integration techniques have the ability to achieve higher integration density with higher reliability, but at the cost of low electrical performances (low sensitivity and low selectivity) due to the low quality factor.

Fortunately, the off-chip integration approaches can be used to overcome these drawbacks. These techniques, which use the MCM based SiP technology, have the ability to increase the packaging reliability and electrical performance, as well as to decrease the development-cost, in comparison to the on-chip integration approaches.

Nevertheless, each of these integration techniques has its place in the modern wireless filter design and integration technology, and can be used for the implementation of RF filters. Based on this state-of-the art, a novel methodology for design and integration of highly miniaturized RF filters for wireless applications is developed and presented in subsequent chapters.

Chapter 3

Design Methodology for Integration and Miniaturization of RF Filters

In this chapter, a design methodology developed for the integration and miniaturization of RF filters is presented. The development involves three main steps consisting of design synthesis, physical design implementation, and fabrication as well as testing. Whereas the first and third main steps are common for the most electronic filters, the particularity of this methodology lies in the second main step, which is therefore thoroughly discussed in this chapter.

3.1. Design Synthesis

The design development begins with given filter specifications, followed by the approximation of these specifications using well-know mathematical transfer functions such as Butterworth-, Chebyshev-, Elliptic-, Gauss-function, etc. This approximation results in the initial filter network, the so-called LC-ladder network. The synthesized network is then evaluated and optimized by means of circuit analysis to meet the design goals. The condensed form of this step contains:

- Filter design specifications,
- Approximation using transfer functions (Chebyshev-function, for example), which results to LC-network,
- Analysis and optimization of the synthesized LC-network through circuit-simulations.

Each of these steps is presented in the following.

3.1.1 Filter Design Specifications

Filters (for signal selection) used in electronic circuitry reject the unwanted signals, while permitting a good transmission of the wanted ones. Depending on the applications, these filters may be designed as lowpass (LP), highpass (HP), bandpass (BP), or bandstop (BS).

The development of such filters begins with the specifications, which typically include the source/load impedance that are typically equal 50 ohms, the center frequency $\omega_0 = \sqrt{\omega_{p1} \cdot \omega_{p2}}$, the bandwidth $BW = \omega_{p2} - \omega_{p1}$, the maximum passband attenuation, $A_{\max}$ (also called passband ripple, ε), the passband edge frequency ω_p, the minimum stopband attenuation, $A_{\min}$, the stopband edge frequency ω_s, the selectivity factor ω_s / ω_p (also called edge steepness), etc. These parameters are illustrated in Figure 3.1.

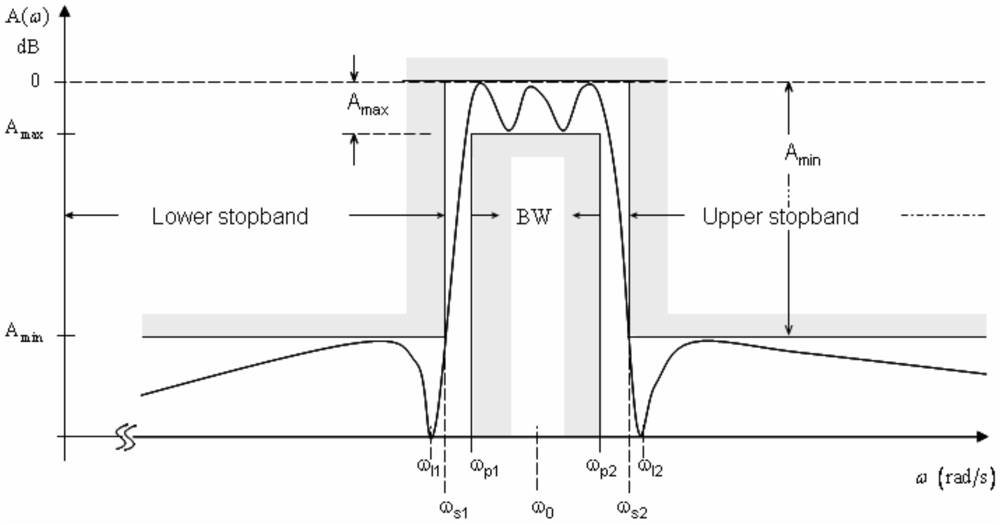

Figure 3.1 Filter response showing specifications for a bandpass filter

Depending on the applications, $A_{\max}$ typically ranges from 0.05 dB to 3 dB, and $A_{\min}$ can range from 20 dB to 100 dB. The transition band extends from the passband edge frequency (ω_p) up to the stopband edge frequency (ω_s). The selectivity factor (ω_s/ω_p) is usually used as a measure of the sharpness of the filter response.

The more tightly one specifies a filter, that is with lower $A_{\max}$ and higher $A_{\min}$, and/or ω_s/ω_p closer to unity, the closer the response of the resulting filter will be to the ideal. However, the resulting filter circuit must be of higher order and thus more complex and expensive. Once the filter specifications have been decided upon, the next step in the design is to find a transfer function, whose magnitude meets the given specifications within the frequencies of interest.

Each filter type can be further divided into subcategories according to its mathematical transfer functions, which can be Butterworth-, Chebyshev-, Bessel-, Elliptic-functions, etc. The transfer functions are primarily differentiated by the degree of their passband flatness, transition-band steepness, and out-of-band rejection. The process of obtaining a transfer function that meets the given specifications is known as filter approximation, which can be performed using closed-form expressions, as will be presented in next section.

3.1.2 Filter Design Synthesis

The synthesis is the determination of a network with no trial and error, when the excitation and response are given.

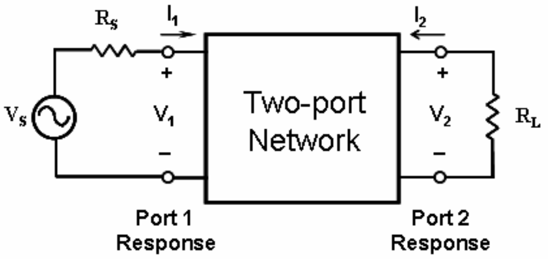

Figure 3.2 Schematic illustration of filter network synthesis

The transfer function of a network is the ration of its output voltage $V_2(j\omega)$ to input voltage $V_1(j\omega)$. This transfer function can be expressed in terms of transmission coefficient $\mathrm{T}(j\omega)$, with magnitude and phase as

$$\mathrm{T}(j\omega)=\left|\mathrm{T}(j\omega)\right|e^{j\phi(\omega)} \tag{3.1}$$

Thus, the transmission of the network can be expressed in terms of the attenuation function in decibels (dB) as

$$\mathrm{A}(\omega)=-20\log\left|\mathrm{T}(j\omega)\right|,\quad dB \tag{3.2}$$

3.1.2.1. Approximation of Filters

Filter responses can be approximated using different transfer function such as Chebyshev-, Butterworth-, Cauer-, Bessel-, Gauss-functions. The frequently used functions are described as follows.

A. Butterworth Function

The Butterworth (or maximally-flat) response is characterized by the fact that it has no ripple in the passband or stopband.

The magnitude of the transfer function of an *n*the-order Butterworth filter [3.2] with a passband edge frequency ω_p is given by

$$\left|\mathrm{T}(j\omega)\right|=\frac{1}{\sqrt{1+\left(\omega/\omega_p\right)^{2n}}} \tag{3.3}$$

where n is the filter order.

For a given passband attenuation ($A_{\max}$), stopband attenuations ($A_{\min}$), passband edge frequency (ω_p) as well as stopband edge frequencies (ω_s), the filter order can be determined by

$$n\geq\frac{\log\left(\dfrac{10^{\frac{A_{\min}}{10}}-1}{10^{\frac{A_{\max}}{10}}-1}\right)}{2\log\left(\omega_p/\omega_s\right)} \tag{3.4}$$

B. Chebyshev Function

The Chebyshev response is characterized by the presence of ripples in the passband and no ripples in the stopband. The Chebyshev response is more selective than the Butterworth response, but at the expense of higher passband attenuation ($A_{\max}$) and greater group delay. The magnitude of the transfer function of an *n*-the-order Chebyshev filter with a passband edge frequency ω_p, is given by

$$\left|\mathrm{T}(j\omega)\right|=\frac{1}{\sqrt{1+\varepsilon^2T_n^2\left(\omega/\omega_p\right)}} \tag{3.5}$$

where $\mathrm{T_n}(\omega)$ is the *n*the-order Chebyshev polynomial of the first kind defined by

$$T_n(\omega)=\begin{cases}\cos\left(n\cos^{-1}\omega\right), & |\omega|\le 1\\ \cosh\left(n\cosh^{-1}\omega\right), & |\omega|>1\end{cases} \tag{3.6}$$

and where ε the ripple constant, which is related to a given maximal passband attenuation $A_{\max}$ in dB by

$$\varepsilon=\sqrt{10^{A_{\max}/10}-1} \tag{3.7}$$

For given specifications, the required filter order can be determined by

$$n\ge\frac{\cosh^{-1}\sqrt{\dfrac{10^{A_{\min}/10}-1}{10^{A_{\max}/10}-1}}}{\cosh^{-1}\left(\omega_s/\omega_p\right)} \tag{3.8}$$

where $A_{\min}$ is the stopband attenuation at stopband frequency (ω_s), and $A_{\max}$ is the passband attenuation at cut-off frequency $(\omega_c=\omega_p)$.

3.1.2.2. Lowpass Prototype Filters

Filters are commonly synthesized based on polynomial transfer functions. The synthesis results in the so-called lowpass prototype filters [3.1]-[3.3].

Lowpass prototype filters are lowpass filters, whose element values are normalized to make the source and load resistance or conductance equal to unity, denoted $g_0=1$, $g_{n+1}=1$, and the cut-off angular frequency to be unity, denoted by $\Omega=\frac{\omega}{\omega_c}=1$. There are two different forms of n-pole lowpass prototype filters based on which all-poles filter response can be realized. These two forms are shown in Figure 3.3.

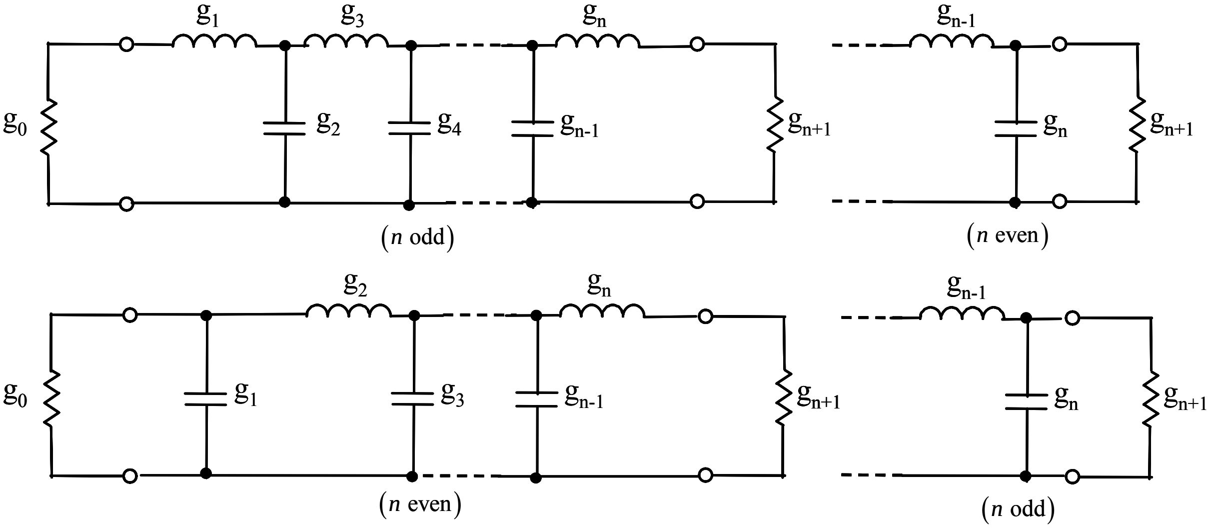

Figure 3.3 Lowpass prototype filter for all-pole filters with ladder network structures

In this figure, g_i (for i=1 to n) represents either the inductance (for series elements), or the capacitance (shunt elements); therefore, n is the number of reactive elements. If g_1 is the shunt capacitance or series inductance, then g_0 is the source resistance or conductance. Similarly, if g_n is the shunt capacitance or series inductance, g_{n+1} becomes the load resistance or the load conductance. The g-values are supposed to be the inductance in Henry, the capacitance in Farad, the resistance in ohm, and the conductance in mho.

From these lowpass prototype filters, practical filters such as lowpass (LB), highpass (HP), bandpass (BP), and bandstop (BS) can be derived using transformations equations for frequencies and g-elements. For filters based on common transfer functions (such as Chebyshev-, Butterworth-, Bessel-function), there are analytical expressions based on which the g-values can be calculated. The procedure of obtaining these g-values Chebyshev filters is described in the next section.

3.1.2.3. Extraction of Lowpass Prototype Elements by the Chebyshev Function

For a given filter specifications such as stopband attenuation $(A_{\min})$ at stopband frequency (ω_s), passband ripple $(A_{\max})$ at cut-off frequency $(\omega_c = \omega_p)$, the design procedure for the extraction of lowpass prototype elements is summarized as follows:

(1) Determination of the ripple constant $\varepsilon = \sqrt{10^{A_{\max}/10} - 1}$.

(2) Determination of the filter order $n \geq \dfrac{\cosh^{-1}\sqrt{\dfrac{10^{A_{\min}/10}-1}{10^{A_{\max}/10}-1}}}{\cosh^{-1}\left(\omega/\omega_p\right)}$, where $\Omega = \omega/\omega_p$ is the frequency transformation for LP, transforming the cut-off frequency from 1 to ω_c.

(3) Determination of the g_i values from the following equations [3.3]:

$$
\begin{aligned}
&g_0 = 1.0\\
&g_1 = \frac{2}{\gamma}\sin\left(\frac{\pi}{2n}\right)\\
&g_{i-1}\cdot g_i = \frac{4\sin\left[\frac{(2i-1)\pi}{2n}\right]\cdot\sin\left[\frac{(2i-3)\pi}{2n}\right]}{\gamma^2+\sin^2\left[\frac{(i-1)\pi}{n}\right]} \quad \text{for i=2, 3, \ldots } n\\
&g_{n+1} = \begin{cases} 1.0 & \textit{for n odd}\\ \coth^2\left(\frac{\beta}{4}\right) & \textit{for n even}\end{cases}\\
&\textit{where}\\
&\beta = \ln\left[\coth\left(\frac{L_{Ar}}{17.37}\right)\right]\\
&\gamma = \sinh\left(\frac{\beta}{2n}\right)
\end{aligned}
\tag{3.9}
$$

Remarks: For design simplicity, g_i of filters based on different transfer-functions have been extracted and tabulated; some of these values can be read off in [3.1]-[3.3]. Once the g-values are obtained, the next step is the derivation of the practical filters by scaling the g-values by the impedance and frequency factors. This step is described in the following.

3.1.2.4. Derivation of Practical Filters Network Elements

The impedance scaling required for the transformation of lowpass prototypes to practical filters is given by

$$\gamma_0 = \begin{cases} Z_0/g_0 & \textit{for } g_0 \text{ being the resistance} \\ g_0/Y_0 & \textit{for } g_0 \text{ being the resistance} \end{cases} \tag{3.10}$$

where $Y_0 = 1/Z_0$ is the source admittance

The important steps in the transformation procedure for different filter types (LP, HP, BP, and BS) are summarized as follows.

A. Lowpass Filter Transformation

(i) Transformation of the normalized frequency Ω into the angular frequency axis ω using

$$\Omega = \left(\frac{\Omega_c}{\omega_c}\right)\omega \tag{3.11}$$

(ii) Application of the frequency scaling factor (3.11) with the impedance scaling factor (3.10) to yield the following practical filter element values for series inductance and shunt capacitances given respectively by:

$$\begin{cases} L_i = g_i\left(\frac{\Omega_c}{\omega_c}\right)\gamma_0 & \textit{for } g_i \textit{ representing the } \text{inductance} \\ C_i = g_i\left(\frac{\Omega_c}{\omega_c}\right)\frac{1}{\gamma_0} & \textit{for } g_i \textit{ representing the } \text{capacitance} \end{cases} \tag{3.12}$$

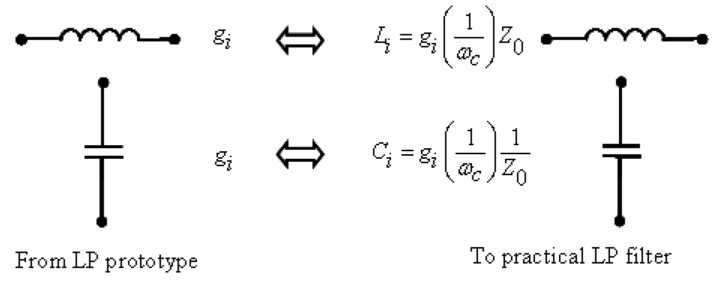

Figure 3.4 Transformation from lowpass prototype filter to practical lowpass filter

B. Highpass Filter Transformation

(i) Transformation of the normalized frequency Ω into the angular frequency axis ω using

$$\Omega = -\left(\frac{\Omega_c}{\omega}\right)\omega_c \tag{3.13}$$

(ii) Application of the frequency scaling factor (3.13) with the impedance scaling factor (3.10) to yield the following practical filter element values for series inductances and shunt capacitances given respectively by

$$\begin{cases} L_i = \dfrac{1}{g_i}\left(\dfrac{1}{\omega_c \Omega_c}\right)\gamma_0 & \textit{for } g_i \textit{ representing the } \text{capacitance} \\ C_i = \dfrac{1}{g_i}\left(\dfrac{1}{\omega_c \Omega_c}\right)\dfrac{1}{\gamma_0} & \textit{for } g_i \textit{ representing the } \text{inductance} \end{cases} \tag{3.14}$$

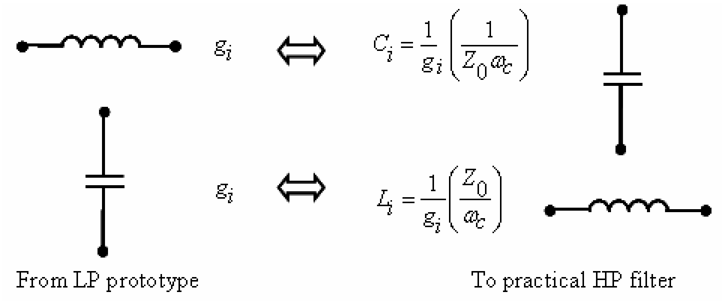

Figure 3.5 Transformation from lowpass prototype filter to practical highpass filter

C. Bandpass Filter Transformation

(i) When a lowpass prototype response with a cut-off frequency of Ω_c is to be transformed into a bandpass response having a passband of $(\omega_H - \omega_L)$, where ω_L and ω_H represent the passband edge angular frequencies, the required frequency transformation is given by

$$\Omega = \frac{\Omega_c}{FBW}\left(\frac{\omega}{\omega_0} - \frac{\omega_0}{\omega}\right) \tag{3.15}$$

where $\omega_0 = \sqrt{\omega_H \omega_L}$ and $FBW = (\omega_H - \omega_L)/\omega_0$ are the center angular frequency and the fractional bandwidth, respectively.

(ii) Applying the transformation above (3.15) with the impedance scaling (3.10) yields the following practical filter element values, where the series g_i are transformed to series LC resonant networks in the bandpass filter and the shunt g_i are transformed to parallel LC resonant networks in the bandpass filter.

$$\begin{cases} L_{s,i} = \left(\dfrac{\Omega_c}{FBW\omega_0}\right)\gamma_0 g_i \\ C_{s,i} = \left(\dfrac{FBW}{\omega_0 \Omega_c}\right)\dfrac{1}{\gamma_0 g_i} \end{cases} , \textit{ for } g_i \textit{ representing the } \text{inductance} \tag{3.16}$$

$$\begin{cases} L_{p,i} = \left(\dfrac{FBW}{\omega_0 \Omega_c}\right)\dfrac{\gamma_0}{g_i} \\ C_{p,i} = \left(\dfrac{\Omega_c}{FBW\,\omega_0}\right)\dfrac{g_i}{\gamma_0} \end{cases} \quad \text{, for } g_i \text{ representing the capacitance} \tag{3.17}$$

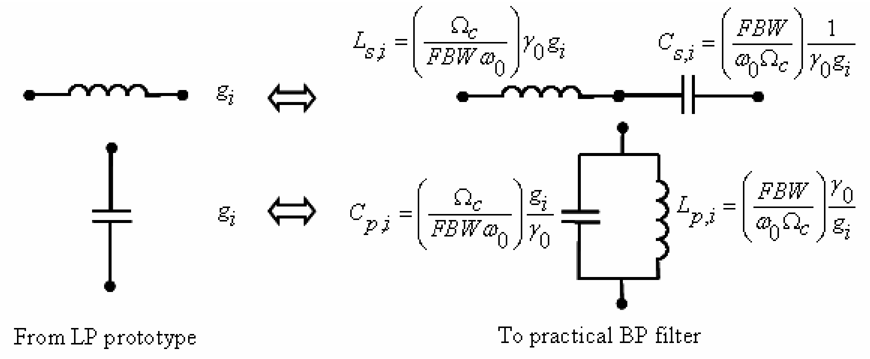

Figure 3.6 Transformation from lowpass prototype filters to practical bandpass filter

D. Bandstop Filter Transformation

(i) When a lowpass prototype response with a cut-off frequency of Ω_c is to be transformed into a bandstop response having a bandwidth of $(\omega_H - \omega_L)$, where ω_L and ω_H represent the stopband edge angular frequencies, the required frequency transformation is given by

$$\Omega = -\frac{\Omega_c FBW}{\left(\dfrac{\omega}{\omega_0} - \dfrac{\omega_0}{\omega}\right)} \tag{3.18}$$

where ω_0 and FBW are the center frequency and the fractional bandwidth, respectively.

(ii) Applying this transformation (3.18) with the impedance scaling factor (3.10) yields the following practical filter element values, where the series g_i are transformed to parallel LC resonant networks in the bandstop filter and the shunt g_i are transformed to series LC resonant networks in the bandstop filter.

$$\begin{cases} L_{p,i} = \left(\dfrac{\Omega_c FBW}{\omega_0}\right)\gamma_0 g_i \\ C_{p,i} = \left(\dfrac{1}{FBW\,\omega_0 \Omega_c}\right)\dfrac{1}{\gamma_0 g_i} \end{cases} \quad \text{, for } g_i \text{ representing the inductance} \tag{3.19}$$

$$\begin{cases} L_{s,i} = \left(\dfrac{1}{FBW\,\omega_0 \Omega_c}\right)\dfrac{\gamma_0}{g_i} \\ C_{s,i} = \left(\dfrac{\Omega_c FBW}{\omega_0}\right)\dfrac{g_i}{\gamma_0} \end{cases} \quad \text{, for } g_i \text{ representing the capacitance} \tag{3.20}$$

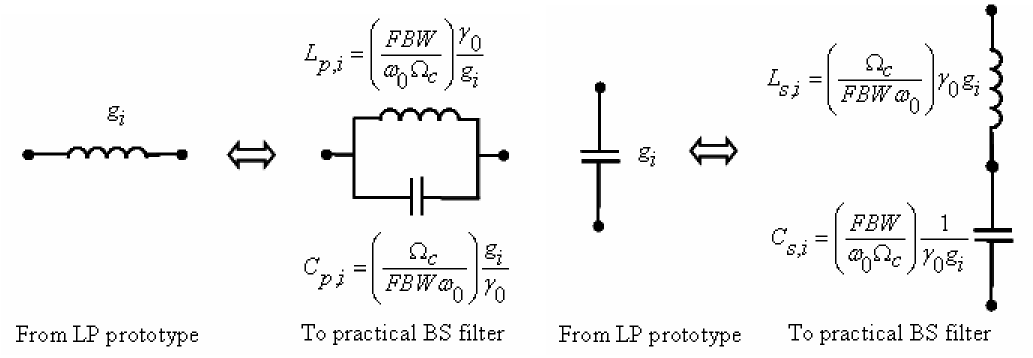

Figure 3.7 Transformation from lowpass prototype to practical bandstop filter

The parameters $L_{p,i}$, $C_{p,i}$ and $L_{s,i}$, $C_{s,i}$ are the practical elements of filters, where the superscripts *i* represents the number of poles.

3.1.3 Analysis and Optimization of Synthesized Bandpass Filters

3.1.3.1. LC Networks

After applying the required transformations, the synthesized LC-networks of bandpass filters can be obtained. Figure 3.8 shows the example of LC-networks of an n-pole bandpass filter, where G_A and G_B are source and load admittance, L_i and C_i are inductances and capacitances.

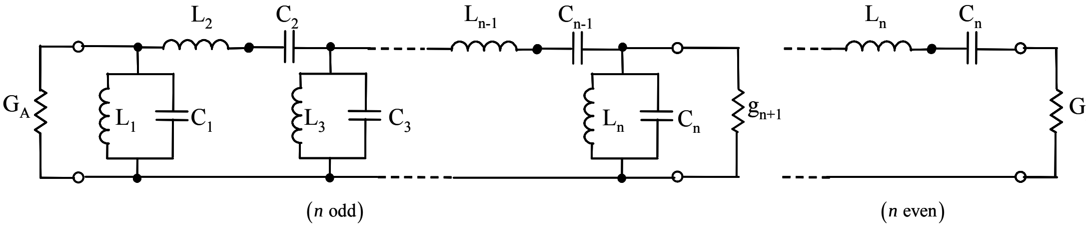

Figure 3. 8 LC-networks of an n-pole bandpass filter

Although these LC-networks are common for all electronic filters, however, their physical realizations can vary depending on the applications and realization technologies.

Since the practical realization of alternating series/shunt LC-networks (of Figure 3.8) is very difficult, particularly in some RF/microwave technologies, the networks can be simplified into one type of LC-networks (either series or parallel LC-networks), by means of inverters circuits.

3.1.3.2. Simplification of Bandpass Filter Circuit Networks

A. Immittance Inverters and Circuit Realizations

Immittance inverter is a collective name for impedance inverter (or *K*-inerter) and admittance inverter (or *J*-inverter). These elements are 2-port networks, whose input admittance (Y_{in}) and impedance (Z_{in}) are dual to their load admittance (Y_L) and impedance (Z_L), respectively, and can be symbolized as shown in Figure 3.9.

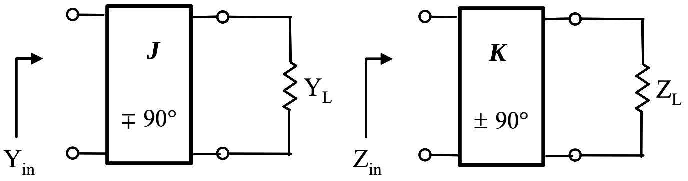

Figure 3. 9 Admittance and impedance inverters

The duality factor *J* and *K*, also called admittance and impedance inverters, are given by $Y_{in} = J^2/Y_L$ and $Z_{in} = K^2/Z_L$, respectively. Based on these properties, a parallel LC-resonant network with an inverter on each side looks like a series LC-resonant network. Similarly, a series LC-resonant network with an inverter on each side looks like a parallel LC-resonant network.

There are various circuit realization possibilities for *K*- and *J*-inverters. Typical realizations of *K*- and *J*-inverters with passive elements are shown in Figure 3.10.

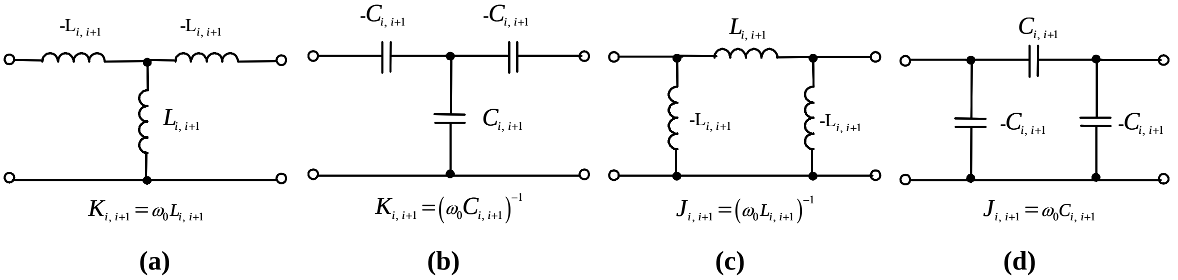

Figure 3.10 Typical realizations of K- or J-inverters with passive elements

Series LC-resonant networks can be coupled using K -inverters (Fig. 3.10.a and b) and parallel LC-resonant networks can be coupled using J -inverters (Fig. 3.10.c and d).

Since the negative elements of these inverters can not be compensated when placed at the generator side, using these inverters at the I/O-ports of filter networks becomes unpractical. Therefore, appropriated inverter circuits for I/O-ports must be used. Various circuits are available for this purpose.

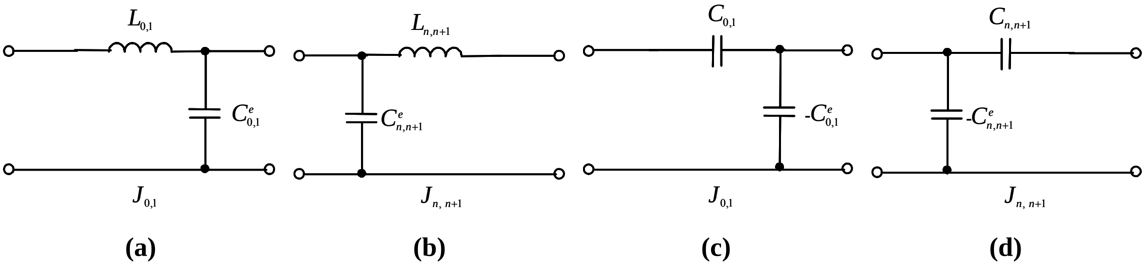

Figure 3.11 Typical LC-circuit network that may be used as K-inverter or J inverter

Figure 3.11 shows the example of I/O-port matching networks, which can be used in case of parallel coupled LC networks. By the use of these circuits, circuit networks of bandpass filters can be simplified for easy practical implementation.

B. Simplified LC Networks of Bandpass Filters

The concept of network simplification is presented here for the illustration. The circuit network of an n-pole bandpass filter is reduced into a cascade of the *J*-inverters and parallel LC-resonant networks as shown in Figure 3.12.

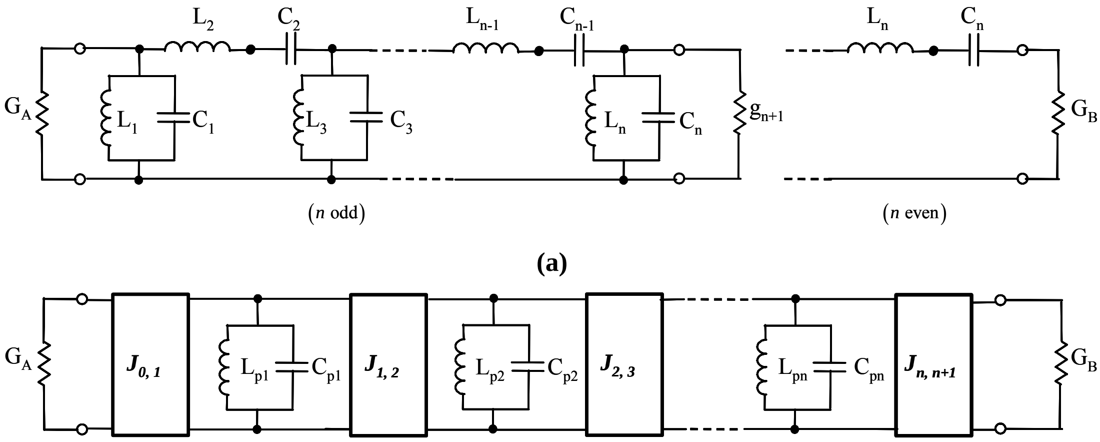

(a)

(b)

Figure 3. 12 Simplification of LC-networks of an n-poles bandpass filter into a cascade of J-inverters and parallel LC-resonant networks

Replacing the inner inverters by the circuit of Figure 3.10.d and the input/output inverters by the matching networks of Figure 3.11.a and b, then the n-poles bandpass filter results finally to the network shown in Figure 3.13.

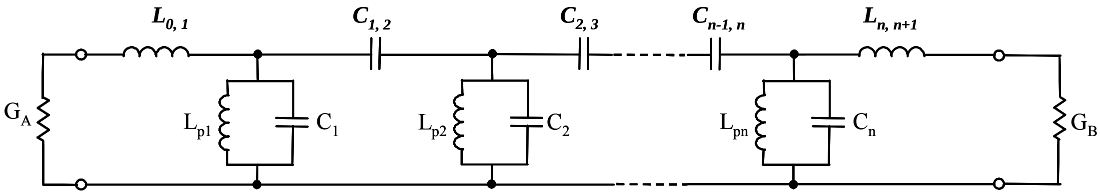

Figure 3. 13 Simplified LC-networks of an n-poles bandpass filter with inductive input/output

On the other hand, by replacing the inner inverters by the circuit of Figure 3.10.d and the input/output inverters by the matching networks of Figure 3.11.c and d, then the n-pole bandpass filter results finally to the circuit shown in Figure 3.14.

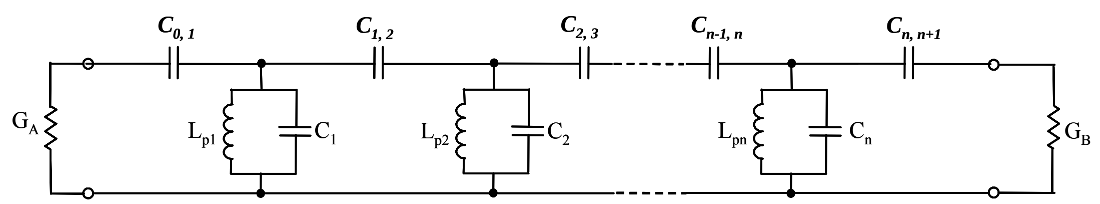

Figure 3. 14 Simplified LC-networks of an n-poles BPF with capacitive input/output

The circuit elements can be calculated using the design formulas [3.1] given by:

$$J_{0,1} = \sqrt{\frac{\delta\omega_0 C_{p1} G_A}{\Omega_c g_0 g_1}} \tag{3.21.a}$$

$$J_{i,i+1} = \frac{\delta\omega_0}{\Omega_c}\sqrt{\frac{C_{pi}C_{p,i+1}}{g_i g_{i+1}}} \qquad i = 1,\ 2,\ 3,\cdots,\ \text{n-1} \tag{3.21.b}$$

$$J_{n,n+1} = \sqrt{\frac{\delta\omega_0 C_{pn} G_B}{\Omega_c g_n g_{n+1}}} \tag{3.21.c}$$

$$C_{pi} = 1 \big/ L_{pi}\omega_0^2 \qquad i = 1,\ 2,\ 3,\cdots,\ n \tag{3.21.d}$$

where $\delta = FBW = (\omega_H - \omega_L)/\omega_0$ and $\omega_0 = \sqrt{\omega_H \omega_L}$, g_i are the prototype element values, C_{pi} , Z_0 , L_{pi} , G_A and G_B , can be chosen as desired.

After obtaining the network elements, their values can be optimized by means of circuit analysis, to meet the filter design specifications. The optimized networks can finally be approximated using RF/microwave design techniques and implemented into a RF/microwave Technology. This task is carefully discussed in next sections.

3.2. Physical Design Implementation

Although the LC circuit network is common to all electronic filters, however its physical realization can vary depending on the implementation techniques as well as realization technologies.

Various RF/microwave filter design techniques/technologies are available, e.g. SAW-filter, waveguide/dielectric-filter, coaxial-filter, microstrip-filter. The choice of one or other technology depends on the applications (e.g. operation frequencies), electrical performances (quality factor, steepness, etc), implementation-costs, as well as miniaturization-requirements.

Thus, *SAW-filter* technique exhibits very higher Q_u, up to $1 \cdot 10^5$, but this approach is limited to low gigahertz applications. *Waveguide/dielectric-filter* technique offers high Q_u, up to $5 \cdot 10^4$ and can be used for applications up to 100 GHz. However, this technique requires higher implementation-cost and the final device can be bulky. *Microstrip-filter* design technique exhibits Q_u ranging up to $1.5 \cdot 10^2$ and can be used for applications operating between 300 MHz and 30 GHz. Despite its lower Q_u, this technique has the advantage of lower implementation-cost and offers good design miniaturization possibilities. Therefore, this approach is preferred for the design realization of filters developed in this work.

Thus, the next main step in the development of bandpass filters is the approximation of the synthesized LC-ladder networks using microstrip techniques. This step is described in the following sections.

3.2.1 Approximation of Reactors and Resonators with Microstrip Lines

3.2.1.1. Frequency Behaviour of ideal Reactors and Resonators

The reactance and susceptance of inductors and capacitors are given, respectively, by

$$Z_L = jX_L = j\omega L \tag{3.22.a}$$

$$Y_C = jB_C = j\omega C \tag{3.22.b}$$

where L, C, and ω are the inductance , capacitance, and angular frequency, respectively.

The frequency behaviour of these functions (as seen in Figure 3.16.a) is a straight line with slope L, and C, respectively.

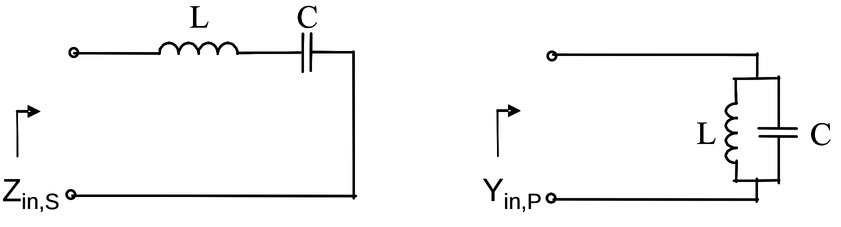

(a) **(b)**

Figure 3. 15 a) Series and b) parallel LC-resonant networks

The input impedance $Z_{in,s}$ and admittance $Y_{in,p}$ of series and parallel LC-resonant networks of Figure 3.15 are given, respectively, by

$$Z_{in,s} = jX_S = j\left(\omega L - \frac{1}{\omega C}\right) = j\sqrt{L/C}\left(\frac{\omega}{\omega_0} - \frac{\omega_0}{\omega}\right) = j\omega_0 L\left(\frac{\omega}{\omega_0} - \frac{\omega_0}{\omega}\right) \tag{3.23}$$

$$Y_{in,p} = jB_P = j\left(\omega C - \frac{1}{\omega L}\right) = j\sqrt{C/L}\left(\frac{\omega}{\omega_0} - \frac{\omega_0}{\omega}\right) = j\omega_0 C\left(\frac{\omega}{\omega_0} - \frac{\omega_0}{\omega}\right) \tag{3.24}$$

where $\omega_0 = 1/\sqrt{LC}$ is the circuit resonant frequency, X_s and B_p are circuit reactance and susceptance, respectively.

By setting $\mathbf{b}_s = \sqrt{L/C}$, $\mathbf{b}_p = \sqrt{C/L}$ as normalized admittance or susceptance, these input impedance and admittance can be rewritten as

$$Z_{in,s} = jX_s = j\left(\omega L - \frac{1}{\omega C}\right) = j\mathbf{b}_s\left(\frac{\omega}{\omega_0} - \frac{\omega_0}{\omega}\right) = j\mathbf{b}_s \nu \tag{3.25}$$

$$Y_{in,p} = jB_p = j\left(\omega C - \frac{1}{\omega L}\right) = j\mathbf{b}_p\left(\frac{\omega}{\omega_0} - \frac{\omega_0}{\omega}\right) = j\mathbf{b}_p \nu \tag{3.26}$$

where $\nu = (\omega/\omega_0 - \omega_0/\omega)$

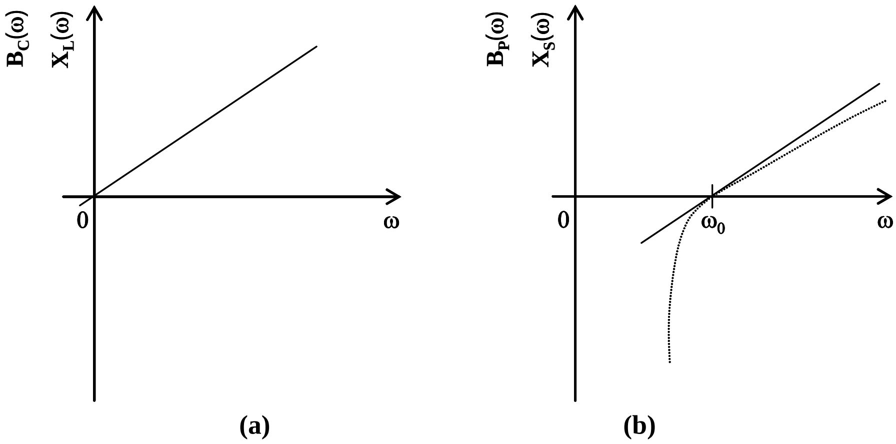

Figure 3. 16 Frequency behaviour of a) ideal reactors, and b) series/parallel LC-resonators

The frequency behaviour of these series/parallel LC-resonators can be described by the plots shown in Figure 3.16.b.

3.2.1.2. Frequency Behaviour of Transmission Line Circuits

The input impedance of a lossless transmission line of length l is given by:

$$Z_{in} = Z_0 \cdot \frac{Z_L \cdot \cos(\beta l) + jZ_0 \cdot \sin(\beta l)}{Z_0 \cdot \cos(\beta l) + jZ_L \cdot \sin(\beta l)} = Z_L \cdot \frac{1 + j\frac{Z_0}{Z_L} \cdot \tan(\beta l)}{1 + j\frac{Z_L}{Z_0} \cdot \tan(\beta l)} \tag{3.27}$$

where β is the phase constant, Z_0 and Z_L are the characteristic impedance and load impedance, respectively.

Short-Circuited Transmission Line

When the line is short-terminated, i.e. $Z_L = 0$, its input impedance becomes

$$Z_{in,short}(l) = jX_{short} = jZ_0 \cdot \tan(\beta l) \tag{3.28}$$

Accordingly, the input admittance is given by:

$$Y_{in,short}(l) = \frac{1}{Z_{in,short}(l)} = jB_{short} = -j\frac{1}{Z_0} \cdot \cot(\beta l) \tag{3.29}$$

Open-Circuited Transmission Line

Otherwise, when the line is open-terminated, i.e. $Z_L = \infty$, then its input impedance is given by:

$$Z_{in,open}(l) = jX_{open} = -jZ_0 \cdot \cot(\beta l) \tag{3.30}$$

Analogous, its input admittance is given by:

$$Y_{in,open}(l) = \frac{1}{Z_{in,open}(l)} = jB_{open} = j\frac{1}{Z_0} \cdot \tan(\beta l) \tag{3.31}$$

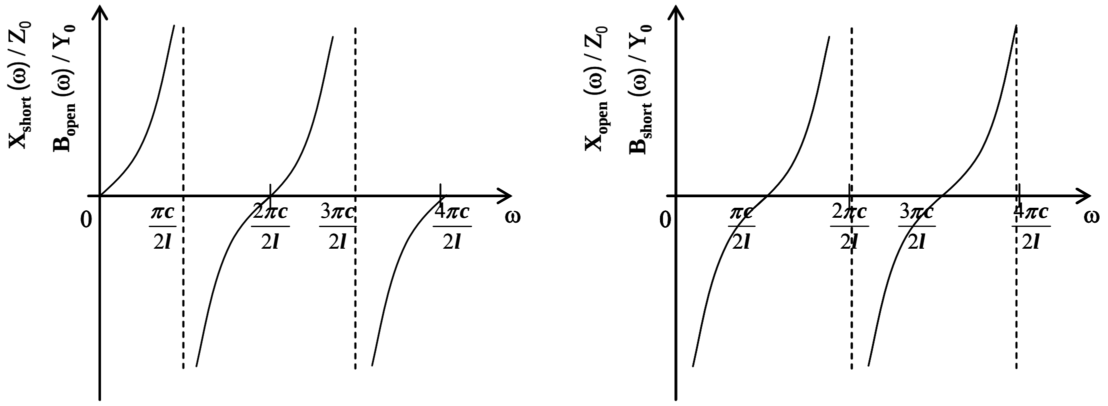

(a) **(b)**

Figure 3. 17 Frequency behaviour of a) short-terminated and b) open-terminated transmission lines

As can be seen the reactance of a short-terminated line (3.28) and the susceptance of an open-terminated line (3.31) are similarly in their form. These equations exhibit a zero-crossing when $\beta l = \pi/2$ or $l = \lambda/4$. Their frequency behaviour can be described by the plots of Figure 3.17.a.

Analogously, the susceptance of a short-terminated line (3.29) and the reactance of an open-terminated line (3.30) are similarly in the form. These equations exhibit a zero-crossing when $\beta l = \pi$ or $l = \lambda/2$. Their frequency behaviour can also be described by the plots of Figure 3.17.b.

3.2.1.3. Comparative Study

When comparing the frequency behaviour of these lossless short/open-terminated lines with the frequency behaviour of ideal reactors (X_L, and B_C) as well as series/parallel resonators (X_S, and B_P), it will be noted that:

(1) A lumped element inductance L can be approximated using a section of a short-terminated transmission line of length *l* that is much smaller than the quarter-wavelength at the frequency of interest.

(2) Similarly, a lumped-element capacitance C can also be approximated using a section of an open-terminated transmission line of length *l* that is much smaller than the quarter-wavelength at frequency of interest.

(3) A series/parallel LC-resonant network can be approximated, near the resonance ω_0, by:

  a. A section of a short-terminated transmission line at frequencies $\omega = \frac{\pi}{2}\frac{c}{l}, \frac{3\pi}{2}\frac{c}{l}, \cdots$, i.e. by a section of a short-terminated line of length $l = (2n+1)\lambda_{go}/4$, where λ_{go} is the guide wavelength at the operation frequency, and $n = 0,1,2,3,\ldots$., or by

  b. A section of an open-terminated line at frequencies $\omega = 0, \frac{2\pi}{2}\frac{c}{l}, \frac{4\pi}{2}\frac{c}{l}, \cdots$, i. e. by an open-terminated line of length $l = (n+1)\lambda_{go}/2$, where λ_{go} is the guide wavelength at the operational frequency, and $n = 0,1,2,3,\ldots$

From these statements, it follows that:

- The slope of a reactance (in other words, the inductance L) and the slope of the input impedance of a short-terminated line of length *l*, which is much smaller than a $\frac{1}{4}$ guide wavelength at the origin, can be matched (3.32).

$$\begin{cases} \left.\dfrac{\partial X_L(\omega)}{\partial \omega}\right|_{\omega=0} = L \\ \left.\dfrac{\partial Z_{in,short}(\omega)}{\partial \omega}\right|_{\omega=0} = Z_0\dfrac{l}{v_p} \end{cases} \tag{3.32}$$

Therefore, the slope parameter, L, of a reactance can be expressed by:

$$L = Z_0\frac{l}{v_p} \tag{3.33}$$

- The slope of a susceptance (in other words, the capacitance C) and the slope parameter of the input admittance of an open-terminated line of length *l*, which is much smaller than a quarter guide wavelength at $\omega = 0$, can be matched (3.34).

$$\begin{cases} \left.\dfrac{\partial B_C(\omega)}{\partial \omega}\right|_{\omega=0} = C \\ \left.\dfrac{\partial Y_{in,oen}(\omega)}{\partial \omega}\right|_{\omega=0} = Y_0\dfrac{l}{v_p} \end{cases} \tag{3.34}$$

Hence, the slope parameter, C, of a reactance can be expressed by:

$$C = Y_0\frac{l}{v_p} \tag{3.35}$$

- The slope parameter of the input admittance of a parallel LC-resonator and the slope parameter of the input admittance of a short-circuited line of length *l* near the resonance can also be approximated (3.36).

$$\begin{cases} \left.\dfrac{\partial B_P(\omega)}{\partial \omega}\right|_{\omega=\omega_0} = 2C \\ \left.\dfrac{\partial Y_{in,short}(\omega)}{\partial \omega}\right|_{\omega=\omega_0} = Y_0\dfrac{l}{v_p} = \dfrac{Y_0}{\omega_0}\pi\dfrac{(2n+1)}{2} \end{cases} \tag{3.36}$$

Therefore, the parallel capacitance C of a LC-resonator can be expressed by a section of short-terminated line of length *l*:

$$2C = Y_0\frac{l}{v_p} = \frac{Y_0}{\omega_0}\frac{(2n+1)\pi}{2} \tag{3.37}$$

And the corresponding parallel inductance of the resonator can then be determined through the resonant frequency by $L = \left(\omega_0^2 C\right)^{-1}$.

- Similarly, the slope parameter of the input impedance of a series LC-resonator and the slope parameter of the input reactance of an open-terminated line of length *l* near the resonance can be approximated (3.38)

$$\begin{cases} \left.\dfrac{\partial X_S(\omega)}{\partial \omega}\right|_{\omega=\omega_0} = 2L \\ \left.\dfrac{\partial X_{in,open}(\omega)}{\partial \omega}\right|_{\omega=\omega_0} = Z_0 \dfrac{l}{v_p} = \dfrac{Z_0}{\omega_0}\pi\dfrac{(2n+1)}{2} \end{cases} \tag{3.38}$$

It follows that the series inductance L of a LC-resonator can be expressed by a section of an open-terminated line of length *l*:

$$2L = Y_0 \frac{l}{v_p} = \frac{Z_0}{\omega_0}\frac{(2n+1)\pi}{2} \tag{3.39}$$

Similarly, the corresponding capacitance can be determined through the resonant frequency by $C = \left(\omega_0^2 L\right)^{-1}$.

Inclusion of Losses

In practice, transmission line circuits are lossy, therefore, attenuation must be considered in the design equations in order to reflect the reality. Thus, the propagation constant in lines becomes

$$\gamma = j(\beta - j\alpha) = \alpha + j\beta \tag{3.40}$$

where $\alpha = \alpha_c + \alpha_d + \alpha_r$ represents the total attenuation constant arising from the conductor losses, dielectric losses, and radiation losses.

These losses can be expressed by means of quality factor as:

$$\frac{1}{Q_u} = \left(\frac{1}{Q_c} + \frac{1}{Q_d} + \frac{1}{Q_r}\right) \tag{3.41}$$

Analogously, resistance (R_s) and conductance (G_p) must be inserted into the LC circuit network in order to account for losses; hence, the input impedance ($Z_{in,s}$) and input admittance ($Y_{in,p}$) of a series/parallel LC resonant network become:

$$Z_{in,s} = R_s + jX_s = R_s + j\left(\omega L - \frac{1}{\omega C}\right) = R_s + j\mathbf{b}\left(\frac{\omega}{\omega_0} - \frac{\omega_0}{\omega}\right) = R_s + j\mathbf{b}\nu \tag{3.42}$$

$$Y_{in,p} = G_p + jB_p = j\left(\omega C - \frac{1}{\omega L}\right) = G_p + j\mathbf{b}\left(\frac{\omega}{\omega_0} - \frac{\omega_0}{\omega}\right) = G_p + j\mathbf{b}\nu \tag{3.43}$$

And the unloaded quality factor Q_u of this series/parallel circuit network can be expressed by $Q_u = \mathbf{b}/R_s$ for the series circuit network, and $Q_u = \mathbf{b}/G_p$ for the parallel circuit network.

Conclusion

From these analyses, one can note that a section of a transmission line can be used to approximate an inductance (L), capacitance (C), and parallel/series resonant network (LC).

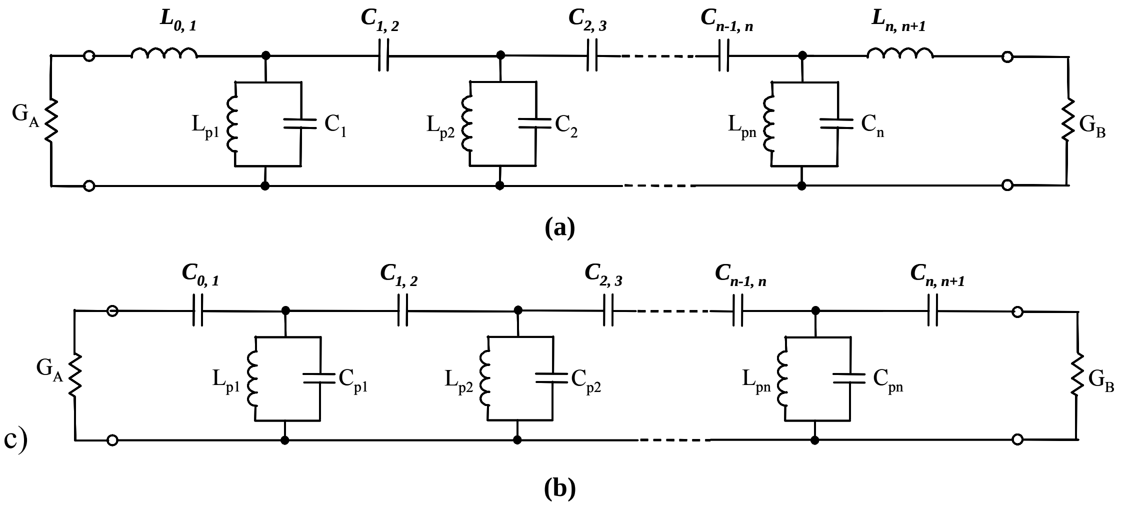

Figure 3. 18 LC-networks of an n-pole bandpass filter with a) inductive and b) capacitive I/O-ports

Thus, the LC-networks of an n-pole bandpass filter (Figure 3.18) can be realized and implemented using sections of microstrip lines configured variously, e.g.:

(1) Connection of reactors that are inductors and capacitors: The inductor structures of length *l*, with $l \ll \lambda_g/10$, provide the inductances. The capacitor structures of length *l*, with $l \ll \lambda_g/10$, provide the capacitances, wherein λ_g is the guide wavelength at the frequency of interest.

This conventional approach of realizing filters has the advantage of small foot print and mass of the final device, and it is therefore well appropriated for high miniaturization of integrated components. But, more design structures are required for the filter realization.

(2) Connection of resonators and reactors: The resonators may be inductors or capacitors, whose structure length is $\le \lambda_g/4$. The inductors provide the inductances as well as parasitic capacitances. The capacitors provide the capacitances as well as parasitic inductances.

The reactors, used for the connection of the adjacent resonators, may be capacitors. Those used at the network I/O-ports may be inductors or capacitors. The capacitor structures of length *l*, with $l \ll \lambda_g/10$, provide the capacitances. The inductor structures of length *l*, with $l \ll \lambda_g/10$, provide the inductances.

(3) Coupling of resonators with reactors at the network I/O-ports: The resonators, as defined previously (case 2), are coupled to each other. The reactors, used at the network I/O-ports, may be inductors or capacitors, whose structures length *l* is $\le \lambda_g/10$, and provide inductances or capacitances.

Filters developed in this work, are based on the last-mentioned design realization approach (case 3). Through this design approach, parasitic reactance (i.e. parasitic capacitances) can positively be used in the filter design. Furthermore, this approach requires fewer design structures decreasing thereby the development-cost/cycle. In addition, this approach enables the realization of narrowband filters due to the very good controllable inter-resonator coupling. Its only drawback is that the size of the final device can be larger.

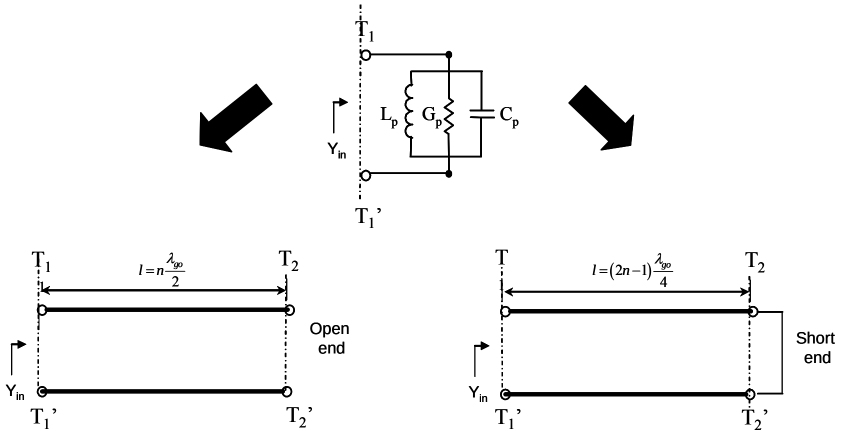

Figure 3. 19 Approximation of LC-resonators using sections of transmission lines

Figure 3.19 illustrates the approach of approximation of L , C and G by sections of open-terminated lines of length $l=(n+1)\lambda_{go}/2$ and short-terminated lines of length $l=(2n+1)\lambda_{go}/4$, where λ_{go} is the guide wavelength at the frequency of interest and $n=0,1,2,3,\ldots$. This design concept is thoroughly discussed throughout the chapter.

3.2.2 Definition of RF/Microwave Integration Medium

After approximating the filter network elements, the next step in the design and integration of bandpass filters is the definition of an adequate integration medium (substrate materials and technology). This step is of importance in the development of circuits for RF/microwave applications and it has a great impact on the component performances.

With the growth of wireless communication markets various new substrate materials have been developed to address the ever increasing need for high-frequency and high-speed circuit applications. Therefore, different RF/microwave substrate materials are available for system-in-package (SiP) technologies. In various RF/wireless circuits, there is a need for a stable dielectric constant over the temperature, a lower dissipation factor, as well as an ability to carry high power levels through materials. In most of the cases, designers must make a trade-off between cost and performances. For the implementation of filters developed in this work, the combination of Rogers' ("RO4350B Core" and "RO4450B Prepreg") and ISOLA's ("IS620 Core") materials was selected.

RO4350B and RO4450B are glass reinforced hydrocarbon/ceramic laminate materials, which offer high frequency performance and can be fabricated using low-cost standard epoxy/glass /FR4 processes at competitive prices [3.4]. Their stable electrical properties allow for repeatable design of filters, matching networks and controlled impedance transmission line. Their low dielectric loss allows them to be used in many applications, where higher operating frequencies limit the use of conventional circuit board FR4-based material. Additionally, these Rogers' materials present good coefficient of thermal expansion (CTE), which is similar to that of copper allowing therefore an excellent dimensional stability. Their low Z-axis CTE provides reliable plated through-hole quality, even in severe thermal shock applications. High glass transition temperature (about 280ºC) along with high thermal conductivity (0.62 W/m/ºK) makes them to be used in a wide variety of operating environments and process conditions. So their expansion characteristics remain stable over the entire range of circuit processing temperatures.

IS620 is a modified epoxy based material with moderate high frequency properties and good CTE. This material can also be fabricated using low-cost standard epoxy/glass/FR4 processes at competitive prices. The most important advantage of this material is the economical price, when compared to other high frequency-materials.

Table 3. 1 Properties of Rogers' and ISOLA's high frequency substrate materials

Material	RO4450B Core	RO4350B Prepreg	IS620 Core
Dielectric constant, ε_r	3.54±0.05	3.48±0.05	3.6
Dissipation factor, tanδ	0.004	0.0037	0.008
Coefficient of thermal expansion, CTE, in ppm/°C for direction X, Y, Z	19, 17, 60	14, 16, 50	17, 17, 60
Glass transition temperature, T_g, in °C	280	280	105-145
Thermal conductivity in W/m/°K, measured under 100°C	0.60	0.62	0.27
Minimal thickness	0.004" (0.101mm)	0.004"(0.101mm)	0.002"(0.050mm)

All theses materials are available in different standard thicknesses and can be processed using copper cladding with ½ oz (18 µm), 1 oz (36 µm), and 2 oz (72 µm). More information about these materials and technology process can be taken out from the vendor's homepage [3.4], [3.5]. The most important parameters of these materials, which are used in the multilayer PCB construction of the developed filters in this work, are given in Table 3.1.

3.2.3 Dimensioning of Filter Design Structures

Inductors and capacitors are key building blocks of electronic filters. For efficient filter design, these components must be accurately designed and dimensioned. The next step in the filer design development is the dimensioning of these filter design structures.

3.2.3.1. Inductor Design Structures

A. Design Shape

Microstrip inductors can be designed using different shapes, e.g. straight line, meander line, spiral line (with rectangular, hexagonal, octagonal, or circular shape). The choice of these design shapes depends on the electrical performances as well as on the simplicity in the layout implementation.

In this work, spiral inductors with rectangular shape were chosen for the approximation of LC-resonant networks of the bandpass filters. This shape is easy to implement and is very practical for the realization of edge coupling. Sections of straight lines have been also chosen for the realization of the inductive I/O-ports of filters.

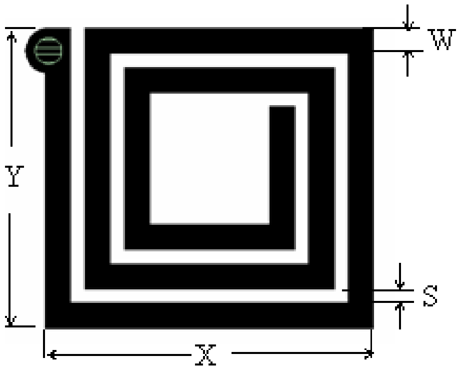

Figure 3. 20 Layout of a spiral resonant inductor with rectangular shape

Figure 3.20 shows the layout of a short terminated spiral resonant inductor with rectangular shape. The most important geometry parameters of this element are the total line length, line width, line space, line thickness, and inner/outer dimensions.

B. Length of Inductor

The total electrical length of a resonant inductor can be determined using:

$$l = \theta \frac{v_p}{\omega_0} = \frac{\theta}{2\pi} \frac{c_0}{f_0\sqrt{\varepsilon_{req}}} \tag{3.44}$$

where f_0 is the center frequency of the bandpass filter, ε_{req} is the equivalent effective dielectric constant, v_p is the phase velocity in medium, and θ is the electrical length at center frequency, $c_0 = 3\times10^8\ m/s$.

The shortest electrical length is equal to $\pi/2$ for short-terminated inductors, and π for open-terminated inductors.

The equivalent dielectric constant of the multi-layer medium can be determined by:

$$\varepsilon_{req} = \left[\frac{1}{H_T} \sum_{i=1}^{n} \frac{H_i}{\varepsilon_{ri}} \right]^{-1} \tag{3.45}$$

with $H_T = \sum_{i=1}^{n} H_i = H_1 + H_2 + \cdots + H_n$, where H_i and ε_{ri} are dielectric thickness and dielectric constant of each layer, respectively.

C. Inductance

There are various expressions of inductance, depending on the line shapes and geometry parameters. For instance, the inductance of spiral inductor can be estimated from *Greenhouse's formula* [3.46] using (3.46),

$$L = \sum_{i=1}^{N} L_{self,\,i} + \sum_{i=1}^{N-1} \sum_{j=i+1}^{N} 2M_{ij} \tag{3.46}$$

where L_{self} and M are the self and mutual inductance of the strip line [3.9] given in (3.47) and (3.48), respectively by

$$L_{self} = 2\times10^{-7}l\left[\ln\left(\frac{2l}{w+t}\right) - 0.50049 + \frac{w+t}{3l}\right] \tag{3.47}$$

$$M = 2\times10^{-7}l\left[\ln\left(\frac{1}{GMD} + \sqrt{1+\left(\frac{1}{GMD}\right)^2}\right) - \sqrt{1+\left(\frac{1}{GMD}\right)^2} + \frac{GMD}{l}\right] \tag{3.48}$$

where t and w are the thickness, and the width of the metal line, respectively, and where, GMD given in (3.49) is the geometric mean distance between the metal strips,

$$GMD = \exp\left[\ln(D) - \left(\frac{1}{12\left(\frac{D}{w}\right)^2} + \frac{1}{60\left(\frac{D}{w}\right)^4} + \frac{1}{168\left(\frac{D}{w}\right)^6} + \frac{1}{360\left(\frac{D}{w}\right)^6}\right)\right] \tag{3.49}$$

with D being the center-to-center distance of the two conductors.

D. Capacitance

Microstrip inductor structures have associated parasitic capacitances, arising from the inter-winding and ground plane. The amount of these capacitances can be determined through the resonant frequency equation given by $C = \left(\omega_0^2 L\right)^{-1}$.

3.2.3.2. Capacitor Design Structures

A. Design Shape

There are various design shapes for integrated capacitors, the most popular ones are the interdigital design shape, and the metal-insulator-metal (MIM) design shape (Figure 3.21).

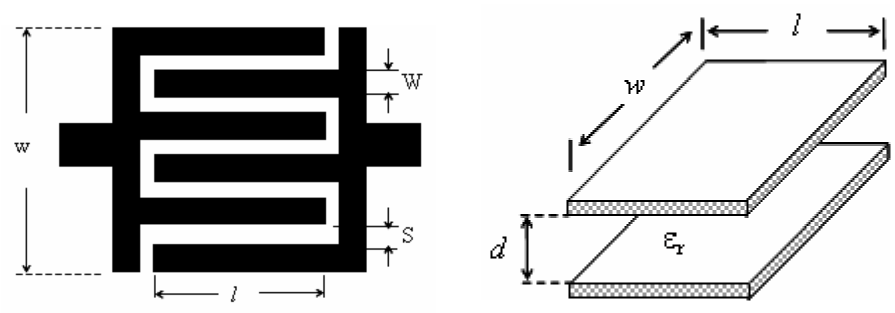

Figure 3. 21 Capacitor design with a) interdigital layout and b) parallel plate layout

MIM capacitors are designed by sandwiching a layer of dielectric between two metal plates; this design approach is frequently used in filter design. The interdigital-design consists of a number of thin parallel conducting strips of length (l) that are inter-linked alternately to give a total width (w) of the structure.

B. Capacitance

Assuming that the substrate thickness is larger than the line spacing (S), the capacitance of an interdigital-capacitor can be expressed as:

$$C_s = \frac{\varepsilon_r + 1}{w} l \left[(N-3) A_1 + A_2 \right], \tag{3.51}$$

where N is the number of Fingers, A_1 and A_2 are parameters depending on line thickness (T) and finger width (W) and finger spacing (S).

$$A_1(pF) = \left[0.334905 - 0.15287116 \left(\frac{T}{S} \right) \right]^2 \tag{3.52}$$

$$A_2(pF) = \left[0.50133101 - 0.22820444 \left(\frac{T}{S} \right) \right]^2 \tag{3.53}$$

The maximum capacitance value is limited by the physical size, and the maximum useable operating frequency is limited by the distributed nature of the fingers.

The capacitance of a metal-insulator-metal (MIM) design shape can be estimated using (3.54).

$$C_p = \varepsilon_0 \varepsilon_r \frac{A}{d} \tag{3.54}$$

where $A = l \cdot w$, is the plate area, l is the length of the plates, w is the width of the plate, d is the distance spacing between the two plates, ε_r is the relative permittivity of the dielectric between the layers.

Equations (3.54) assumes that $d \ll l$, $d \ll w$, and $\varepsilon_0 \ll \varepsilon_r$, and for multilayer-dielectric, ε_r must be replaced by the equivalent relative dielectric constant $\varepsilon_{r,\,eq}$ given in (3.45).

3.2.4 Determination of Coupling

The next step in the filter design development is the determination of coupling. There are two different types of coupling, namely the inter resonator coupling, and the input/output-ports and first/last resonators coupling between.

3.2.4.1. Inter-Resonator Coupling

The inter-resonator coupling is strongly dependent on the distance spacing between the resonators, as well as the configuration of the structures. For laterally coupled structures, the coupling depends on the edges and thickness of the structures. For vertically coupled structures, the coupling depends mainly on the dielectric thickness separating the metallization layers, and the effective coupling areas. These couplings must be accurately determined for efficient design/integration of bandpass filters.

The inter-resonator coupling ([3.1], [3.3]) can be theoretically calculated using (3.55), where g_i are the prototype element values and FBW the fractional bandwidth.

$$k_{n,n+1} = \left. \frac{FBW}{\sqrt{g_i g_{i+1}}} \right|_{i=1 \ to \ (n-1)} \tag{3.55}$$

$$K_{i,i+1} = \left. \frac{f_b^2 - f_a^2}{f_b^2 + f_a^2} \right| \tag{3.56}$$

Alternatively, this coupling can be experimentally determined through full-wave electromagnetic simulations using (3.56), where f_a and f_b are the frequencies at the peaks of the transmission response of the coupled structures.

3.2.4.2. Input/Output Coupling

The coupling between I/O-ports and first/last-resonator is related to the external quality (Q_e) and can theoretically be calculated at each port using equations (3.57), where g_0, g_1, g_n and $\mathrm{g}_{\mathrm{n}+1}$ are the prototype element values, and FBW is the fractional bandwidth, A and B denote the input/output-port, respectively.

$$\left(Q_e\right)_A = \frac{g_0 g_1}{FBW} \tag{3.57.a}$$

$$\left(Q_e\right)_B = \frac{g_n g_{n+1}}{FBW} \tag{3.57.b}$$

$$Q_e = \frac{\omega_{res} \cdot \tau_{S11}\left(\omega_{res}\right)}{4} \tag{3.58}$$

Alternatively, these quality factors can experimentally be extracted from the group delay of the reflection coefficient$\left(\tau_{S11}\right)$ at the resonant frequency [3.3], using (3.58) for single loaded resonator.

3.2.5 Design Topologies and Configurations

Table 3. 2 Different design topologies and configurations for embedded 2-pole bandpass filters

I/O-port	Lateral	Vertical with off-set	Vertical without off-set
Gap	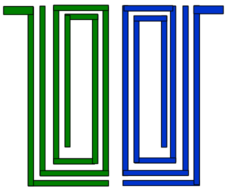 Open-end Terminal	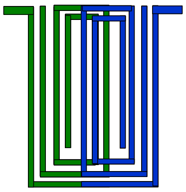 Open-end Terminal	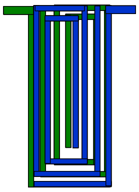 Open-end Terminal
	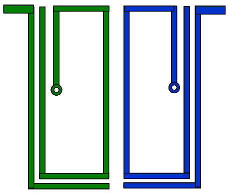 Short-end Terminal	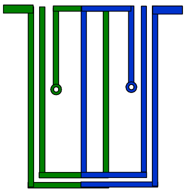 Short-end Terminal	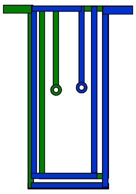 Short-end Terminal
Tap	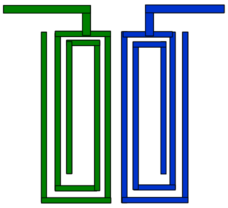 Open-end Terminal	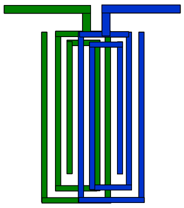 Open-end Terminal	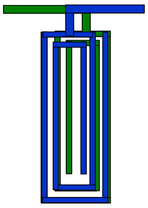 Open-end Terminal
	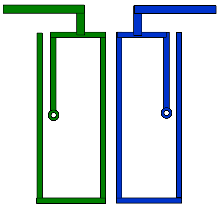 Short-end Terminal	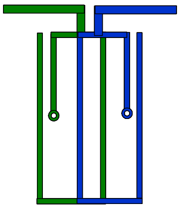 Short-end Terminal	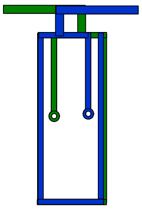 Short-end Terminal
Embedded configuration	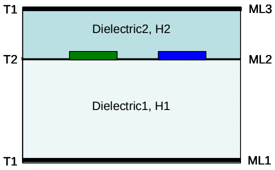 Embedded in 3 ML	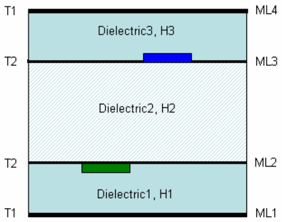 Embedded in 4 ML	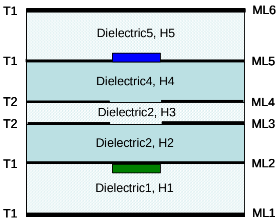 Embedded in 6 ML

Different design topologies and configurations for bandpass filters are possible (e.g., lateral, vertical, or mixed configuration, with tap or gap topology), depending on the required performances and filter size. For the implementation of second order bandpass filters, the most important design topologies/configurations are shown in Table 3.2.

"Gap topology" means that the input/output-ports coupling of the filter network is capacitive. The design realization occurs with gap-spacing.

"Tap topology" means that the input/output-ports coupling of the filter network is inductive. The design implementation occurs with tapped-line.

"Lateral configuration" means that the resonant elements are realized in the same metallization layer, where they are laterally coupled to each other.

"Vertical configuration with off-set between the resonant elements" means that the resonant elements are realized in different layers. These elements are vertically coupled to each other, and there is an off-set between them.

"Vertical configuration without off-set between resonant elements" means that the resonant elements are realized in different layers. These elements are vertically coupled to each other, and there is no off-set between them. In this design approach, ground planes designed with electromagnetic (EM) windows, are inserted between the resonant elements in such a way to control the EM coupling happening between the resonant elements.

Whichever of these design topologies/configurations is chosen, there is a trade-off between filter size, electrical performance, and development-cost.

3.3. Summary

The last main step in the design development is the fabrication and testing through RF measurements. The design approach is verified and the modeling accuracy is evaluated. The complete design flow developed for the integration and miniaturization of RF filters is summarized in Figure 3.22.

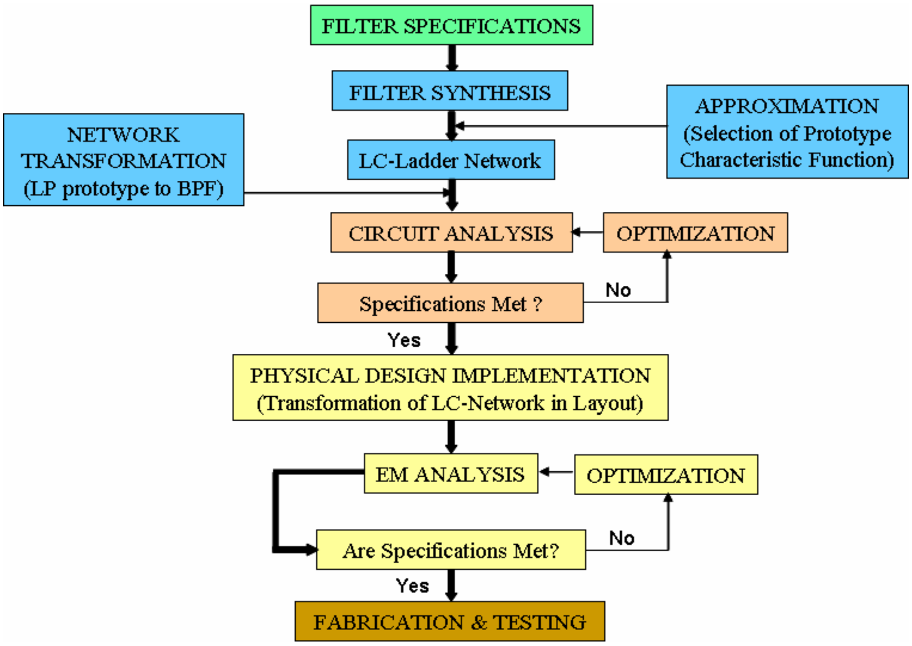

Figure 3.22 Design flow for integrated RF/microwave filters

The design and implementation of some RF filters for wireless applications are presented in the next chapter for the illustration of this design methodology.

Chapter 4

Illustration of Design Methodology

4.1. High-Frequency/High-Speed Multilayer PCB

Various constructions of high-frequency/high-speed multilayer printed-circuit-board (PCBs) with different substrate materials and in different configurations are possible, dependent on the circuit performance requirements as well as circuit miniaturization requirements. Figure 4.1 shows the example of a multilayer PCB configuration, in which bandpass filters can be embedded.

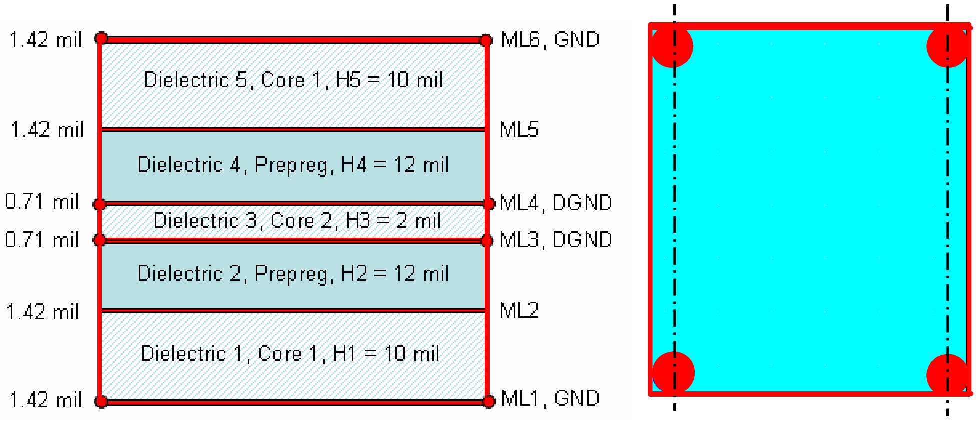

(a) **(b)**

Figure 4. 1 Multilayer organic based PCB construction a) Cross-section with inhomogeneous medium, b) Top view showing the through-vias that idealize the metallic walls

The board consists in three laminate cores, two prepregs, and six copper-metal-layers. The prepreg layer is RO4350 and is 12 mil thick; its dielectric constant (DK) and dissipation factor (DF) are 3.56 and 0.0036, respectively. The core layer 1 is RO4450 with 10 mil thickness, a DK and DF of 3.48 and 0.004, respectively. The core layer 2 is ISO620 of 2 mil thickness; with a DK and Df of 3.6 and 0.008, respectively. The metal layers are copper of conductivity $5.8 \cdot 10^{7}$ S/m. The thicknesses of the inner metal (ML3, and ML4) and the outer metal layers (ML1, ML2, ML5, ML6) are 1.42 mil and 0.71 mil, respectively.

To minimize the electromagnetic interferences (EMI) and radiations, as well as to provide mechanical strength and enhanced reliability, the filter structures are completely shielded and embedded within the inner metal layers (ML2 and ML5). But to facilitate the on-board measurements, GSG-adapters representing the interface between the device under test (DUT) and RF probes-tips are designed on the top metal layer (ML6). The outer layers (ML1 and ML6) are protected by solder masks (not shown in Figure 4.1). The fully packaged substrate has a thickness of 53.1 mils (≅1.4 mm).

Through-vias connect the ground layers; micro-vias connect the terminal of the resonant elements to the ground planes. Blind-vias connect the adapters to the input/output (I/O)-ports of the filters.

The technology processes are compatible with the standard FR-4/PWB manufacturing processes. The detailed processes can be read in [3.5]-[3.6].

4.2. Reduction of Losses in Filter Design

Generally, the energy is lost during the signal transfer in practical filters. The loss mechanism can be attributed to the reflections at the filter I/O-ports as well as to the dissipation within the filter structures and/or by radiation from the filter structures. To ensure an efficient energy transport through filter components, the source of these losses must be identified, and then reduced or totally eliminated. The approach used to tackle this issue is presented in this section.

4.2.1 Source of Losses in Microstrip Filters

In most conventional microstrip filters, there exist three different losses, namely conductor (or ohmic) losses, dielectric losses, and radiation losses. These losses can corrupt or impact the electromagnetic (EM) wave propagation in the whole component. The wave propagation constant in integrated microstrip filters can be expressed by $\gamma = \alpha + j\beta$, where $\alpha = \alpha_c + \alpha_d + \alpha_r$ represents the total attenuation constant arising from the conductor losses, dielectric losses and radiation losses. These losses can be linearly expressed in terms of the unloaded quality factor [4.1] given by:

$$\frac{1}{Q_u} = \left(\frac{1}{Q_c} + \frac{1}{Q_d} + \frac{1}{Q_r} \right) \tag{4.1}$$

where Q_c, Q_d, Q_r are the quality factors corresponding to conductor losses, dielectric losses and radiation losses, respectively.

In order to improve the filter performance, it is very important to reduce or eliminate (if possible) these losses; i.e. the quality factor must be increased.

Conductor Losses

The conductor losses result from several factors related to the metal material composing the strip, the ground plane and walls. The sources of these losses are *conductivity*, *skin effects*, and *surface roughness*. These losses can be expressed in terms of the conductor quality factor (Q_c) [4.2] given by

$$Q_c = \frac{\pi}{\alpha_c \lambda_g} \tag{4.2}$$

where λ_g is the conductor guide wavelength that can be calculated using equation (4.3), and α_c is the conductor attenuation arising from the conductor losses, which can be determined using equation (4.4) [4.3].

$$\lambda_g = \frac{c}{f_0\sqrt{\varepsilon_{req}}} \tag{4.3}$$

$$\alpha_c = \frac{8.686R_s}{Z_0W} \tag{4.4}$$

where Z_0 is the characteristic impedance of the microstrip, W is the width, and R_s represents the surface resistance of the conductor strip and ground plane, given by

$$R_s = \sqrt{\frac{\omega\mu}{2\sigma}} \tag{4.5}$$

where σ, ω and μ are the conductivity, angular frequency, and permeability, respectively.

As can be seen from these equations ((4.2)-(4.5)), conductor losses are related to many different geometry and material parameters. Thus, on the one hand, narrowing the strip decreases the overall dimensions and suppresses at the same time the higher-order modes. But, narrow strip leads to higher conductor losses. In addition, narrowing the strip while maintaining constant the characteristic impedance(Z_0) must be accompanied by a decrease in the substrate thickness(H), which could lead to more severe fabrication tolerances. And on the other hand, widening the strip decreases the conductor losses, but could lead to the increase in radiation losses, as well as increase the component size. Thus, there is a conflicting situation between the necessity to have small structures (with higher losses) and larger structures (with lower losses).

With finite conductivity, there is a non-uniform current density starting at the metal surface and decaying exponentially into the metal bulk. The so-called *skin effect* can be approximated by the skin depth(δ), and in order to minimize the conductor skin effect losses, the conductor thickness should be greater than approximately three to five times the skin depth [4.1].

Sometimes the fabrication process of real microstrip components creates scratches and bumps on the metal surfaces and the ground plane facing the substrate. The high frequency currents following the uneven surface of the substrate encounter a greater resistance compared to the case of a smooth substrate. And with increasing *surface roughness*, the length of the current path increases and, therefore, the conductor losses increase. Therefore, decreasing the surface roughness decreases the conductor surface resistance.

Dielectric Losses

The dielectric losses can be expressed in terms of the quality factor Q_d given in (4.6), where $\tan\delta$ is the dissipation factor.

$$Q_d = \frac{1}{\tan\delta} \tag{4.6}$$

$$Q_d = \frac{\pi}{\alpha_d\lambda_g} \tag{4.7}$$

Alternatively, Q_d can also be expressed by (4.7) where, α_d and λ_g are the dielectric attenuation constant, and the guide wavelength of the strip line in the propagation medium at the frequency of interest, respectively.

Generally, working with low-loss dielectric substrates helps to minimize the dielectric losses.

Radiation Losses

When filter structures are open to air, they tend to radiate energy. Thus, the radiation losses can be eliminated by completely shielding and embedding the whole structures within the integration medium. Filters designed in such configuration are not only protected from the environment, but also from the electromagnetic interference (EMI). Furthermore, the so-covered structures reflect the reality.

4.2.2 Design Measures for Reduction of Losses

In order to eliminate or reduce the losses described previously, following attempts were undertaken:

- The filter structures were embedded within the inner metallization layers (ML2 and ML5) in the PCB construction. These structures were thereby protected from the environment and prevented from the radiations and electromagnetic interferences (EMI).
- To reduce the conductor losses, the thickness of the copper strip lines was kept greater than five times the skin depth $\left(\delta_{deepth} = \sqrt{1/(\pi f \mu\sigma)}\right)$. The structures were designed with wider strip lines (W=8 mils), decreasing thereby the line resistance.
- The choice of the PCB stack up was done carefully and the construction shown in Figure 4.1 has been used for the integration of the developed filters.

There are various commercial PCB materials with different possible combination of polymers, reinforcement, and copper, resulting in a wide variety of chemical, physical and electrical properties as well as a wide variation in cost. The most important parameters are electrical and mechanical parameters, manufacturability, and cost. Electrical and mechanical characteristic relate directly to the performance. The manufacturability affects the cost as well as the quality and the reliability. Whenever, there is always a trade-off between performance and cost. Figure 4.2 shows the general material structure [4.4] in relation to the cost and performance.

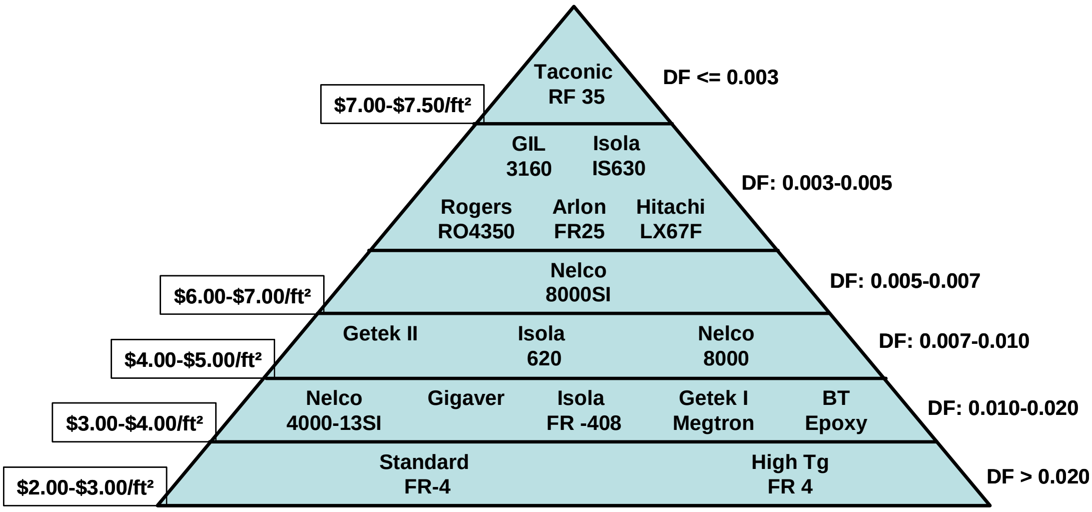

Figure 4. 2 Laminate material price and performance pyramid

The bottom of the pyramid is composed by the conventional epoxy laminates and moving upward through various blends or polymers to the polytetrafluoroethhylene (*PTFE*)-based materials at the top. The price and dissipation factor (DF) related to these materials are indicated by the left and right side of the pyramid.

- The efficient dimensioning of the filter I/O-ports is of great importance in the design development. Figure 4.3.a illustrates the board construction with material and geometry parameters. Due to the inhomogeneity of the integration medium, the filter structures have to support different waveguide modes, namely the TM-, TE-modes, and the TEM-mode.

The dominant modes emerging near the discontinuities/sources are evanescent and have reactive effects. Since the energy transport is ensured by all these modes (the TEM mode as well as the dominant TE-, and TM-modes), thus keeping the transversal and longitudinal dimension of the structures above the cut-off waveguide length (or keeping the maximum frequency of interest below the cut-off frequency) is very important.

The cut-off frequency and guide wavelength [4.5] of the dominant modes, TE^{mnp} and TM^{mnp}, are given, respectively, by

$$\left(f_c\right)^{mnp} = \frac{v_p}{\lambda_c} = \frac{1}{\sqrt{\mu\varepsilon}}\sqrt{\left(\frac{m}{2a}\right)^2+\left(\frac{n}{2b}\right)^2+\left(\frac{p}{2c}\right)^2}\left|\begin{matrix} m=0,1,2,\ldots \\ n=0,1,2,\ldots \\ p=1,2,3,\ldots \end{matrix}\right\} m=n\neq 0 \tag{4.8}$$

$$\left(\lambda_c\right)^{mnp} = \frac{1}{\sqrt{\left(\frac{m}{2a}\right)^2+\left(\frac{n}{2b}\right)^2+\left(\frac{p}{2c}\right)^2}}\left|\begin{matrix} m=0,1,2,\ldots \\ n=0,1,2,\ldots \\ p=1,2,3,\ldots \end{matrix}\right\} m=n\neq 0 \tag{4.9}$$

where the subscripts m, n refer to the mode numbers, and p refers to the number of one-half sinusoidal variations of the fields along the dimension c of the PCB construction, with $c = p\cdot\left(\lambda_g/2\right)$. In this construction, the metallic walls are idealized through the through-vias (as shown previously in Figure 4.1.b).

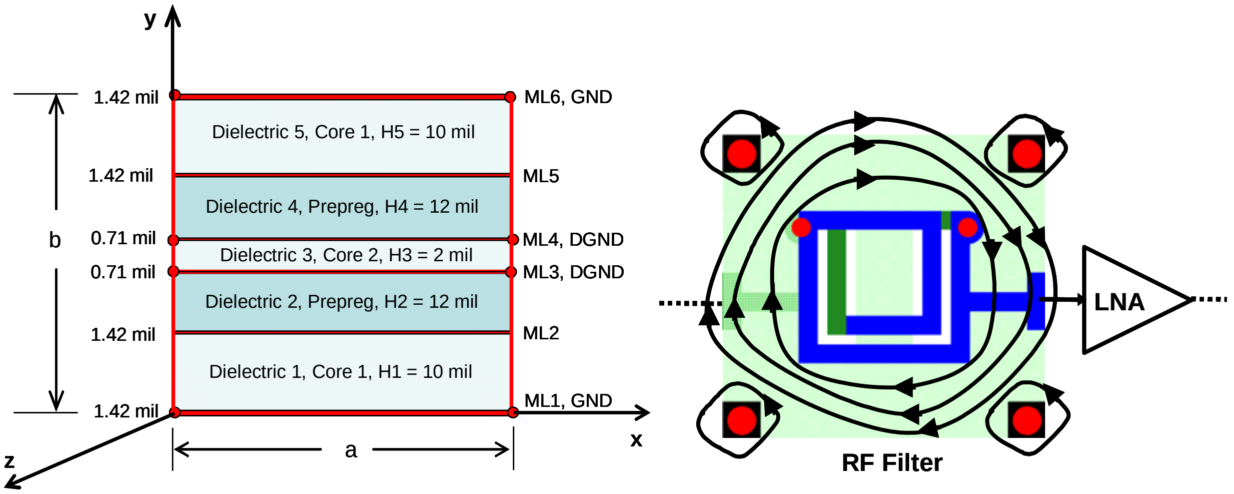

(a) (b)

Figure 4. 3 a) Cross-sectional view of the PCB stack-up including the design parameters, b) Sketch of the TEM mode showing the magnetic field lines structures in an embedded RF filter

By dimensioning the filter structures, $\left(f_c\right)^{mnp}$ for the lowest modes number that are $\left(1,0,1\right)$ for TE-modes and $\left(1,1,0\right)$ for TM-modes and by assuming that $c > a > b$, was determined:

$$\left(f_c\right)_{TE}^{110} = \frac{1}{\sqrt{\mu\varepsilon}}\sqrt{\left(\frac{1}{2a}\right)^2 + \left(\frac{1}{2b}\right)^2} = \frac{1}{2a\sqrt{\mu\varepsilon}}\sqrt{1+\left(\frac{a}{b}\right)^2} = \frac{1}{2a\sqrt{\mu\varepsilon}}\sqrt{1+\left(\frac{1}{k}\right)^2} \tag{4.10}$$

where the dimension $b = k \cdot a$ and k is the constant of proportionality between the lateral and vertical transversal dimensions.

The maximum frequency is the mesh frequency that was predefined in this PCB construction to f_{mesh}=10 GHz; this frequency was equated to $\left(f_c\right)_{TE}^{110}$. Thus the thickness of the PCB construction is b=53.1 mil and the equivalent dielectric constant of the construction is $\varepsilon_{r,eq} \simeq 3.5$.

From these parameters, the minimal (lateral transversal) dimension of the PCB construction was determined.

Similarly, $\left(f_c\right)_{TE}^{101}$ was determined:

$$\left(f_c\right)_{TE}^{101} = \frac{1}{\sqrt{\mu\varepsilon_{r,\,eq}}}\sqrt{\left(\frac{1}{2a}\right)^2 + \left(\frac{1}{2c}\right)^2} = \frac{1}{2a\sqrt{\mu\varepsilon_{r,\,eq}}}\sqrt{1+\left(\frac{1}{k}\right)^2} \tag{4.11}$$

where the dimension $c = k \cdot a$ and k is the constant of proportionality between the dimension of the structure in the wave propagation direction and the transversal dimension. The highest frequency in this design is the mesh frequency (f_{mesh}). Since the operating frequencies are below the cut-off frequency, the coupling due to the radiation is therewith minimized.

However, it is important to note that the shielding efficiency based on the through-vias metallic walls idealization is of course not perfect, since a rest-radiation of the TEM-wave could occur through the inter-through-vias spacings, as shown in Figure 4.3.b. According to this figure, the wave radiation could hit upon other neighbouring devices such as the low noise amplifier (LNA).

Thus, restricted on this idealization, the filter structures were efficiently dimensioned, therefore preventing an optimum energy transfer through the filter input/output ports.

4.3. Examples of Bandpass Filters for Wi-Fi Applications

4.3.1 Definitions

Wi-Fi, referred to Wireless-Fidelity, is a certification mark for equipment based on a different set of IEEE standards from the 802.11 working group for wireless local area networks (WLAN) [4.6]. Neither WiMAX nor Wi-Fi are technologies but their names have been adopted in popular usage to denote the technologies behind them. These standards were designed to achieve wireless communications providing a data rate of 54 Mb/s at 100 m distance.

In terms of spectrum, Wi-Fi system operates around 2.4 GHz in an ISM (Industrial Scientific Medicine) band ranging from 2400 MHz up to 2483 MHz with a frequency hopping spread spectrum system using gauss frequency shifting keying (GFSK) modulation, as well as around 5 GHz in an UISM (Unlicensed Industrial Scientific Medicine) band ranging from 5250 MHz up to 5350 MHz, and from 5725 MHz up to 5850 MHz.

In the 2.4 GHz ISM band, Wi-Fi coexists with Bluetooth and it has demonstrated robust service for WLANs.

4.3.2 Filter Design Specifications and Responses

For the specifications, these parameters were used: center frequency f_0 = 2.4 GHz, passband width BW = 100 MHz, passband ripples of 0.1 dB, passband return loss RL ≤ -20 dB, source/load impedance of 50 ohms. Various functions can be used to approximate this filter; examples of these functions are Butterworth, Chebyshev, Elliptic, Bessel-Thomson, Gaussian, etc. The approximation with Butterworth and Chebyshev function responses is presented in the following for the illustration.

Butterworth 3rd Order

The synthesized LC-circuit network of the bandpass filter using this function is shown in Figure 4.4.a, where the network elements are L_{s1} = 26.5 nH, C_{s1} = 165.18 fF, L_{p2} = 202.48 pH, C_{p2} = 21.20 pF, L_{s3} = 26.50 nH, C_{s3} = 165.18 fF.

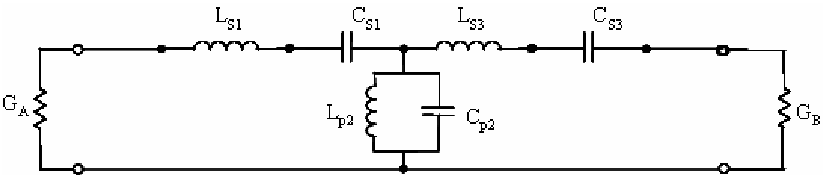

(a)

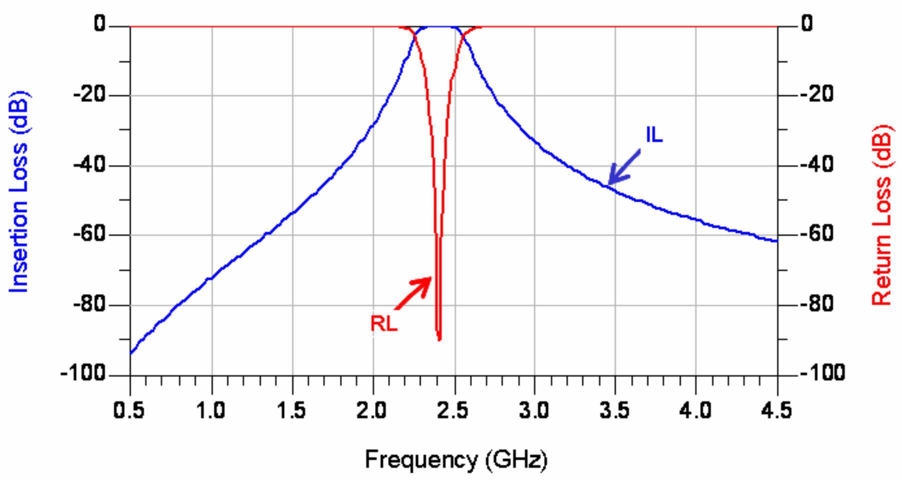

(b)

Figure 4. 4 Butterworth 3rd order bandpass filter a) LC-circuit network and b) filter responses

The simulation responses of this bandpass filter are shown in Figure 4.4.b in terms of insertion loss (IL) and return loss (RL).

Chebyshev 2nd Order

The next example shows the 2nd order Chebyshev approximation of the so-specified bandpass filter. The synthesized LC-circuit network of this filter is shown in Figure 4.5.a, where the network elements are L_{s1} = 82.27 nH, C_{s1} = 53.22 fF, L_{p2} = 772.92 pH, and C_{p2} = 5.66 pF, respectively.

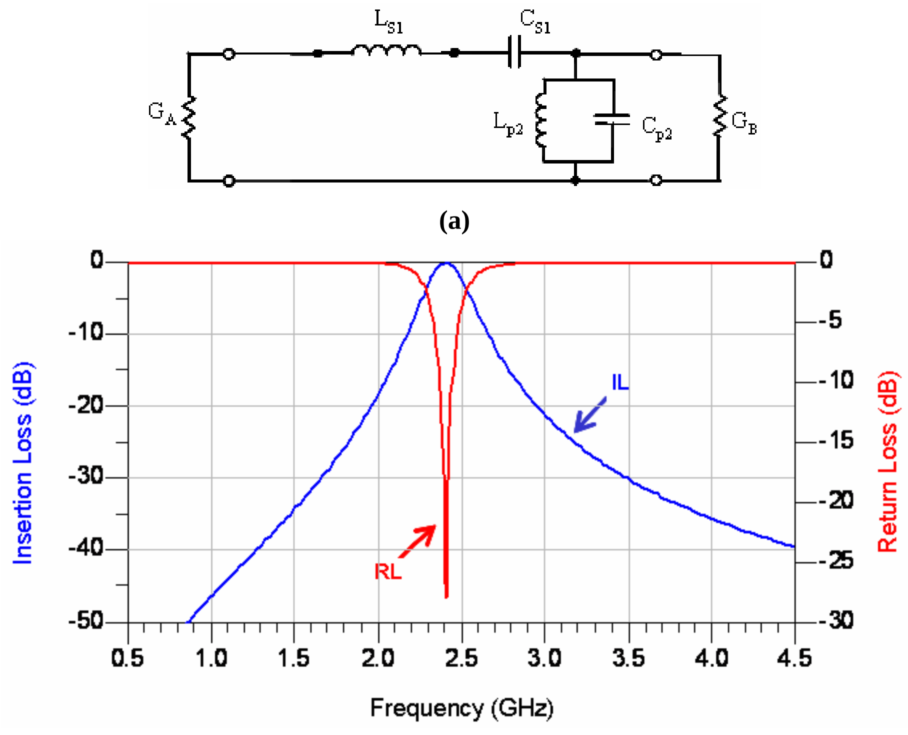

(a)

(b)

Figure 4. 5 Chebyshev 2nd order BPF a) LC-circuit network and b) filter responses

The simulation responses of this filter are shown in Figure 4.5.b in terms of insertion loss and return loss. As can be seen, the synthesis of the so-specified bandpass filter requires at least 2 poles ($n \geq 2$) LC network. As a practical measure, the higher the number of poles, the better is the selectivity but at the expense of the filter sensitivity. But in all cases, designers have to make a trade-off between sensitivity and selectivity.

The next section will present the design implementation of a 2nd order Chebyshev bandpass filter.

4.3.3 Implementation of a 2.4 GHz Chebyshev Bandpass Filter

The so-specified filter can be approximated by the 2nd order Chebyshev function, whose lowpass prototype elements are $g_0 = 1$, $g_1 = 0.8431$, $g_2 = 0.6220$, $g_3 = g_{n+1} = 1.3554$. Based on the filter designed theory given by Matthaei [3.1], the LC network of Figure 4.6.b was synthesized, where the network elements are L_{s1} = 82.27 nH, C_{s1} = 53.22 fF, L_{p2} = 772.92 pH, and C_{p2} = 5.66 pF. But for the easy implementation of this filter, the synthesized LC network was simplified by means of I/O-port matching network and J-inverter into a capacitively coupled LC network with either capacitive I/O-ports (that we call gap topology), or inductive I/O-ports (that we call tap topology). These designs approaches are shown in Figure 4.6.d and Figure 4.6.e, respectively.

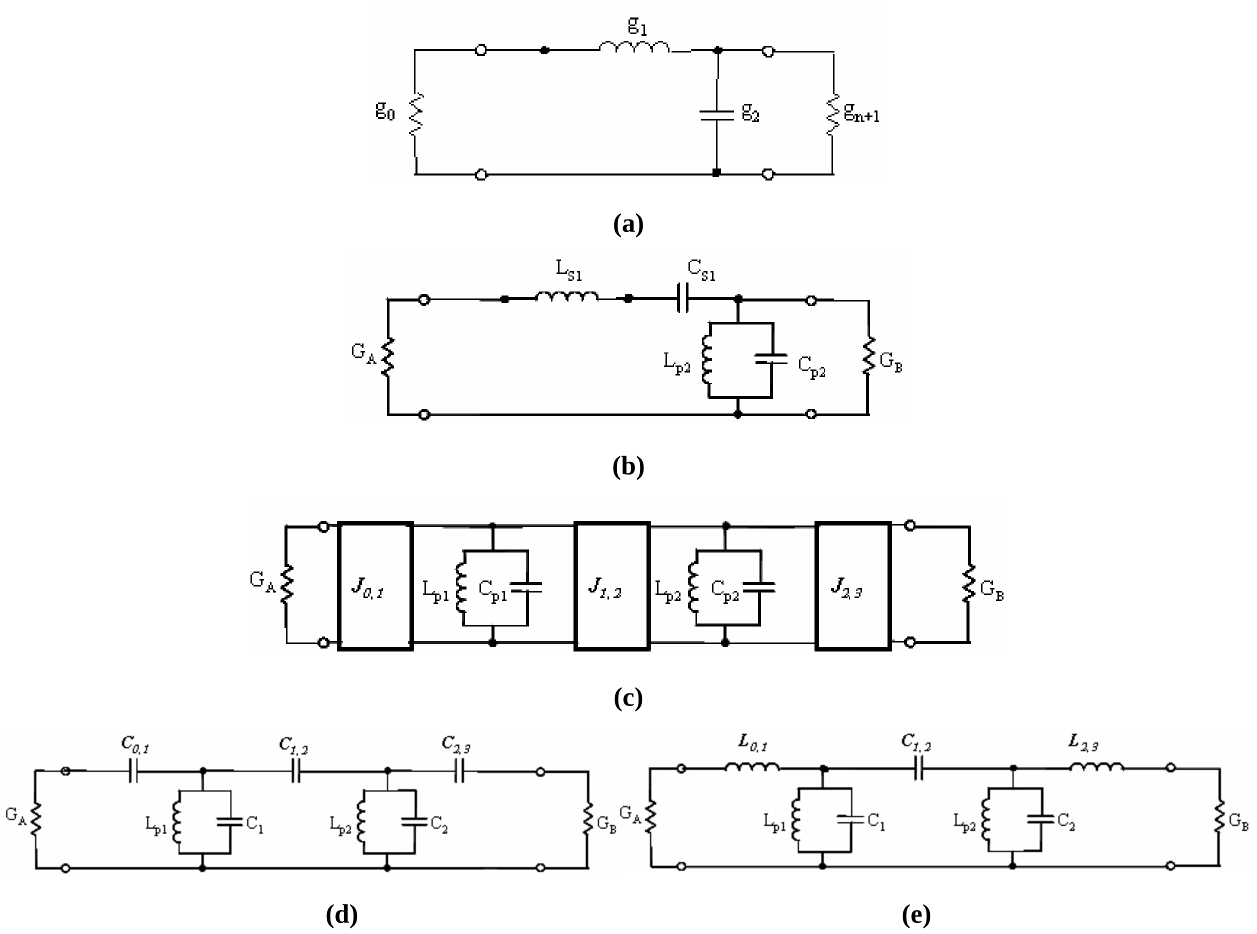

(a)

(b)

(c)

(d) (e)

Figure 4. 6 Synthesized LC-network for a 2-pole bandpass filter

Based on the gap topology for example, the so-specified 2.4 GHz bandpass filter was then embedded in a multilayer PCB configuration of Figure 4.1. Each LC element of the network was approximated by a short-terminated square-shaped spiral inductor, whose shortest electrical length was $\pi/2$, and by using (3.44) the physical length was 608 mil. Its size (in XY-directions) was 100 mil x 92 mil. The line width (W) and space (S) were 8 mil and 4 mil, respectively. The layout of the spiral inductor and the simulation responses are shown in Figure 4.7.

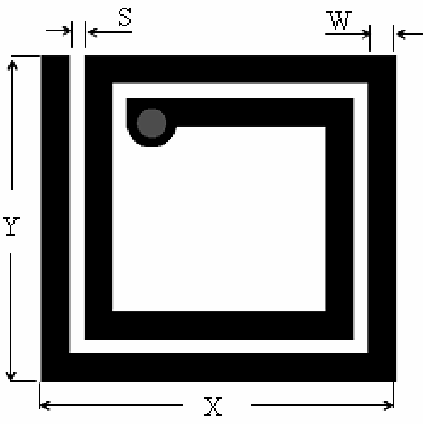

(a)

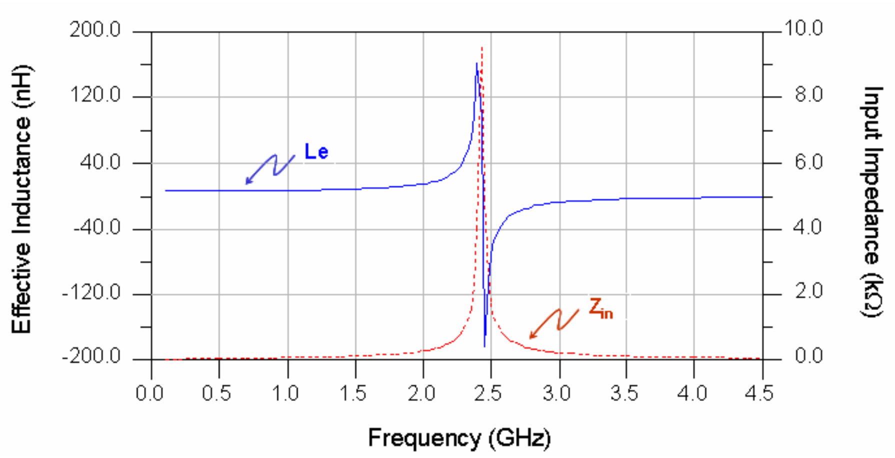

(b)

Figure 4.7 a) Layout of the spiral resonant inductor and b) its simulated responses

The so-dimensioned inductor offered an effective inductance (read at 100 MHz) of 5.37 nH and an unloaded quality factor (Q_u) of 48.4.

The input/output-port coupling, which is related to the external quality factor (Q_e), was theoretically calculated using (3.37) and experimentally determined using (3.38). Table 4.1 shows the Q_e values in dependence of the gap-spacing (S). The optimal gap-spacing was found by 4 mil, which matches to $Q_e = 20.40$.

Table 4.1 Experimental determination of the external quality factor for different gap-spacings

S [mil]	1	2	3	4	5	6	7	8	9	10
Qe	1.81	4.42	10.80	20.40	14.94	7.70	4.47	2.84	1.97	1.45

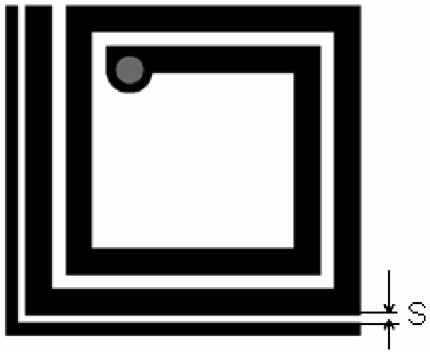

Figure 4. 8 Experimental determination of the external quality factor

After determining the optimal gap spacing, the inter-resonators coupling ($K_{1,2}$) was calculated and the 2.4 GHz bandpass filter was implemented in two different design topologies, namely, the "vertical configuration with off-set between the resonant elements" that we call "filter C3", and the "vertical configuration without off-set between the resonant elements" that we call "filter C4".

Implementation of Filter C3

The layout and substrate cross-section of this design approach are shown in Figure 4.9. The optimal off-set between the resonant elements was determined to G = 60 mil. The total size of filter C3 (in XY-directions) was 234 x 168 mil² incl. all proximity areas.

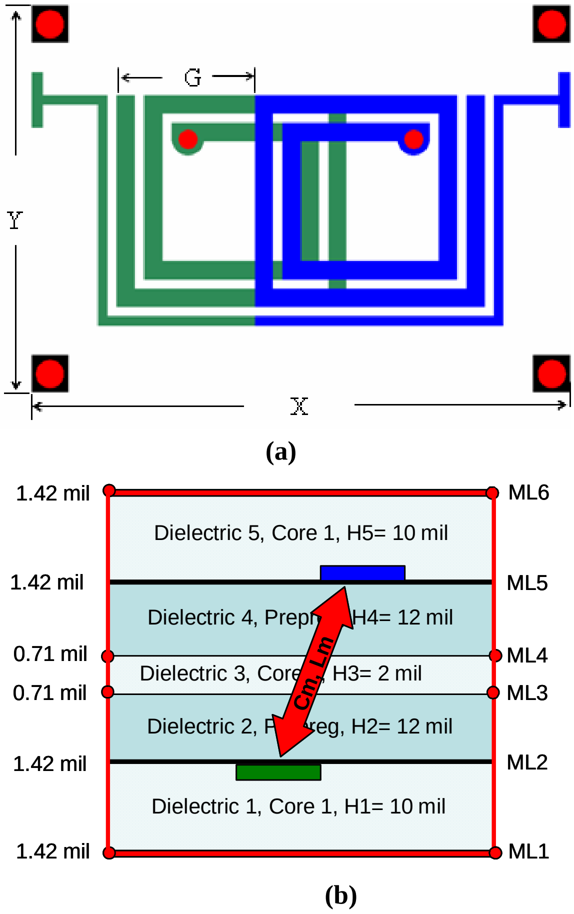

Figure 4. 9 a) Layout and b) substrate cross-section of filter C3

The simulation responses of this filter are shown in Figure 4.10, in terms of insertion loss (IL) and return loss (RL).

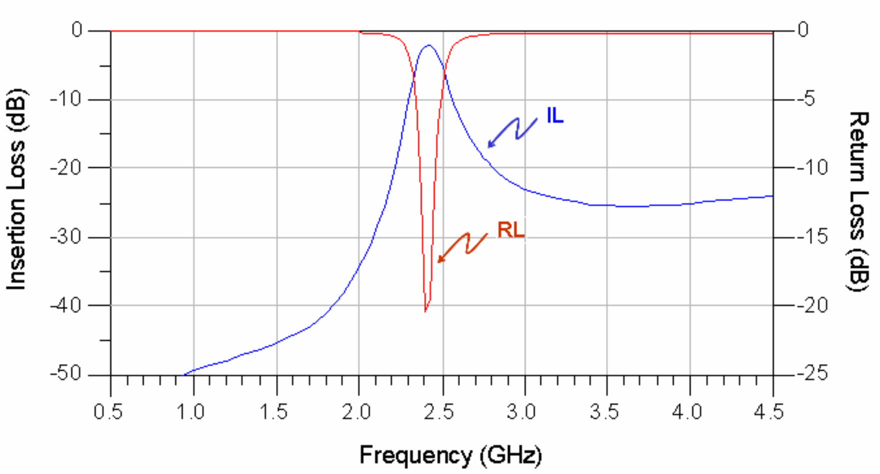

Figure 4. 10 Simulation responses of filter C3

As shown in this figure, the simulated IL and RL values at midband frequency of 2.4 GHz are -2.1 dB and -19.4 dB, respectively.

Implementation of Filter C4

In order to decrease the filter size, the resonant elements were arranged in a vertical topology without any off-set between them. Ground planes designed with electromagnetic (EM) window of size 76 x 68 mil² (in AB-directions) were inserted between the resonant elements in such a way to control the EM coupling between these resonators. The total size of filter C4 (in XY-directions) was 174 x 168 mil², incl. all proximity areas.

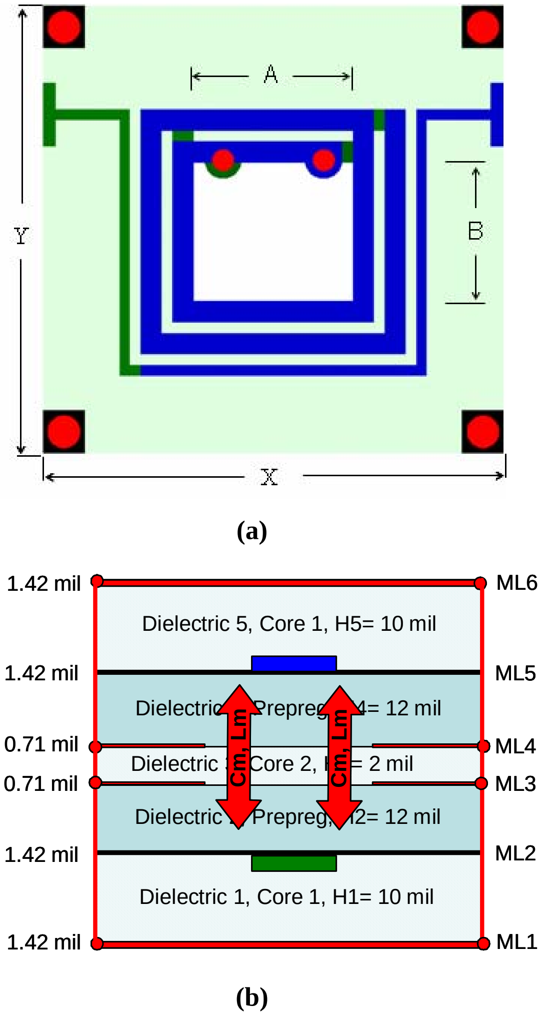

(a)

(b)

Figure 4.11 a) Layout-view and b) substrate cross-section of filter C4

The layout and substrate cross-section of this design approach are shown in Figure 4.11. The simulation responses are shown in Figure 4.12 in terms of insertion loss and return loss.

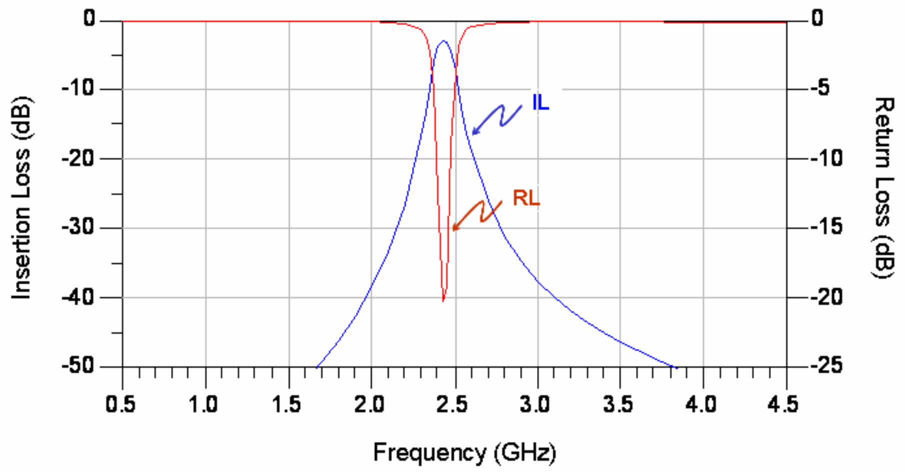

Figure 4. 12 Simulation responses of filter C4

As can be seen, the simulated IL and RL values are -3.0 dB and -20.27 dB, respectively, at the midband frequency of 2.4 GHz.

Comparison between Filter C3 and Filter C4

In order to evaluate the efficiency of this design approach in terms of the miniaturization and electrical performance, the size and simulation responses of these filters are compared. The size of filter C3 was 234 x 168 mil², whereas the size of filter C4 was 174 x 168 mil². This comparison shows that a size reduction of more than 25 % was obtained. The simulation responses of these filters are plotted in Figure 4.13 for the comparison. As can be seen, there is a discrepancy in terms of filter attenuation within the upper stopband.

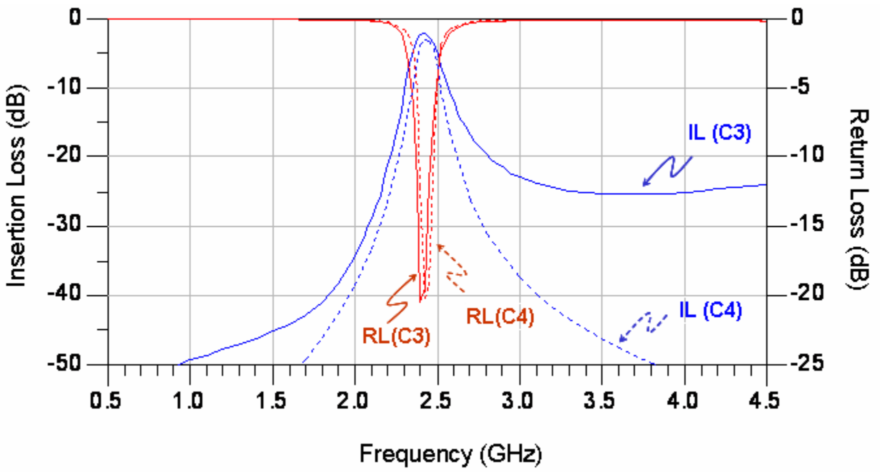

Figure 4. 13 Simulation responses of filter C3 and filter C4

Within the lower stopband, the attenuation of both the filters is nearly identical, while within the upper stopband, filter C4 exhibits the better characteristics that can be attributed to the frequency–dependent coupling. The slightly higher insertion loss of -3.0 dB in filter C4 can be attributed to the additional conductor losses coming from the ground planes.

4.4. Examples of Bandpass Filters for WiMAX Applications

4.4.1 Definitions and Transceiver Requirements

WiMAX, the acronym that stands for Worldwide Interoperability for Microwave Access, is a certification mark for products that pass conformity and interoperability tests for the IEEE 802.16 standards and is officially known as wireless metropolitan area network (WMAN) [4.6].

The spectra covered by WiMAX are available and allocated in various licensed and unlicensed bands. The licensed bands are those that are currently “owned” by carriers that have paid for the use of the bands. Unlicensed bands are freely available for any experimental or enterprise application. There is no uniform global licensed spectrum for WiMAX. Worldwide, the most likely bands used will be around 2.3/2.5 GHz, 3.5 GHz, or 5 GHz, with 2.3/2.5 GHz probably being most important in Asia.

2.3 GHz band: The two wireless communications service (WCS) bands are twin 15 MHz slots, 2305-2320 MHz and 2345-2360 MHz. The 25 MHz gap between these bands is assigned to the digital audio radio service (DARS).

2.5 GHz band: The multi-channel multipoint distribution service (MMDS) spectrum includes 31 channels of 6 MHz spacing in the 2500 MHz - 2690 MHz range and includes the instructional television fixed service (ITFS). The spectrum is extended into the 2700 MHz-2900 MHz range.

3.5 GHz band: The 3.5 GHz band is a licensed spectrum available for broadband wireless access (BWA) use in many European and Asian countries. It is the most heavily-allocated band representing the largest global BWA market. Covering 200 MHz of bandwidth, from 3.4 GHz up to 3.6 GHz, this band offers great flexibility for large-pipeline backhauling to WMAN services. With this licensed spectrum, major carriers will be able to offer competitive subscriber fees through the economy of scale and the lower equipment costs that WiMAX certification brings.

5 GHz band: The unlicensed national information infrastructure (U-NII) band covers the spectrum 5725-5850 MHz with 125 MHz bandwidth. This is an industrial scientific and medical (U-NII/ISM) band. Most WiMAX activities are in the upper U-NII/ISM band because there are fewer competing services and less interference there.

Generally, the WiMAX transceivers in the 2 GHz - 11 GHz range must have a dynamic power control range of at least 50 dB in no less than 1 dB steps with high accuracy within ±1.5 dB over a 30 dB range or ±3 dB over any range greater than the 30 dB range.

As specified by the WiMAX standard, receiver level specifications are the same across the centimeter bands, 2 GHz to 11 GHz. The receiver must be able to accurately decode an on-channel signal of -30dBm (1 μW) maximum and must be able to tolerate a signal as strong as 0 dBm (0.001 μW) at the receiver input without damage to the front-end. In addition, the receiver should be able to provide a minimum image rejection of 60 dB. The WiMAX standard specifies that “the image rejection requirement be inclusive of all image terms originating at the receiver RF and subsequent intermediate frequencies”.

4.4.2 Filter Design Specifications and Responses

For the following specifications (center frequency f_0 = 5.2 GHz, passband width BW = 100 MHz, passband ripple of 0.1 dB, passband return loss RL $\leq$ 20 dB, source/load impedance of 50 ohms) various functions can be used to approximate this filter. The Chebyshev bandpass filter is presented as follows.

Chebyshev 2nd Order

The resulting LC-circuit network and the simulation responses are shown in Figure 4.14.

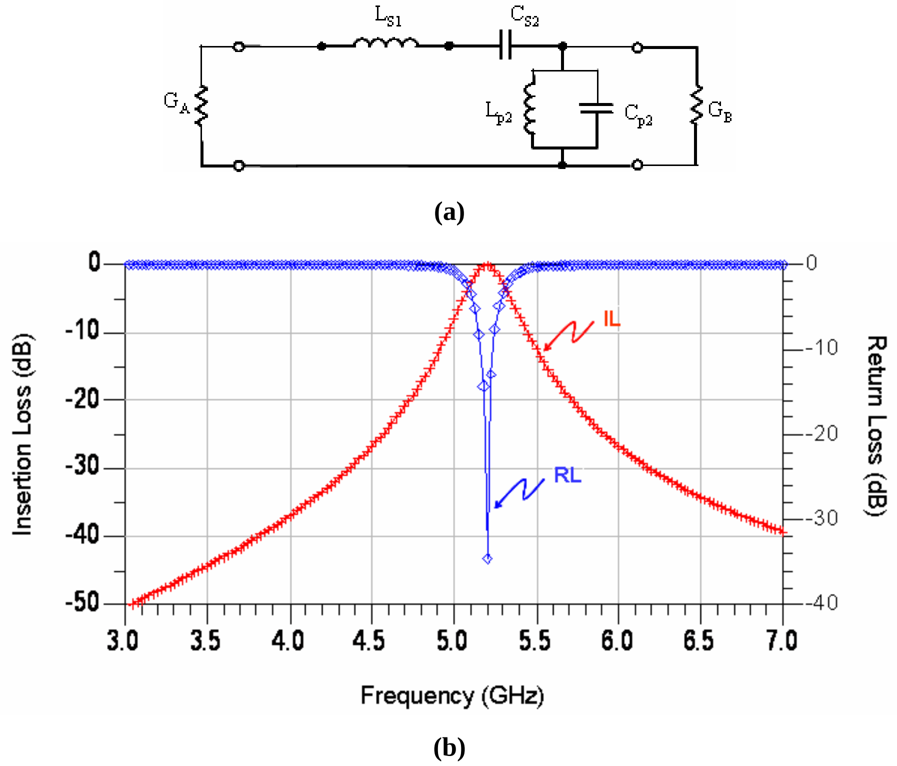

Figure 4. 14 Chebyshev 2nd order bandpass filter a) LC-circuit network and b) filter responses

The values of the network elements are L_{s1} = 82.27 nH, C_{s1} = 11.40 fF, L_{p2} = 165.52 pH, and C_{p2} = 5.66 pF, respectively. The design implementation of this filter is presented in the next section.

4.4.3 Implementation of a 5.2 GHz Chebyshev Bandpass Filter

The synthesized LC-network of the 2-pole Chebyshev bandpass filter can be simplified to a capacitive coupled LC-resonant network with capacitive I/O-port (gap topology) or inductive I/O-ports (tap topology) as shown in Figure 4.16. The prototype elements values are g_0 = 1, g_1 = 1.8219, g_2 = 0.6850, g_3 = g_{n+1} = 2.6599.

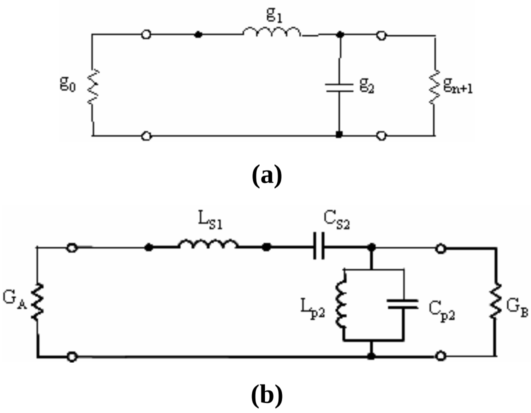

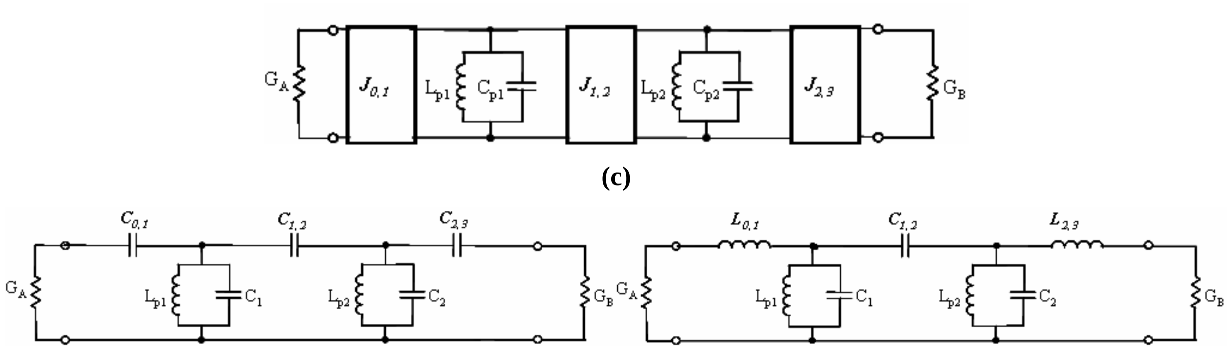

(c)

(d) (e)

Figure 4. 15 Design flow for the 2-pole 5.2 GHz bandpass filter

Based on the tap topology for example, the so-specified 5.2 GHz bandpass filter was realized. Each parallel LC element was approximated by a short-terminated spiral inductor, whose shortest electrical length was $\pi/2$, and whose physical length was 322 mil. The inductor size was 72 mil x 64 mil (in XY-directions). The line width (W) and space (S) were 8 mil and 4 mil, respectively. The layout of this spiral inductor is shown in Figure 4.16.a.

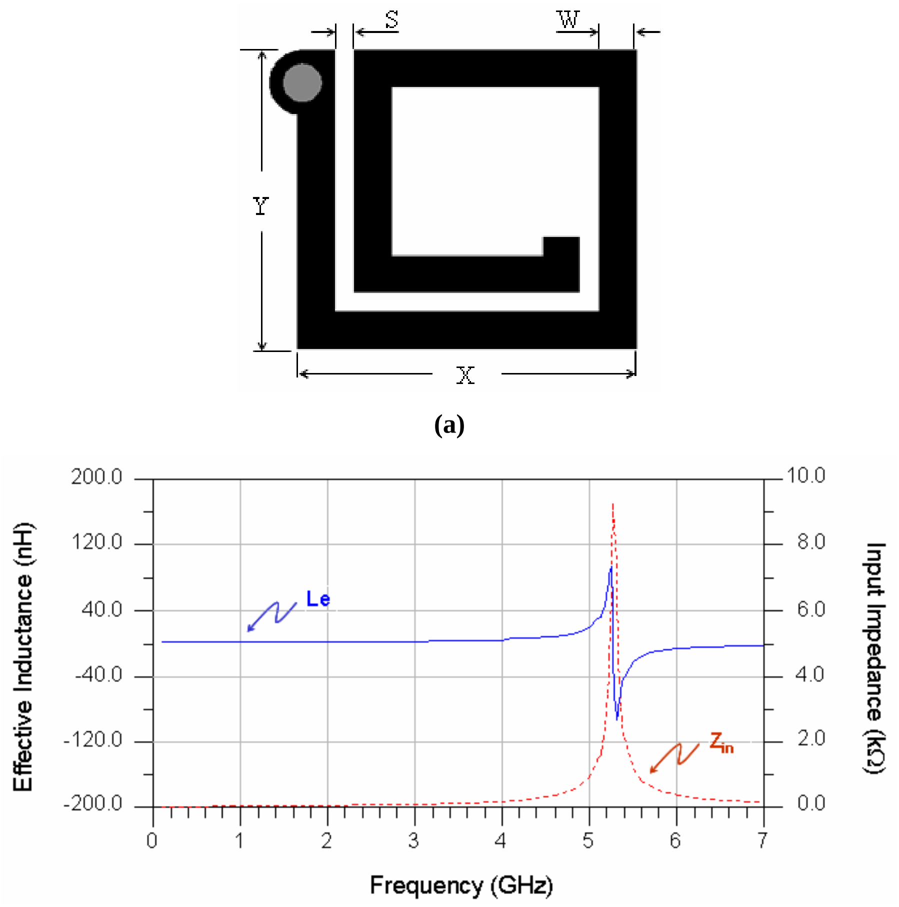

(a)

(b)

Figure 4. 16 a) Inductor layout, b) simulated input impedance and effective inductance

The simulated frequency-dependent effective inductance L_e and the unloaded quality factor $\left(Q_u = f_{res}/BW\right)$ were 3.4 nH (read at 100 MHz) and 16.7, respectively. This Q-factor was calculated from the input impedance (Z_{in}) at resonance. These parameters are plotted in Figure 4.16.b.

The I/O-port coupling is related to the external quality factor, which is dependent on the tap-location (T) on the first/last resonator, as illustrated in Figure 4.17.

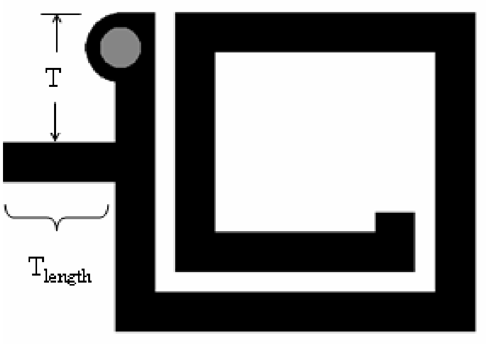

Figure 4. 17 Tap location on I/O-resonator

This Q_e was experimentally determined for different tap-line location (T). The determined values are given in Table 4.2 and plotted in Figure 4.18.

Table 4.2 Experimental determination of tap-line location (T) and external quality factor (Q_e)

T [mil]	21	25	26	27	29	33	37	45	49	53	61	69	77	85
Q_e	78.09	51.98	49.26	46.54	41.19	32.37	26.11	17.96	14.75	11.12	9.63	8.18	6.92	5.93

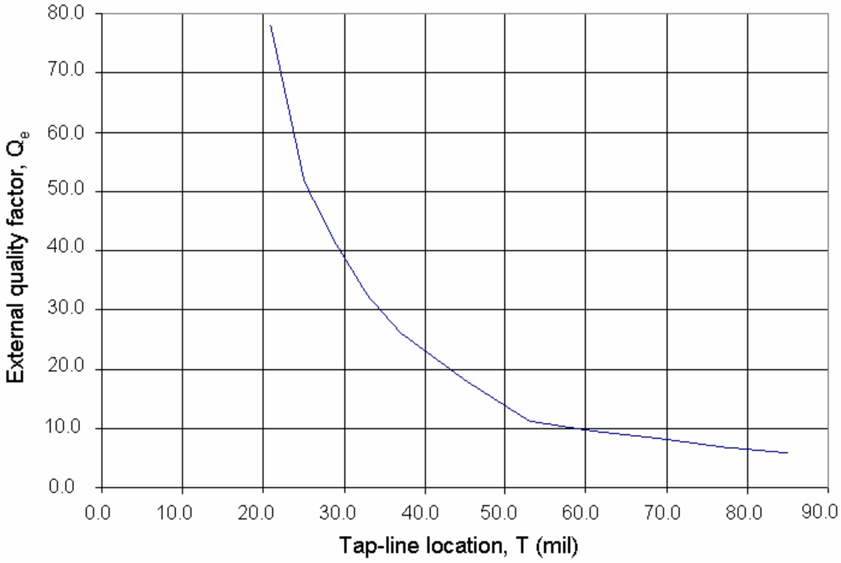

Figure 4. 18 Experimental determination of tap-line location (T) and external quality factor (Q_e),

The appropriate tap-location (T) was found at 23 mil, which corresponds to the external quality factor (Q_e) of about 55. The optimal tap-line length (T_{length}) was calculated to 34 mil.

After the dimensioning of the structures, the next step is the implementation of the whole design. The 5.2 GHz bandpass filter was implemented in two different design configurations, namely “vertical configuration with off-set between the resonant elements” that we call “filter J1”, and “vertical configuration without off-set between the resonant elements” that we call “filter J2”.

Design Implementation of Filter J1

The coupling between the resonant elements in this filter was calculated theoretically using equation (3.55) with the result of $K_{1,2} = 0.017$. The optimal off-set (G) between the resonant elements was determined to G = 70 mil. The filter size was 206 x 128 mil² (in XY-directions). The substrate cross-section and layout of this filter are shown in Figure 4.19.

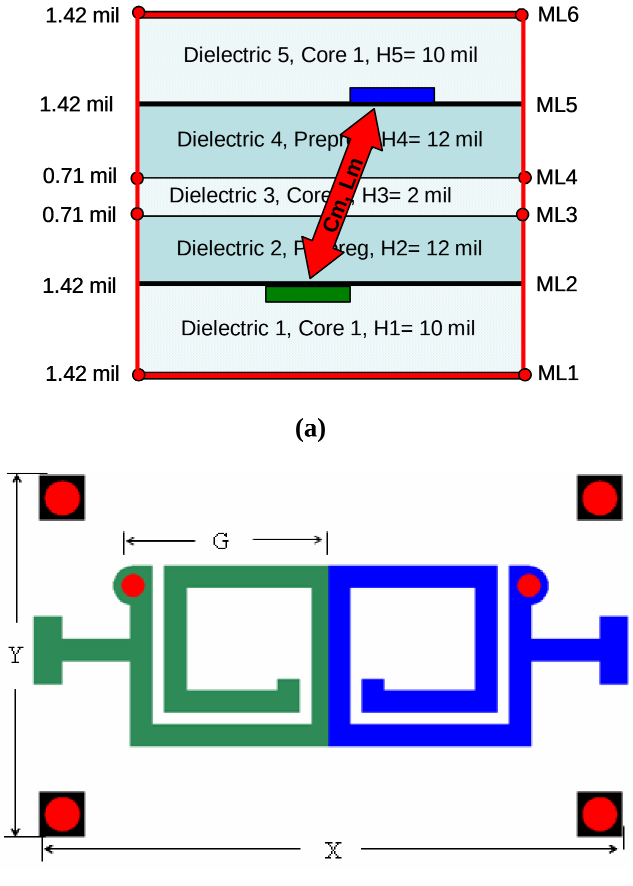

(a)

(b)

Figure 4. 19 a) Substrate cross-section and b) layout of filter J1

The coupling for different off-set was experimentally calculated, listed in Table 4.3 and plotted in Figure 4.20.

Table 4.3 Experimental determination of inter-resonator coupling

Off-set G [mil]	48	52	56	64	68	70
$K_{1,2}$	0.093	0.073	0.063	0.034	0.025	0.015

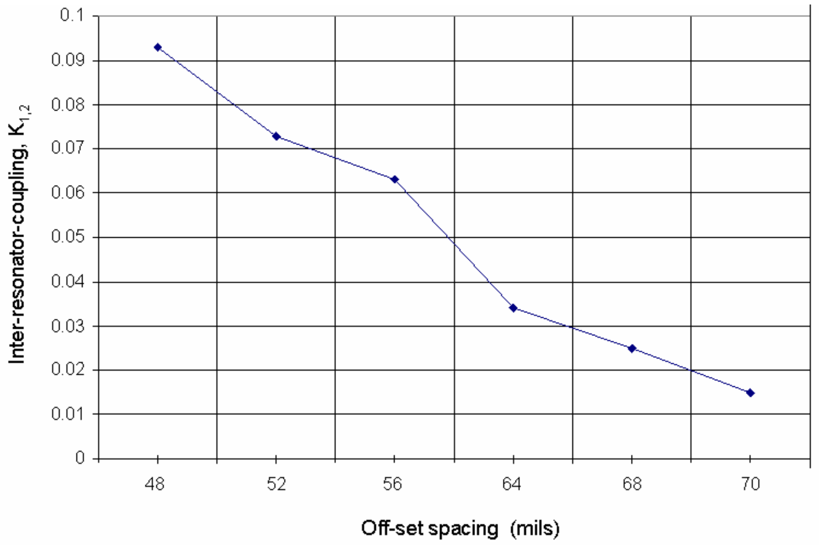

Figure 4. 20 Experimental determination of inter-resonator coupling ($K_{1,2}$)

The simulation responses are shown in Figure 4.21 in terms of insertion loss and return loss.

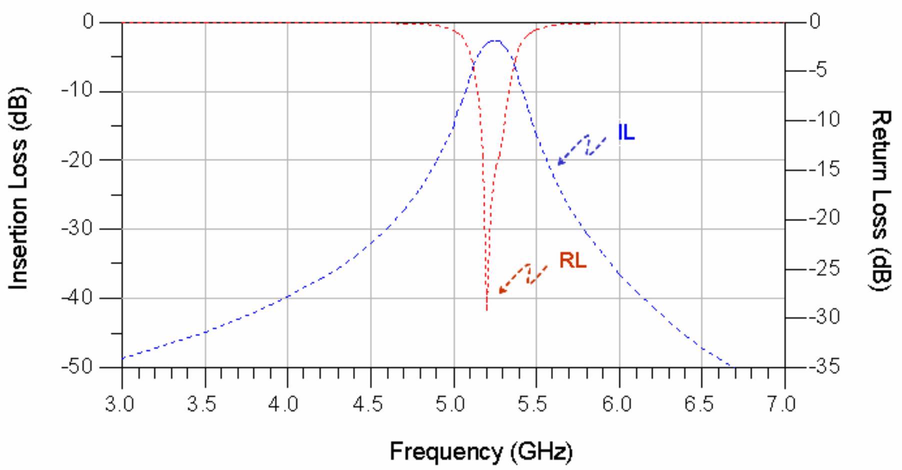

Figure 4. 21 Simulated responses of filter J1

As can be seen, this filter exhibits an insertion loss and return loss of -2.8 dB and -14.6 dB, respectively, at the midband frequency f_0 = 5.2 GHz.

Design Implementation of Filter J2

In order to decrease the size of this filter, its structures were arranged in a vertical topology without offset between the resonant elements. Ground planes designed with electromagnetic (EM) windows of size 48 x 64 mil² (in AB-directions) were placed between the resonant elements in such a way to control the EM coupling that happen between the resonant elements. This design configuration is shown in Figure 4.22.

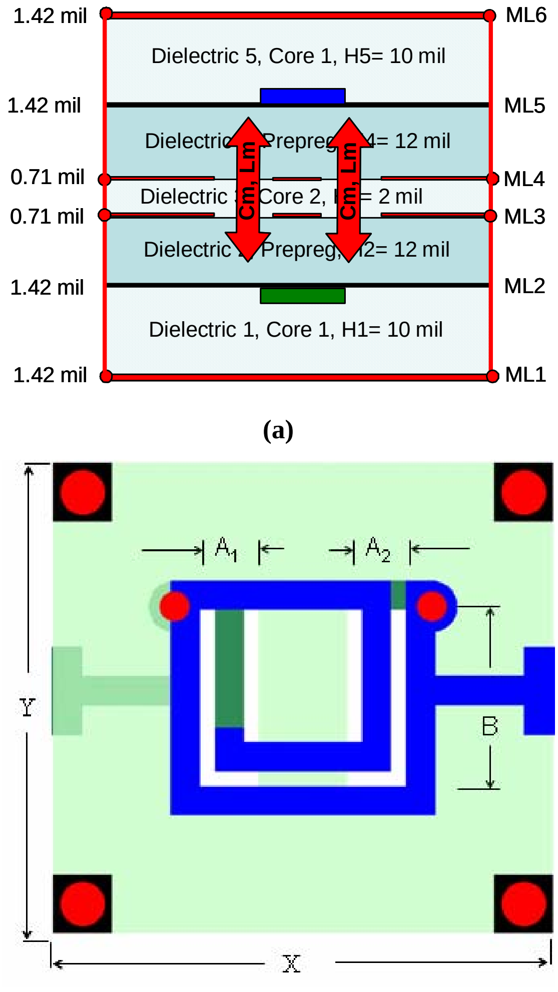

(a)

(b)

Figure 4. 22 a) Substrate cross-section and b) layout of filter J2

The filter size (in XY-directions) was 124 x 131 mil^2 and the simulation responses of this design are shown in Figure 4.24 in terms of insertion loss (IL) and return loss (RL), respectively.

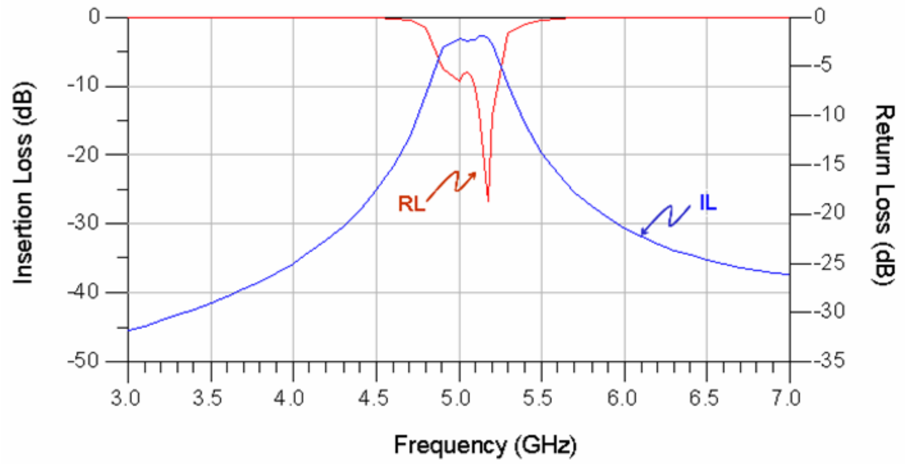

Figure 4. 23 Simulation responses of filter J2

The simulated insertion loss and return loss at the midband frequency of 5.13 GHz are 2.8 dB and 9.5 dB, respectively.

Comparison between Filter J1 and Filter J2

The size of filter J1 was 206 x 128 mil², whereas the size of filter J2 was 136 x 128 mil². The comparison shows that a size reduction of more than 33 % was obtained.

The simulation responses for both the filter J1 and filter J2 are shown in Figure 4.24 in terms of IL and RL. As can be seen in this figure, there is a shift between both the design approaches for the center frequencies of about 80 MHz. This shift can be attributed to the decrease of parasitics EM fields in the structures of filter J2, which lead to the decrease in the physical length of the filter structures.

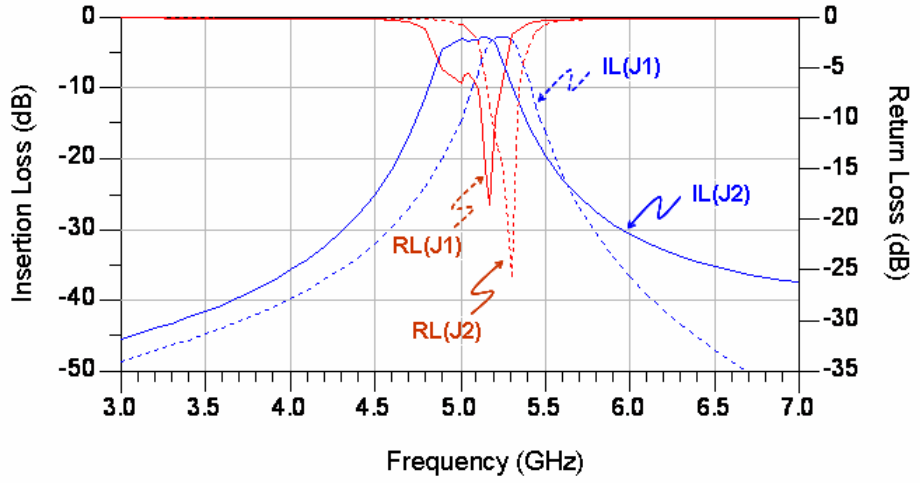

Figure 4. 24 Simulated responses of filter J1 and filter J2

However, the characteristics of both the filters are the same within the passband. Within the upper stopband, filter J1 exhibits better attenuation, due to the frequency-dependent coupling between the resonant elements.

4.5. Sensitivity Analysis for Filter Design Parameters

The objective of this analysis is to know the effect of variations in design parameters on the characteristics of the embedded filters. The design parameters such as metal conductivity, metal thickness, core and prepreg thickness, as well as core and prepreg dielectric constant were varied relative to their nominal values, and the effects of these variations on filter electrical parameters such as center frequency, insertion loss, return loss, as well as bandwidth were studied. The impact of the design topologies and configurations on the filter characteristics was also studied. The results of all these studies are presented in this section.

4.5.1 Variation of Design Parameters

Thickness of Metal Layer

The filters are designed within the inner metallization layers of the PCB as shown in Figure 4.1. The nominal thickness of the metal layer 2, and metal layer 5, in which the filter are realized, is 1.42 mil. The thickness of the metal layer 3 and metal layer 4 is 0.71 mil. These line thicknesses are much greater than the skin depth, which is calculated using the expression $\left(\delta_{deepth} = \sqrt{1/(\pi f \mu\sigma)}\right)$ for different frequencies and displayed in Table 4.4.

Table 4. 4 Skin depth for copper strip at different frequencies

f (GHz)	0.5	1.0	1.5	2.0	**2.4**	3.0	5.2
Skin depth (mil)	$1.16\cdot10^{-1}$	$8.23\cdot10^{-2}$	$6.72\cdot10^{-2}$	$5.82\cdot10^{-2}$	**$5.31\cdot10^{-2}$**	$4.75\cdot10^{-2}$	$3.61\cdot10^{-2}$
Mini. line thickness (mil)	$5.82\cdot10^{-1}$	$4.12\cdot10^{-1}$	$3.36\cdot10^{-1}$	$2.91\cdot10^{-1}$	**$2.26\cdot10^{-1}$**	$2.38\cdot10^{-1}$	$1.80\cdot10^{-1}$

Generally, the line thickness tends to decrease after being fabricated. A series of numerical experiments with different line thickness values was performed in order to predict the impact of the technology tolerances. These experiments were taking over a 2.4 GHz bandpass filter, whose design as well as simulation results, performed with nominal values, have already been presented in the previous section. During the experiments, the line thickness was varied in about ±20 % from the nominal value, while the other parameters were kept constant.

Table 4. 5 Effects of line thickness variation on electrical performances

Variation	-20 %	-15 %	-10 %	-5 %	0 %	5 %	10 %	15 %	20 %
Value (mil)	1.14	1.21	1.28	1.35	1.42	1.49	1.56	1.63	1.70
f_0 (GHz)	2.40	2.40	2.40	2.40	2.40	2.40	2.40	2.40	2.40
IL (dB)	-1.16	-1.17	-1.18	-1.19	-1.20	-1.21	-1.22	-1.23	-1.24
RL (dB)	-12.58	-12.46	-12.36	-12.25	-12.15	-12.05	-11.95	-11.86	-11.76
BW (MHz)	325	325	325	325	325	325	325	325	325

The effects of these variations are shown in Table 4.5. As can be seen, the increasing and decreasing of line thicknesses do not affect the filter bandwidth and center frequency. But, their increase decreases the IL values and increases at the same time the RL ones. A ±20 % variation in line thickness leads to up to ±3.6 % variation in terms of IL and up to 3.5% variation in terms of RL. This effect is due to the conductor losses and is insignificant, because the design thickness is much greater than 5 times the skin depth.

Conductivity of Metal Layer

The effects of the line conductivity variations on filter characteristics were also investigated. The copper line conductivity (σ_{cu}) was varied by ±20 % around its nominal value of $5.8\cdot10^{7}$ S/m. The effects of these variations are summarized in Table 4.6. As can be seen, the increase and decrease of line conductivity do not affect the filter bandwidth and center frequency. But, higher copper conductivity increases the filter insertion loss. A ±20 % variation of conductivity leads to a change of maximum ±5.8 % in terms of IL. This effect is also negligible.

Table 4. 6 Effects of copper conductivity variation on filter electrical performances

σ_{cu} Variation	-20 %	-15 %	-10 %	-5 %	0 %	5 %	10 %	15 %	20 %
Value (10^7 S/m)	4.64	4.93	5.22	5.51	5.8	6.09	6.38	6.67	6.96
f_0 (GHz)	2.40	2.40	2.40	2.40	2.40	2.40	2.40	2.40	2.40
IL (dB)	-1.27	-1.25	-1.23	-1.21	-1.20	-1.18	-1.17	-1.16	-1.16
RL (dB)	-12.17	-12.17	-12.16	-12.27	-12.15	-12.26	-12.25	-12.25	-12.17
BW (MHz)	325	325	325	325	325	325	325	325	325

Thickness of Prepreg Layer

EM simulations with different prepreg thickness were performed in order to predict the impact of the thickness tolerances on filter characteristics. The results of this experiment are summarized in Table 4.7 in terms of center frequency, insertion loss, return loss, and bandwidth.

Table 4. 7 Effects of the prepreg thickness variation on filter electrical performances

Deviation	-20 %	-15 %	-10 %	-5 %	0 %	5 %	10 %	15 %	20 %
Value (mil)	9.60	10.20	10.80	11.4	12.00	12.60	13.20	13.80	14.40
f_0 (GHz)	2.40	2.40	2.40	2.40	2.40	2.40	2.40	2.40	2.40
IL (dB)	-1.55	-1.44	-1.34	-1.27	-1.20	-1.16	-1.12	-1.10	-1.10
RL (dB)	-8.25	-9.07	-9.97	-10.99	-12.15	-13.48	-15.04	-16.92	-19.23
BW (MHz)	375	360	350	335	325	310	285	275	265

As can be seen, the decrease of the prepreg thickness in general deteriorates the filter performances: the BW becomes wider, the IL decreases and the RL increases; whereas the increase of the prepreg thickness improves the performances: the BW becomes narrower, the IL increases, and the RL decreases.

A 20 % decrease of the prepreg thickness leads to a 29 % decrease in the IL, a 32 % decrease in the RL, and a 15 % increase in the BW; whereas a 20 % increase leads to 18 % decrease in the BW, a 8.4 % increase in IL, and a 58.3 % decrease in the RL. The increase and decrease do not affect the center frequency.

Dielectric Constant of Prepreg Layer

EM simulations with different values of the prepreg dielectric constant were performed in order to predict the impact of these tolerances on filter characteristics. The results of these experiments are shown in Table 4.8.

Table 4. 8 Effects of prepreg dielectric constant variation on filter electrical performances

Deviation	-20 %	-15 %	-10 %	-5 %	0 %	5 %	10 %	15 %	20 %
Value	2.83	3.01	3.19	3.36	3.54	3.72	3.89	4.07	4.25
f_0 (GHz)	2.500	2.475	2.450	2.425	2.400	2.400	2.375	2.350	2.325
IL (dB)	-1.06	-1.07	-1.11	-1.15	-1.20	-1.27	-1.34	-1.43	-1.51
RL (dB)	-20.12	-17.01	-14.88	-13.40	-12.15	-11.12	-10.19	-9.40	-8.75
BW (MHz)	300	300	300	310	325	325	325	350	325

As can be seen, a 20 % decrease in the prepreg dielectric constant leads to an increase of about 4.2% and of about 11.7 % in terms of f_0 and IL, respectively, while at the same time the RL decreases in about 65.6 %. Similarly, a 20 % increase of the prepreg ε_r leads to a decrease of about 3.1 % and about 25.8 % in terms of f_0 and IL, respectively, while at the same time the RL increases in about 28.0 %.

Thickness of Core Dielectric Layer

The thickness of the inner core dielectric layer is 2 mils and relatively small. This is less sensitive and therefore, no sensitivity analysis was performed. The thickness of the outer core layers is 10 mils. During the manufacturing, there could be tolerances in terms of this core thickness. A series of numerical experiments with different core thicknesses were performed in order to predict the impact of tolerances on filter performances. The results of these experiments are shown in Table 4.9 in terms of f_0, IL, RL and BW.

Table 4. 9 Effects of core dielectric layer thickness variation on filter performances

$H_{RO4350B}$ Deviation	-20 %	-15 %	-10 %	-5 %	0 %	5 %	10 %	15 %	20 %
Value (mil)	8.00	8.50	9.00	9.50	10.00	10.50	11.00	11.50	12.00
f_0 (GHz)	2.400	2.400	2.400	2.400	2.400	2.400	2.400	2.400	2.400
IL (dB)	-1.21	-1.20	-1.19	-1.19	-1.20	-1.22	-1.23	-1.25	-1.26
RL (dB)	-16.69	-14.99	-13.78	-12.88	-12.15	-11.55	-11.05	-10.62	-10.25
BW (MHz)	270	275	300	325	325	335	350	350	350

As can be seen, the decrease and increase in core thickness do not affect the center frequency. But a 20 % decrease in core thickness leads to a decrease of about 37.4 % in RL, and of about 16.92 % in BW. On the other hand, a 20 % increase in core thickness leads to an increase of about 15.6 % in RL and of about 7.7 % in BW. The insertion loss (IL) is less sensitive against the decrease in core thickness, but sensitive against the increase in core layer thickness.

Dielectric Constant of Core Layer

The core dielectric constant (ε_r) of RO4350B was varied in 20 % around the nominal value, and the effects of these variations on filter performances were investigated. The results of this study are shown in Table 4.10.

Table 4. 10 Effects of the core dielectric constant variation on filter electrical performances

Deviation	-20 %	-15 %	-10 %	-5 %	0 %	5 %	10 %	15 %	20 %
Value	2.78	2.96	3.12	3.31	3.48	3.65	3.83	4.00	4.18
f_0 (GHz)	2.600	2.525	2.500	2.450	2.400	2.375	2.350	2.300	2.275
IL (dB)	-1.40	-1.33	-1.29	-1.24	-1.20	-1.19	-1.16	-1.16	-1.16
RL (dB)	-9.12	-9.90	-10.45	-11.26	-12.15	-12.84	-14.01	-14.58	-15.72
BW (MHz)	400	370	350	335	325	300	285	275	250

As can be seen, a 20 % decrease in the prepreg dielectric constant (ε_r) leads to an increase of about 8.4 % in f_0, and of about 24.9 % in RL, and of about 23.1 % in BW, while as the same time, this leads to a decrease of about 16.7 % in IL. On the other hand, a 20 % increase in the prepreg dielectric constant leads to a decrease of about 5.2 % in f_0, and of about 29.4 % in RL, and of about 23.1 % in BW, while at the same time this increase of the prepreg dielectric constant leads to an increase of about 3.3 % in IL.

Another important design parameter in PCB construction is the dissipation factor. Substrates with lower $\tan\delta$ are desired in designing RF/microwave filters. Although very good high frequency materials combination was chosen in this filter design implementation, their $\tan\delta$ values can also be varied due to the fluctuations in the technology processes.

4.5.2 Impact of Tolerances on Filter Characteristics

Impact of Parameter Variations on Center Frequency

The studies showed that the metal layer conductivity and thickness, as well as the core and prepreg layers thickness, as defined in this work, did not influence the filter center frequency.

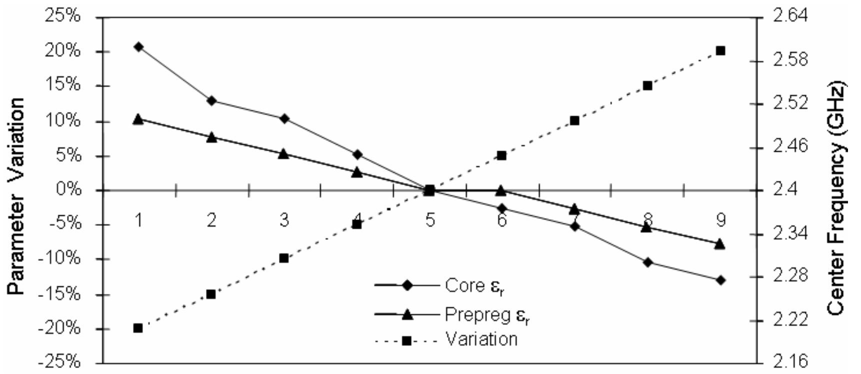

Figure 4. 25 Single parameter sensitivity analysis on filter center frequency

However, the core and prepreg dielectric constants (ε_r) made an impact on the filter center frequency. This impact is shown in Figure 4.25. As can be seen from these plots, the changes in center frequency do not increase or decrease by more than approximately 8 %.

Impact of Parameter Variations on Insertion Loss

The filter insertion loss is less affected by the metal thickness as well as metal conductivity variation. However, the variation of core thickness and dielectric constant as well as prepreg thickness and dielectric constant has a considerable effect on the filter insertion loss. This impact is shown in Figure 4.26.

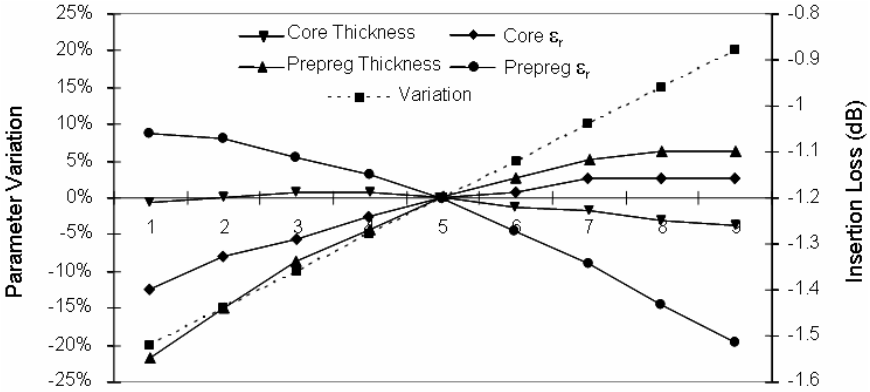

Figure 4. 26 Single parameter sensitivity analysis on filter insertion loss

As can be seen from this figure, the IL is most sensitive to variations in the prepreg thickness and dielectric constant. A ±20 % tolerance leads to IL variation of approximately 29 %.

Impact of Parameter Variations on Return Loss

The filter insertion loss is not (or less) affected by the variation of the metal thickness and metal conductivity. However, the variation of core thickness and dielectric constant as well as Prepreg thickness and dielectric constant has an important impact on the filter insertion loss. This impact is shown in Figure 4.27.

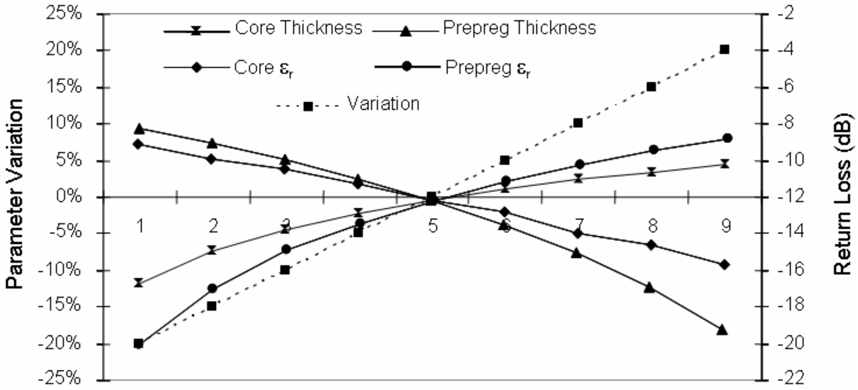

Figure 4. 27 Single parameter sensitivity analyses on filter return loss

As can be seen from this figure, the RL is most sensitive to the change in the prepreg thickness as well as in the dielectric constant. A ±20 % tolerance in the prepreg dielectric constant leads to a variation of approximately 65 % in RL.

Impact of Parameter Variations on Bandwidth

These studies showed that the tolerances in metal thickness as well as metal conductivity did not influence the filter bandwidth. However, the tolerances in core thickness and dielectric constant as well as in prepreg thickness and dielectric constant made an impact on filter bandwidth. These effects are shown in Figure 4.28.

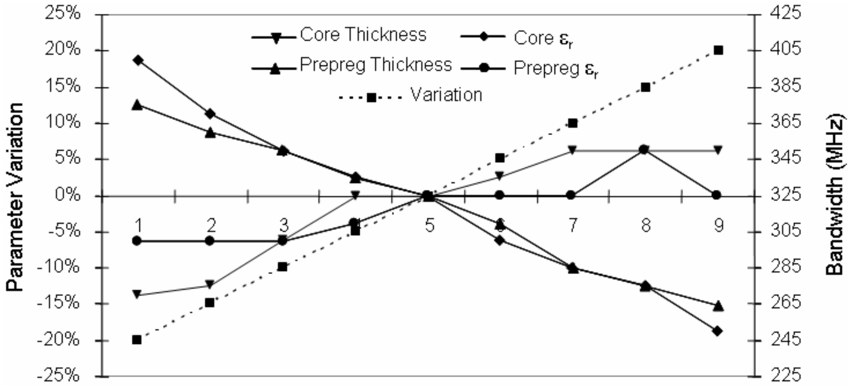

Figure 4. 28 Single parameter sensitivity analysis on filter bandwidth

As can be seen from these diagrams, the variations in core thickness and in prepreg dielectric constant have the same tendency, and on the other hand, the variations in prepreg thickness and core dielectric constant have the same tendency. The BW is most sensitive to the tolerances in prepreg thickness and core dielectric constant. A variation of ±20 % in core ε_r leads to a change in BW of approximately 23 %.

4.5.3 Impact of Topologies/Configurations on Filter Characteristics

The most commonly used approach to improve the filter selectivity is the increase of the number of poles, but at the expense of insertion loss and filter size.

Obviously, the design configuration and topology have an impact on the filter characteristics. The effects of the design topologies and configurations are illustrated in this section.

Example of a 2.4 GHz BPF designed with Tap/Gap –Topologies in Vertical Configurations

Based on the developed methodology, a 2.4 GHz bandpass filter was designed to meet the center frequency (f_0) of 2.4 GHz, the 1-dB-bandwith of 100 MHz, the passband ripples of 0.1 dB, the passband return loss of -20 dB, and the source/load impedance of 50 Ω.

The so-specified filter was implemented with tap as well as gap topologies in two different configurations: "vertical configuration with off-set between the resonant elements" and "vertical configuration without off-set between the resonant elements".

Let us call the filter designed with "tap topology" in "vertical configuration with off-set" filter C1 (see Figure 4.29.a), and the filter implemented with "tap topology" in "vertical configuration without off-set between the resonant elements" filter C2 (see Figure 4.29.b). Similarly, let us also call the filter implemented with "gap topology" in "vertical configuration with off-set" filter C3 (see Figure 4.29.c), and the filter implemented with "gap topology" in "vertical configuration without off-set between the resonant elements” filter C4 (see Figure 4.29.d). The layouts of these design approaches are presented in Figure 4.29.

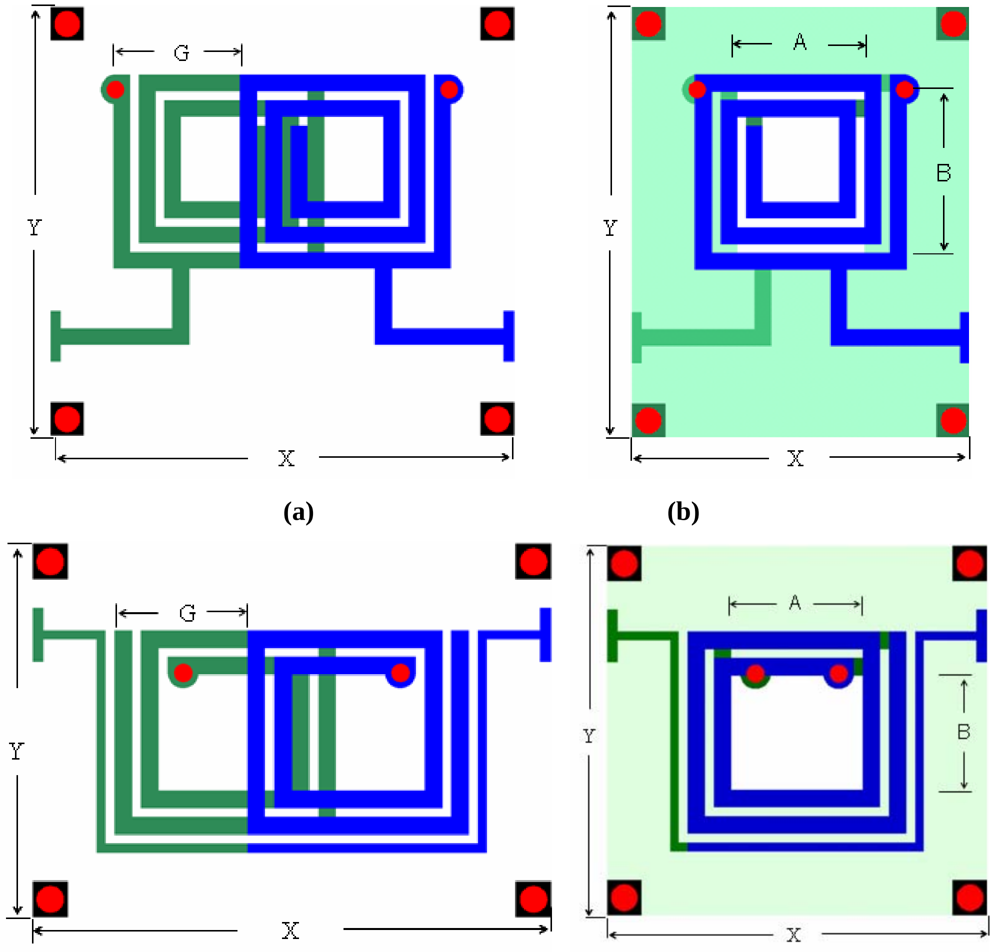

(a) (b)

(c) (d)

Figure 4. 29 Layout views of a 2.4-GHz bandpass filter designed using different topologies and configurations a) filter C1, b) filter C2, c) filter C3, and d) filter C4

Each design consists of two short-terminated inductors, which are capacitively coupled and arranged in vertical configuration. The first inductor was realized on the second metallization layer (ML2), while the second inductor was realized on the fifth metallization layer (ML5).

The tap-line in filter C1 and filter C2 was 94 mil long, and located at 109 mil from the short-ended inductor terminal. The total length of each inductor was 740 mil. The size (in XY-directions) of filter C1 was 220 x 203 mil^2. The off-set (G) between the resonant elements was 60 mil. The size (in XY-directions) of filter C2 was 160 x 203 mil^2 and the size of the EM windows (in AB-directions) was 60 x 76 mil^2.

The input/output-port gap in filter C3 and filter C4 were 4 mil spaced from the resonant inductors. The total length of each inductor was 608 mil. The off-set (G) between the resonant elements in filter C3 was 60 mil, and the size (in AB-directions) of EM windows in filter C4 was 76 x 68 mil^2.

The simulation results of these four different design implementations approaches are shown in Figure 4.30.

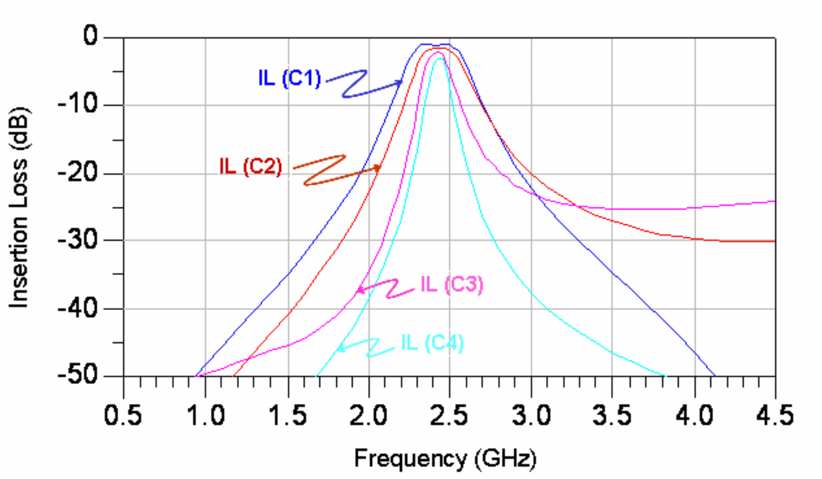

Figure 4. 30 Simulation responses of a 2.4 GHz BPF designed with different topologies and configurations

As can be seen in this figure, the design topologies and configurations affect the filter selectivity. Filter C4 exhibits the best selectivity in comparison to the other filters, but at the expense of the sensitivity.

As can be seen from these diagrams, filter C1 exhibits an insertion loss of 1.15 dB at the midband frequency of 2.4 GHz, and a 3-dB-bandwidth of 300 MHz. Filter C2 shows an insertion loss of 1.54 dB, and a 3-dB-bandwidth of 230 MHz.

Filter C3 exhibits an insertion loss of -2.25 dB at the midband frequency of 2.4 GHz, and a 3-dB-bandwidth of 85 MHz. Filter C4 presents an insertion loss of -3.0 dB at the midband frequency of 2.4 GHz.

Example of a 5.2 GHz BPF designed with Gap/Tap –Topologies in Lateral and Vertical Configurations

Based on the developed methodology, a 5.2 GHz bandpass filter was designed in different topologies and configurations to meet the bandwidth of 200 MHz, the passband ripple of 0.1 dB, and stopband attenuation of at least 20 dB. Four different design approaches have been realized:

The first filter was designed with “gap topology” in “lateral configuration” that we call filter F (see Figure 4.31.a): This design consists of two open terminated inductors, which are capacitively coupled and arranged in lateral configuration. Both the inductors were realized on the second metallization layer (ML2). The length of each inductor was 484 mils, the I/O-port gap was 4 mil spaced from the resonant inductor, the gap (G) between the lateral coupled inductors was 8 mil, and the total size (in XY-directions) of the filter was 256 x 168mil^2.

The second filter was designed with inter-digital “gap topology” in “vertical configuration without off-set between the resonant elements”; let us call this design filter H (see Figure 4.31.b). It consists of two short-terminated inductors, which are capacitively coupled and arranged in vertical configuration without off-set between them. The first inductor was realized on the metal layer 2 (ML2), while the second inductor was realized on the metal layer 5 (ML5). The total length of each inductor was 280 mil. The input/output-port was realized with an interdigital fingers gap spaced by 4 mil. The EM windows size was 88 x 64 mil^2 and the total size of the filter was 124 x 131 mil^2.

The third filter was designed with “gap topology” in “vertical configuration without off-set between the resonant elements”; let us call this design filter I. It consists of two short-terminated inductors. The first inductor was realized on ML2, while the second inductor was realized on ML5. The length of each inductor was 302 mil. The I/O-port gap was spaced by 4 mil from the resonant inductor. The EM window size was 72 x 68mil^2 and the total size of this filter was 144 x 147 mil^2.

The fourth filter was designed with “tap topology” in “vertical configuration without off-set between the resonant elements” that we call filter J. This design consists of two short-terminated inductors. The first inductor was realized on ML2, while the second inductor was realized on ML5. The tap-line was 123 mil long and it was located at 109 mil from the short-ended inductor terminal. The length of each inductor was 433 mil. The size of the EM windows was 48 x 64 mil^2, and the final size of this filter was 136 x 128 mil^2.

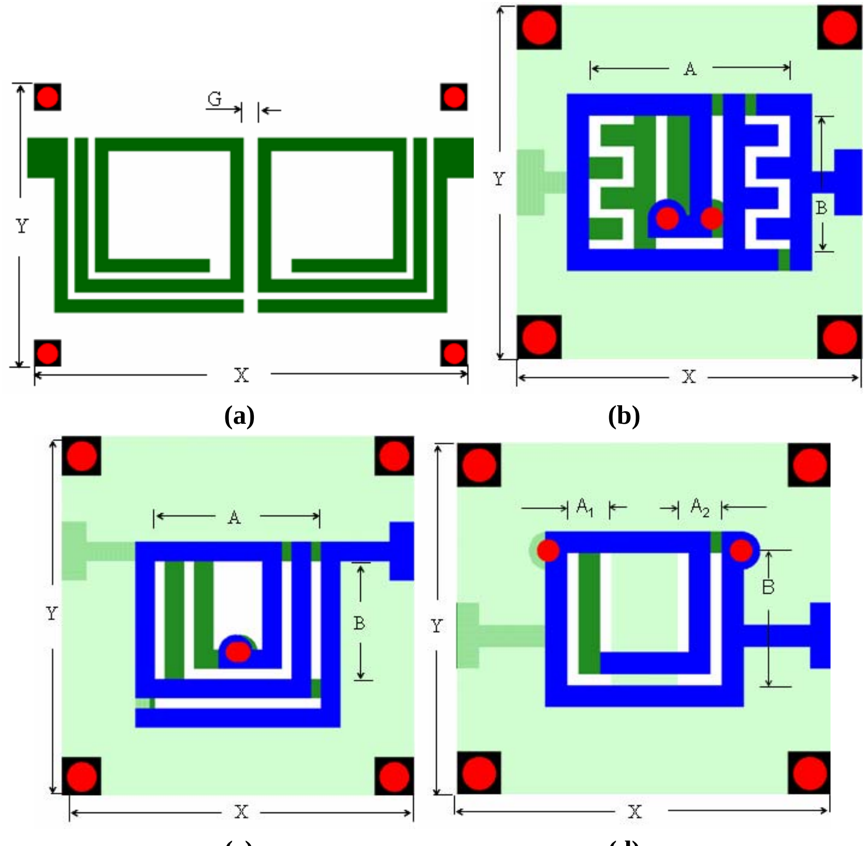

(a) **(b)**

(c) **(d)**

Figure 4. 31 Layout views of a 5.2 GHz bandpass filter designed using different topologies and configurations a) filter F, b) filter H, c) filter I, and d) filter J

These different layouts are shown in Figure 4.31, and their simulation results are shown in Figure 4.32 in terms of insertion loss.

As can be seen from these diagrams, filter F exhibits an insertion loss of 2.4 dB at the midband frequency of 5.2 GHz. Filter H exhibits an insertion loss of 2.4 dB at the midband frequency of 5.2 GHz. Its 3-dB-bandwidth is 130 MHz.

Filter I presents an insertion loss of 1.8 dB at the midband frequency of 5.2 GHz. Its bandwidth is 270 MHz. Filter J exhibits an IL of 1.8 dB at the midband frequency of 5.2 GHz. Its 3-dB-bandwidth is 240 MHz.

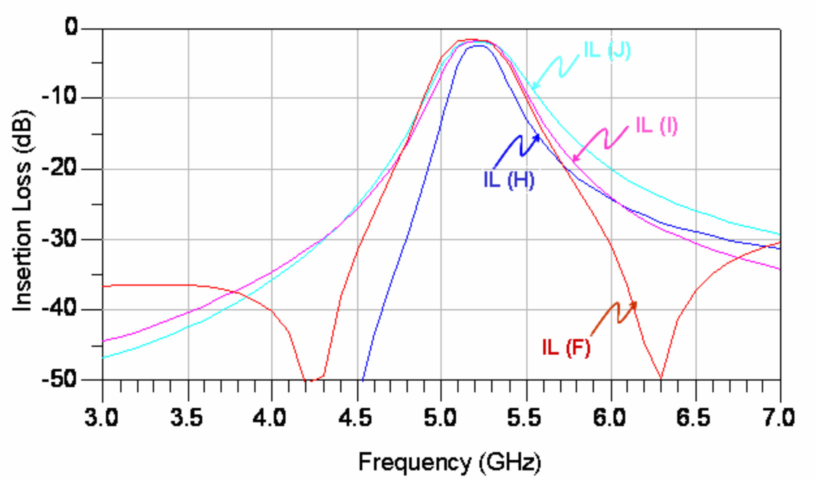

Figure 4. 32 Simulated responses of a 5.2 GHz BPF designed with different topologies and configurations

As can be seen, the design topologies and configurations affect the filter selectivity. “Gap topology” with interdigital fingers provides the best selectivity in comparison to the simple “gap topology” as well as to the “tap topology”. However, the sensitivity of the filter is slightly affected.

4.6. Design Downscaling

One of the main objectives of this work is the filter design miniaturization. In principal, the miniaturization of a component depends on many different factors such as the given design specifications, the design rules of the component, the choice of the technology, etc.

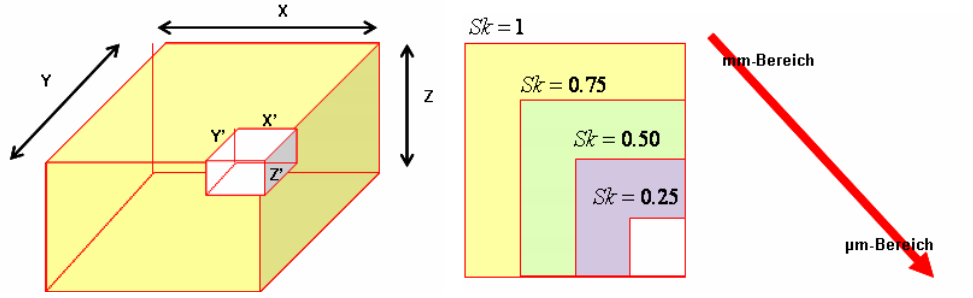

(a) (b)

Figure 4. 33 Sketch for the downscaling of a component

In order to shrink the size of a component, from mm-range to µm-range for example, the following procedure was used:

- Fragmentation of the component into its subcomponents.
- Description of each subcomponent and establishment of a relationship between its geometrical parameters and electrical parameters.

- Shrinking of the size of each subcomponent by a scaling factor Sk, with $0 < Sk < 1$, and consideration of its characteristics.
- Downscaling of the complete component by assembling all the scaled subcomponents, and consideration of its characteristics. The size of the final component passes from (X, Y, Z) into (X', Y', Z').

For the illustration of this approach, a spiral inductor of size 100 mil x 100 mil was considered as a filter subcomponent and was designed to meet the resonant frequency f_{res} of 2.24 GHz. This inductor was embedded in a dielectric medium of height H = 53 mil. Its line-width (W), line-space (S) line-with-line-space-ratio (W/S), line-thickness (T), inner-dimension (D_i) and total-length (l) were W = 8 mil, S = 4 mil, W/S = 2, T = 1.42 mil, D_i = 32 mil, and l = 784 mil, respectively. This inductor design was electromagnetically simulated and the simulation results, given in terms of effective inductance L_e, magnitude of the input impedance $Mag(Z_{in})$, bandwidth (BW), and loaded quality factor Q_l, are 10.29 nH, 10.05 kΩ, 0.03 GHz, and 74, respectively.

The size of this inductor was shrunken successively by a factor Sk equaling 0.75, 0.50, and 0.25, respectively, while keeping the resonant frequency f_{res} constant to 2.24 GHz (by compensating the overall length of the inductor and the line width). The downscaled designs were simulated and their simulation results are summarized in Figure 4.34.

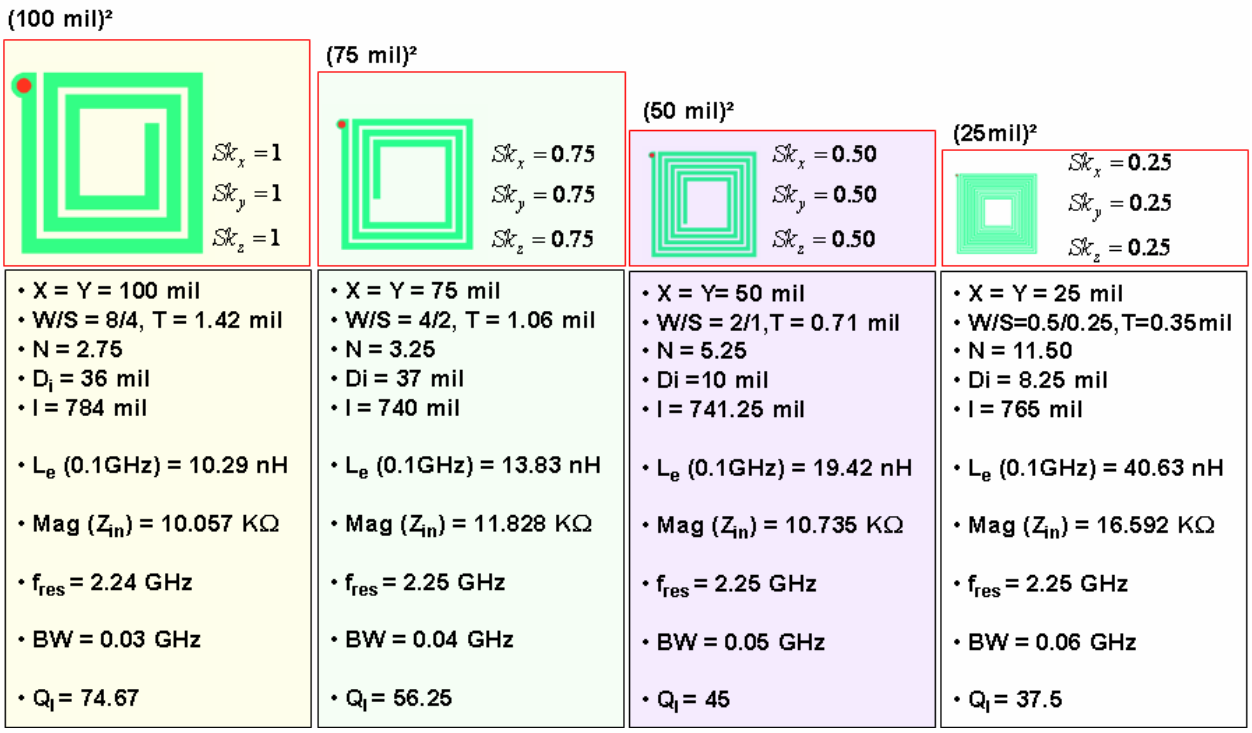

• X = Y = 100 mil • W/S = 8/4, T = 1.42 mil • N = 2.75 • D_i = 36 mil • l = 784 mil	• X = Y = 75 mil • W/S = 4/2, T = 1.06 mil • N = 3.25 • Di = 37 mil • l = 740 mil	• X = Y= 50 mil • W/S = 2/1,T = 0.71 mil • N = 5.25 • Di =10 mil • l = 741.25 mil	• X = Y = 25 mil • W/S=0.5/0.25,T=0.35mil • N = 11.50 • Di = 8.25 mil • l = 765 mil
• L_e (0.1GHz) = 10.29 nH	• L_e (0.1GHz) = 13.83 nH	• L_e (0.1GHz) = 19.42 nH	• L_e (0.1GHz) = 40.63 nH
• Mag (Z_{in}) = 10.057 KΩ	• Mag (Z_{in}) = 11.828 KΩ	• Mag (Z_{in}) = 10.735 KΩ	• Mag (Z_{in}) = 16.592 KΩ
• f_{res} = 2.24 GHz	• f_{res} = 2.25 GHz	• f_{res} = 2.25 GHz	• f_{res} = 2.25 GHz
• BW = 0.03 GHz	• BW = 0.04 GHz	• BW = 0.05 GHz	• BW = 0.06 GHz
• Q_l = 74.67	• Q_l = 56.25	• Q_l = 45	• Q_l = 37.5

Figure 4. 34 Survey of EM simulation results of an inductor design, the size of which was successively downscaled while keeping its resonant frequency constant (by compensating the overall length of the inductor and the line width)

As can be seen in this figure, the shrinking of the inductor size leads to the decrease of Q_l and to the increase of L_e at the same time.

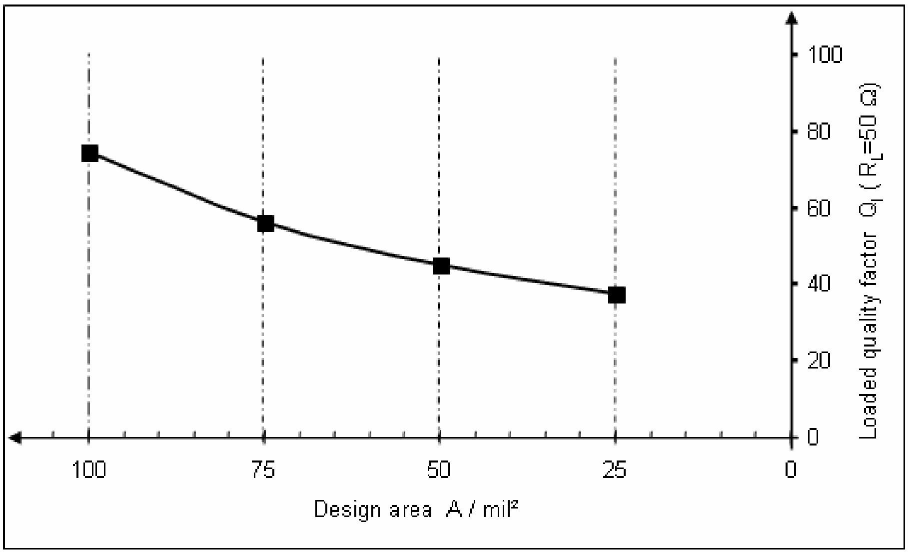

Figure 4. 35 Loaded quality factor Q_l versus design area A

Figure 4.35 shows the inductor's loaded quality factor versus the design area. The decrease of Q_l is due to the increase of the conductor losses, because narrower line-width (W) leads to smaller line cross-sectional area, and this increases the Ohmic losses. The total conductor losses are not only due to the Ohmic losses, but they are also due to the skin-effect losses.

The increase of L_e is due to the increase of the magnetic field that is proportional to the number of turns (N) and inversely proportional to the line radius. The number of turns has increased and the line radius has decreased at the same time.

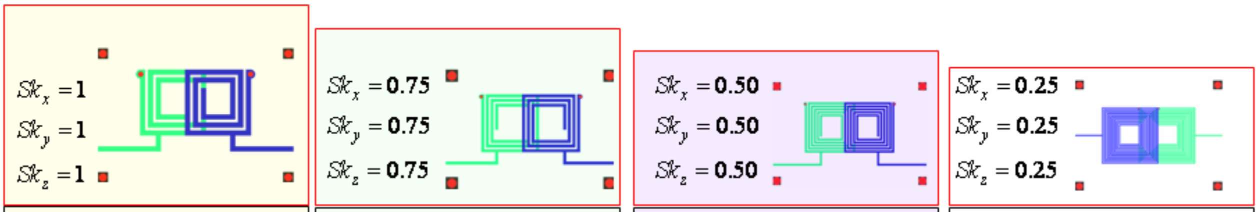

- X = Y = 100 mil
- W/S = 8/4, T = 1.42 mil
- N = 2.75
- D_i = 36 mil
- l = 784 mil

- G = 68 mil
- X_T = 296 mil
- Y_T = 203 mil
- H_T = 53 mil

- f_0 = 2.25 GHz

- IL (2.25GHz) = 1.5 dB
- RL (2.25GHz) = 34.0 dB

- X = Y = 75 mil
- W/S = 4/2, T = 1.065 mil
- N = 3.25
- D_i = 37 mil
- l = 740 mil

- G = 53 mil
- X_T = 220 mil
- Y_T = 155 mil
- H_T = 33 mil

- f_0 = 2.25 GHz

- IL (2.25GHz) = 2.8 dB
- RL (2.25GHz) = 22.6 dB

- X = Y = 50 mil
- W/S = 2/1, T = 0.71 mil
- N = 6.75
- D_i = 10 mil
- l = 832 mil

- G = 39 mil
- X_T = 153 mil
- Y_T = 102 mil
- H_T = 26.5 mil

- f_0 = 2.28 GHz

- IL (2.28GHz) = 6.4 dB
- RL (2.28GHz) = 20.2 dB

- X = Y = 25 mil
- W/S=0.5/0.25 T=0.35mil
- N = 11.50
- D_i = 8.25 mil
- l = 765 mil

- G = 16.25 mil
- X_T = 65.25 mil
- Y_T = 49 mil
- H_T = 13.25 mil

- f_0 = 2.27 GHz

- IL (2.27GHz) = 6.4 dB
- RL (2.27GHz) = 16.7 dB

Figure 4. 36 EM analysis of a bandpass filter, the size of which was successively downscaled while keeping its center frequency constant (by compensating the overall length of the inductor and the line width)

The complete filter component, which consists of coupled inductors, was downscaled while keeping the filter center frequency f_0 constant and equal to 2.25 GHz. Each design was simulated and the simulation results are summarized in Figure 4.36 in terms of electrical parameters (such as the insertion loss IL, the return loss RL, and the center frequency f_0) as well as geometrical parameters (like the off-set between the filter elements G, and the filter size X_T, Y_T, H_T).

As can be seen, the shrinking of the filter size while keeping its center frequency (f_0) constant leads to a degradation of the filter characteristics in terms of insertion loss (IL) and return loss (RL). Thus, the downscaling of the filter design up to the scaling factor Sk = 0.75 leads to acceptable filter characteristics, but beyond this scaling factors, the filter sensitivity becomes poor. The degradation of the filter sensitivity is mainly due to the increase of the conductor losses, as explained previously.

4.7. Summary

Based on this design methodology, bandpass filters for various applications were developed and implemented in organic based MCM-L technology.

After describing the different sources of losses in microstrip filters, design measures were undertaken to reduce these losses. Bandpass filters for different applications such as Wi-Fi and Wi-MAX were designed with different topologies (tap, and gap) and configurations (lateral, vertical with off-set, and vertical without off-set between the resonant elements). The focus was particularly in the design miniaturization and performance improvement.

Sensitivity analyses for design parameters were performed in order to predict the impact of the tolerances due to the manufacturing process fluctuations on the filter performances. As could be seen, the bandwidth was most sensitive against the tolerances in prepreg thickness as well as in core dielectric constant. The insertion loss and return loss were most sensitive against the tolerances in substrate thickness as well as in substrate dielectric constant. The center frequency was more sensitive against the tolerances in substrate dielectric constant.

It was also shown that the filter design topologies and configurations made an impact on the filter characteristics. “Lateral configuration” showed not only a very good sensitivity, but also transmissions zeros in filter characteristics, however at the expense of the size. “Gap topology” improved the filter selectivity, but at the cost of the sensitivity.

“Vertical configuration with off-set between the resonant elements” showed a very good electrical performance, particularly in terms of insertion loss. “Vertical configuration without off-set between the resonant elements” exhibited the best design compactness, but with good electrical characteristics only within the passband.

It has also shown that the downscaling of the filter size while keeping the center frequency constant degrades the filter sensitivity, because the conductor losses increase mainly due to the decrease of the cross-sectional line area.

The analysis of all these designs was performed using the Method-of-Moments codes, “Agilent Momentum”. This full-wave solver has the advantage of analysis-speed and it required rather low computation efforts.

Chapter 5

Experimental Validation

Experimental measurements are not only the way to characterize the manufactured prototypes, but also the way to validate the design methodology as well as to verify the modeling accuracy. This chapter presents the measurements and characterization of RF/microwave filters realized based on the design methodology developed in this work.

The basic equipment used for the measurement of these filters will be presented first, followed by the description of the common measurement errors related to the measurement equipment. In the second section, the technique used to eliminate these errors before performing the measurements is described. The third section presents the measurement and analysis methods. The fourth section presents the de-embedding method as well as the measured and simulated results in comparison. Finally, the last section summarizes the whole chapter.

High-density-interconnect printed-circuit-boards (HDI-PCB), which include many filters and de-embedding structures, were fabricated using six-metal-layer organic MCM-L technology.

5.1. Measurement Equipment and Related Errors

The basic equipment for the measurement of the integrated RF/microwave filters consists of a vector network analyzer (VNA), RF cables and connectors, RF probes, as well as a personal computer and software (e.g. “WinCal”). Some of these elements are described in the following.

5.1.1 Measurement Equipment

Vector Network Analyzer (VNA)

The VNA “HP8510B”, which consists of a control and display unit (mainframe), a wobbled high frequency generator (RF synthesizer), and an S-parameter test-set that detects the transmitted and reflected power at the both ports of the device under test (DUT), was used for the measurement of the complex transmitted and reflected power at the different ports.

A simplified block diagram of this VNA is shown in Figure 5.1.b. The RF source generates the incident signal that is downconverted to an intermediate frequency (IF), which is detected after the switch by a receiver, and stored as reference signal. The signals transmitted through the DUT as well as the signals reflected from the DUT ports are detected and stored through the couplers. Then, the S-parameters relating to the current port are calculated from the three stored signals (reference, transmitted, and reflected).

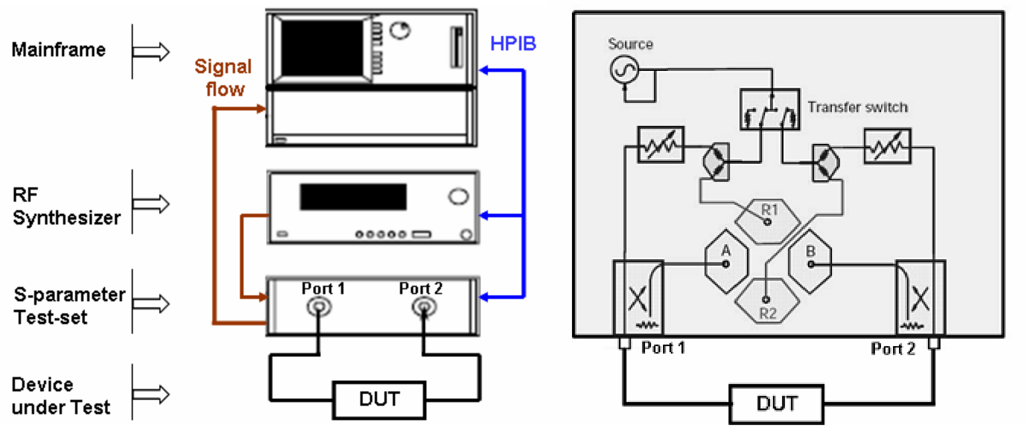

(a) (b)

Figure 5. 1 a) Vector network analyzer and b) simplified block diagram of a 4-sampler VNA

RF Probes, Cables and Connectors

The RF probes, cables and connectors can be seen as interface between the DUT and the VNA. For the probing of gold pads, the air-coplanar-probes (ACP) with flexible beryllium-copper (BeCu) tips were used in order to keep low the contact resistance.

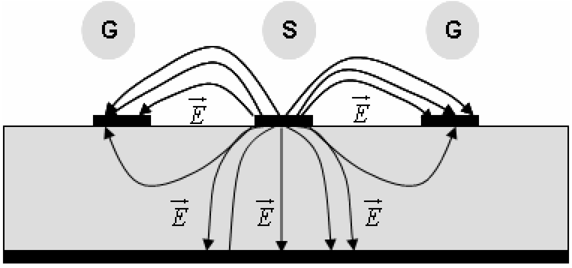

Figure 5. 2 Electric field scattering in a G-S-G coplanar probe configuration

The signal-ground-signal (G-S-G) probes are used for the measurement because these probes have the advantage of tightly controlling electromagnetic (EM) fields around the signal probe [5.1]. The electrical fields around the signal (S) tip terminate on the ground (G) tips while the magnetic fields between S and G cancel. This configuration (see Figure 5.2) ensures a better wave propagation along the line, and it provides accurate measurements. The pitch (distance between the probe pads) was 250 µm.

5.1.2 Errors Related to Measurement Equipment

On and off, there exist errors associated with the measurement equipments. These errors, which are coming mainly from the VNA, RF probes, cables and connectors, can be classified into systematic errors, random errors, and drift errors [5.2].

Systematic errors are those due to imperfections in the VNA, RF probes, cables and connectors. These errors are time invariant, repeatable and therefore predictable. In VNA, their contribution depends on the level of the applied input power. For instance, too high applied input power may move the front-end mixer or IF amplifiers into compression. Too low applied input power may degrade the measuring accuracy. The power of 5 mW was standard setup during the measurement.

The major systematic errors associated with the VNA and RF probes are: directivity errors (E_D), crosstalk errors (E_X), load (E_L) and source (E_S) match errors, and reflection (E_R) and transmission tracking errors (E_T).

Random errors are unpredictable since they vary with time in a random fashion. These errors can not be removed by calibration. The main contributors to random errors are the instrument noise, like source phase noise, sampler noise, etc. By measuring the same parameters several times and taking the average of the obtained results, one can improve the repeatability.

Drift errors are those due to the test-equipment performance changing by-and-by after being calibrated. These kinds of errors are primarily caused by temperature variation, degradation of the electrical contacts or increased electromagnetic interference (EMI) from outside environment. Drift errors can be removed by further calibration.

Thus, in order to obtain reliable, repeatable and accurate measurements, all these errors relating to the test-equipment should be identified and removed. This process, known as calibration, is described in the next section.

5.2. Calibration of Measurement Equipment

Generally, the calibration process begins with the definition of the error-model that describes the measuring set-up, followed by the application of an appropriate algorithm, which can remove the defined error-parameters.

5.2.1 Errors-Model

Errors coming from a two-port measurement system can be modeled using the 12-terms-errors-model as shown in Figure 5.3.

This model accounts for errors introduced by directivity (E_D), crosstalk (E_X), source (E_S) and load (E_L) mismatch, reflection tracking (E_R), and transmission tracking (E_T) for both forward (F) and reverse (R) ports. These 12 parameters are the reason for referring to 12-terms-errors.

From this error-model, neglecting the E_X terms, the mathematical equations relating the S-parameters to the parameters of the device under test (DUT) can be expressed by:

$$S_{11M} = E_{DX} + E_{RF} \frac{S_{11A}(1 - S_{22A}E_{LF}) + S_{12A}S_{21A}E_{LF}}{(1 - S_{11A}E_{SF})(1 - S_{22A}E_{LF}) - S_{12A}S_{21A}E_{LF}E_{SF}} \tag{5.1}$$

$$S_{21M} = \frac{S_{21A}E_{TF}}{(1 - S_{11A}E_{SF})(1 - S_{22A}E_{LF}) - S_{12A}S_{21A}E_{LF}E_{SF}} \tag{5.2}$$

$$S_{22M} = E_{DR} + E_{RR} \frac{S_{22A}(1 - S_{22A}E_{LR}) + S_{21A}S_{12A}E_{LR}}{(1 - S_{22A}E_{SR})(1 - S_{11A}E_{LR}) - S_{12A}S_{21A}E_{LR}E_{SR}} \tag{5.3}$$

$$S_{12M} = \frac{S_{12A}E_{TR}}{(1 - S_{22A}E_{SR})(1 - S_{11A}E_{LR}) - S_{12A}S_{21A}E_{LR}E_{SR}} \tag{5.4}$$

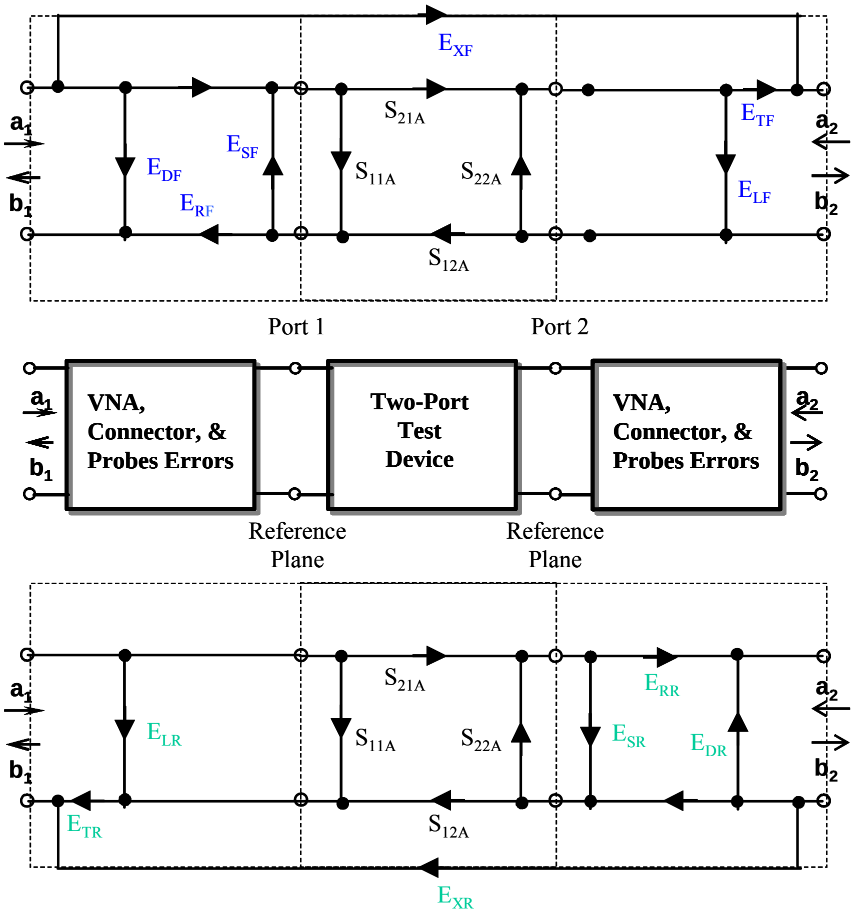

Figure 5. 3 Signal flow graph with 12-term-errors-model representing a two-port measuring setup

Calibration consists in replacing the DUT by well-known calibration-standards like those contained on impedance-standard-substrates (ISS).

5.2.2 Line-Reflect-Reflect-Match (LRRM) Calibration Method

There is various calibration techniques [5.1]-[5.4], which can be used to remove the impact of the different errors presented previously. Examples of these techniques are short-open-load-thru (SOLT), thru-reflect-line (TRL), line-reflect-match (LRM), line-reflect-reflect-match (LRRM), etc. Each of them has advantages as well as disadvantages.

LRRM is the method used in this work to remove the errors related to the test-equipment. This method uses the same set of standards as the short-open-load-thru (SOLT) method, with the only difference that the short and open standards do not need to be defined. This method requires little information about the calibration-standards and is therefore the most usable method. The measurement of short, open and load standards enables the elimination of directivity (E_D), source (E_S) and reflection tracking (E_R) errors, for both forward (F) and reverse (R) ports. The measurement of thru standard enables the elimination of transmission tracking (E_T) and load mismatch (E_L) error for both forward (F) and reverse (R) ports.

Assuming that both the probes (on port 1 and port 2) are enough spaced from each other, the crosstalk (E_X) errors are neglected [5.5]. Therefore, the 12-terms-errors parameters can be removed.

5.3. RF Characterization of Integrated Filters

RF/microwave devices can be characterized by expressing their transmission and reflection characteristics. Using a VNA, incident signals are measured with the R (for reference) channel, reflected signals are measured with the A channel, and transmitted signal are measured with the B channel [5.6]. The transmission and refection characteristics of the DUT can then be quantified by using the amplitude and phase information of theses three signals.

5.3.1 Transmission and Reflection Characteristics of Filters

The transmission characteristics of DUT can be expressed by various parameters such as S-parameters (S_{21}, S_{12}), transmission coefficient(T), insertion loss (IL), group delay (τ_D), etc. Similarly, the reflection characteristics can be expressed by different parameters such as S-parameters (S_{11}, S_{22}), reflection coefficient(Γ), return loss (RL), voltage standing wave ratio (VSWR), impedance $(R+jX)$ and admittance$(G+jB)$parameters, etc. Thus, for the characterization of integrated filters, it suffices to express their IL, RL, and τ_g.

• The insertion loss (IL)expresses the filter sensitivity, and it can be calculated using

$$IL = -10\log_{10}\frac{P_L}{P_{in}} \tag{5.5}$$

where P_{in} and P_L are incident and transmitted power, respectively.

In terms of S-parameters, IL is related to the magnitude of S_{21} (or S_{12}) by

$$IL = -10\log_{10}\left(\frac{1}{\left|S_{21}\right|^2}\right) \tag{5.6}$$

• The return loss (RL) can be calculated using

$$RL = -10\log_{10}\frac{P_R}{P_{in}} = -10\log\left(\left|\Gamma\right|^2\right) \tag{5.7}$$

where P_{in} and P_R are incident and reflected power, respectively.

The return loss is related to the magnitude of S-parameter reflection coefficients ($\left|S_{11}\right|$, or$\left|S_{22}\right|$) by

$$RL = -10\log_{10}\left(\frac{1}{\left|S_{11}\right|^2}\right) \tag{5.8}$$

• The group delay is related to the time a signal is delayed while passing through the filter. It is the derivative of the transmission phase with respect to frequency, and it can be expressed by:

$$\tau_D = \frac{d\phi_T(\omega)}{d\omega} \tag{5.9}$$

where $\phi_T(\omega)$ is the phase transmission, and ω is the angular frequency.

Further parameters useful for the characterization of filters are center frequency$\left(f_0\right)$, bandwidth$\left(BW\right)$, quality factor $\left(Q_L\right)$ and shape factor$\left(SF\right)$.

The center frequency of a bandpass filter is the frequency at which the filter operates. The filter bandwidth is commonly defined at 3-dB, which means that the half of the transmitted signal is present at the passband. The unloaded quality factor of the filter is the inverse of the 3-dB-bandwidth$Q_L = \left(f_0/BW_{3dB}\right)$. The shape factor expresses the filter selectivity, and it is commonly defined as ratio of the 3-dB-bandwidth to the 30-dB-bandwidth$SF = \left(BW_{3dB}\right)/\left(BW_{30dB}\right)$.

Although the device characterization, in this work, is mainly focussed on integrated filters, the structures such as inductors, which were used in designing these filters, can also be evaluated. The characteristics of these inductors are expressed in terms of electrical parameters such as effective inductance$\left(L_e\right)$, resonant frequency$\left(f_{res}\right)$, quality factor, etc. These parameters can be extracted from the S-parameters.

5.3.2 S-Parameter Devices Characterization

The most commonly measured parameters in high frequency device characterizations are the S-parameters. These parameters have many advantages over the other parameters such as Z-, Y-, or H-parameters:

- They relate to familiar filter measurements such as insertion loss, and return loss.

- They do not require connection of undesired load to the DUT, for the characterization.

- From the S-parameters, the other parameters (Z-, Y-, H-, or T,-Parameter) can easily be derived and further electrical parameters such as inductance, capacitance, resistance and conductance can be easy determined.

- S-parameters are defined in terms of voltage travelling waves (a, b), which are relatively easy to measured. And these travelling waves do not vary in magnitude at points along a lossless transmission line.

N-Port Network S-Parameters

An N-port DUT has N^2 S-parameters, so, a two-port DUT has four S-parameters (S_{11}, S_{21}, S_{12}, S_{22}), and a one-port DUT has one S-parameter (S_{11}).

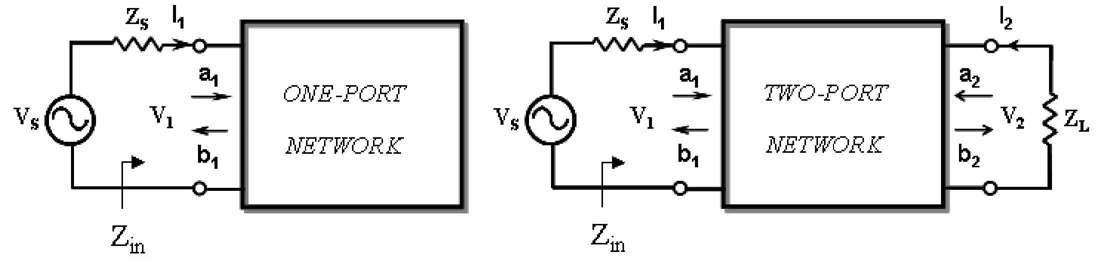

(a) (b)

Figure 5. 4 a) One-port and b) two-port networks device representation

Figure 5.4.b shows a two-port network, symbolizing a filter device. The linear equations describing this network are given in terms of S-parameters coefficients by:

$$b_1 = S_{11}a_1 + S_{12}a_2 \tag{5.10}$$

$$b_2 = S_{21}a_1 + S_{22}a_2 \tag{5.11}$$

where S_{11} and S_{22} are the reflection coefficients seen at port 1 and port 2, when port 2 and port1 are terminated in a matched impedance $Z_0 = 50\ \Omega$, respectively, S_{21} and S_{12} are the transmission coefficients from port 1 to port 2 and from port 2 to port 1, respectively. These parameters are defined as:

$$\mathrm{S}_{11} = \frac{\mathrm{Reflected}}{\mathrm{Incident}} = \left.\frac{\mathrm{b}_1}{\mathrm{a}_1}\right|_{\mathrm{a}_2=0} \tag{5.12}$$

$$\mathrm{S}_{21} = \frac{\mathrm{Transmitted}}{\mathrm{Incident}} = \left.\frac{\mathrm{b}_2}{\mathrm{a}_1}\right|_{\mathrm{a}2=0} \tag{5.13}$$

$$\mathrm{S}_{22} = \frac{\mathrm{Reflected}}{\mathrm{Incident}} = \left.\frac{\mathrm{b}_2}{\mathrm{a}_2}\right|_{\mathrm{a}1=0} \tag{5.14}$$

$$\mathrm{S}_{12} = \frac{\mathrm{Transmitted}}{\mathrm{Incident}} = \left.\frac{\mathrm{b}_1}{\mathrm{a}_2}\right|_{\mathrm{a}_1=0} \tag{5.15}$$

Sometime, the one-port S-parameter is required for the characterization of short-terminated structures (such as resonant inductors) used in designing the bandpass filters. This one-port S-parameter (S_{11}) is related to the device input impedance Z_{in}, and source/load impedance Z_0 by

$$S_{11} = \frac{b_1}{a_1} = \frac{Z_{in} - Z_0}{Z_{in} + Z_0} \tag{5.16}$$

From this relation, the device input impedance (Z_{in}) can be determined as:

$$Z_{in} = Z_0 \frac{(1+S_{11})}{(1-S_{11})} = R + jX \tag{5.17}$$

where the real part (R) expresses the losses and the imaginary part (X) the energy storage in the device.

5.4. Measurement Results

This section deals with the measurement results of the filter components. But before their evaluation, these results are first de-embedded.

5.4.1 De-embedding of Measurement Results

In order to enable the measurement of the integrated filters, probe-pads and interconnecting-lines (also called adapters), which represent the interface between the DUT and probe-tips, are required.

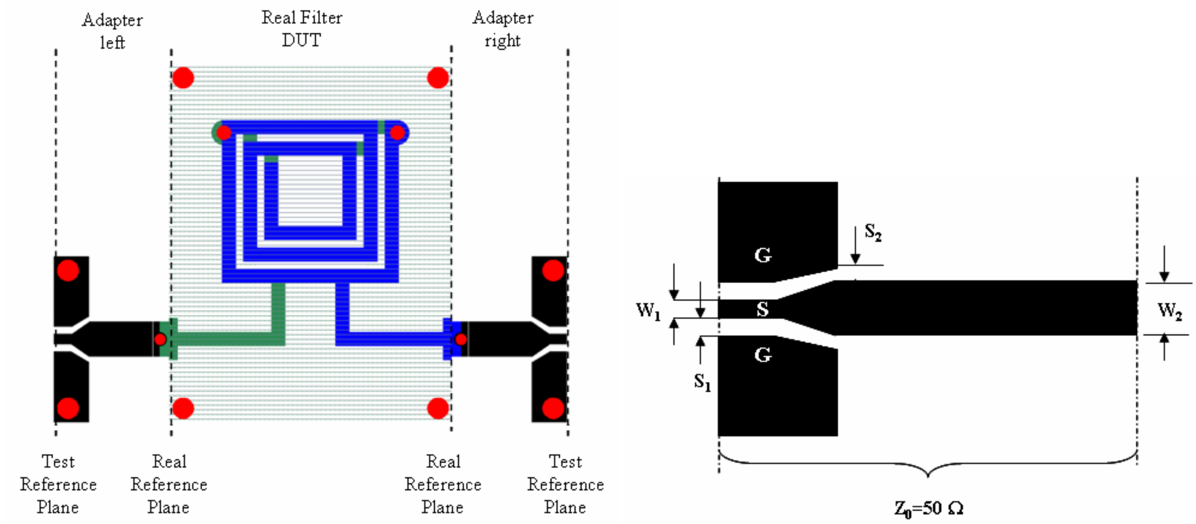

(a) **(b)**

Figure 5. 5 a) Layout of an embedded test-filter and b) design of its left adapter

Figure 5.5 shows the layout of an embedded test-filter, as well as the design of its left adapter for G-S-G-pads probing with 250 µm-pitch (W_1 = 6 mil, S_1 = 4 mil, and W_2= 20mil). This real test-filter is embedded between a left and right adapter. Each adapter was designed to match the 50 ohm-port characteristic impedance.

In practical, these adapters influence the characteristics of the real filter. To obtain the real measuring-results, the influence of these adapters should be removed (de-embedded) from the measuring-results. This process, also called “de-embedding”, is a mathematical procedure of removing the influence of the probe-pads and interconnecting-lines (or adapters) from the measuring results such as to provide the measuring-results of the real device under test.

De-embedding Principle

Although different de-embedding techniques applicable to integrated passive and active components are available (e.g., [5.1], [5.7]-[5.8]), the choice of the appropriate method involves a trade-off between results accuracy and characterization efforts. In this work, “thru-de-embedding method” was used. This method utilizes the two-port circuit modeling of left and right adapters. Assuming that left and right adapters are symmetric, the measured S-parameters of the “THRU” standard can be modeled as a cascade of two two-port networks, wherein each network represents one adapter as symbolized in Figure 5.6.

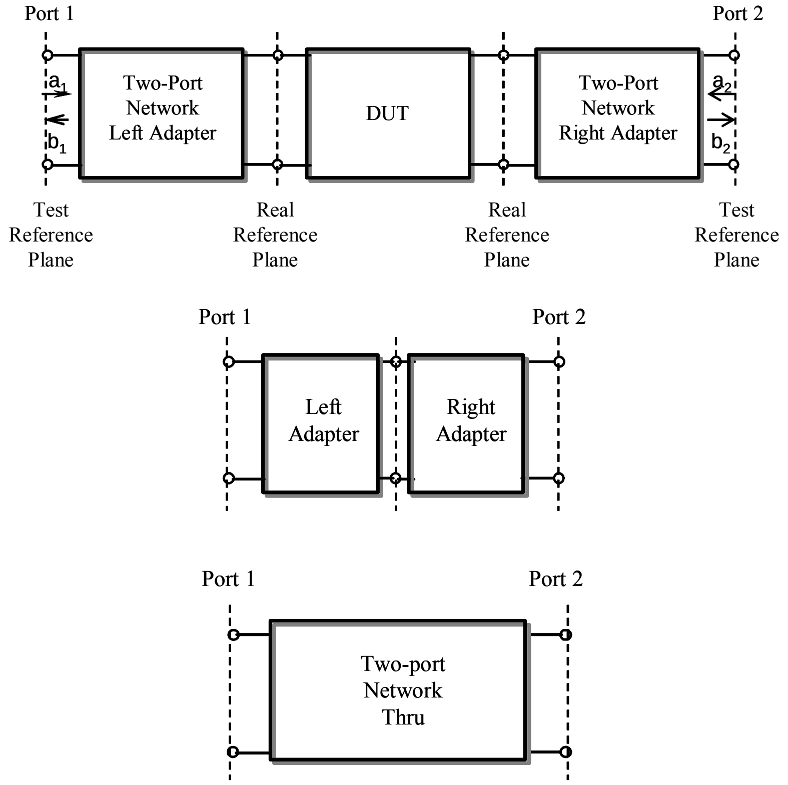

Figure 5. 6 Block diagram for illustration of thru de-embedding method

The fitted S-parameters of left and right adapters $\left(\overline{\overline{\mathbf{S}}}_{\text{left}},\ \overline{\overline{\mathbf{S}}}_{\text{right}}\right)$, as well the measured S-parameters of device $\left(\overline{\overline{\mathbf{S}}}_{\text{total}}\right)$ are transformed into their corresponding T-parameters, since T-parameters are more convenient for operations with cascaded networks. As results, the T-parameters of the real device ($\overline{\overline{\mathbf{T}}}_{\text{DUT}}$) can easily be obtained using:

$$\overline{\overline{\mathbf{T}}}_{\text{DUT}}=\overline{\overline{\mathbf{T}}}_{\text{left}}^{-1}\,\overline{\overline{\mathbf{T}}}_{\text{total}}\,\overline{\overline{\mathbf{T}}}_{\text{right}}^{-1} \tag{5.18}$$

Finally, the S-parameters of the real-device ($\overline{\overline{\mathbf{S}}}_{\text{DUT}}$) are obtained through back-transformation of the T-parameters.

The complete de-embedding procedure is summarized as follows:

- Measuring of the test-sample with probes at the test reference planes, which results to $\left(\overline{\overline{\mathbf{S}}}_{\text{total}}\right)$,
- Measuring of the “THRU” standard, which results to $\left(\overline{\overline{\mathbf{S}}}_{\text{thru}}\right)$,
- Two-port network modeling of the measured “THRU” standard, which results to $\left(\overline{\overline{\mathbf{S}}}_{\text{thru, opt}}\right)$, followed by its modeling as cascading of two two-port networks, which results to $\left(\overline{\overline{\mathbf{S}}}_{\text{left}},\ \text{and}\ \overline{\overline{\mathbf{S}}}_{\text{right}}\right)$,

- Transformation of the resulting S-parameters $\left(\bar{\bar{\mathbf{S}}}_{\mathrm{total}}, \bar{\bar{\mathbf{S}}}_{\mathrm{left}}, \text{ and } \bar{\bar{\mathbf{S}}}_{\mathrm{right}}\right)$ to the corresponding T-parameters $\left(\bar{\bar{\mathbf{T}}}_{\mathrm{total}}, \bar{\bar{\mathbf{T}}}_{\mathrm{left}}, \text{ and } \bar{\bar{\mathbf{T}}}_{\mathrm{right}}\right)$,
- Determination of the T-parameters of the real-device $\left(\bar{\bar{\mathbf{T}}}_{\mathrm{DUT}}\right)$ by applying (5.18), and
- Back transformation of $\bar{\bar{\mathbf{T}}}_{\mathrm{DUT}}$ to $\bar{\bar{\mathbf{S}}}_{\mathrm{DUT}}$.

Effect of De-embedding on Measurement Results

The effect of the de-embedding on the measurement results is illustrated in terms of insertion loss and return loss for filter C1.

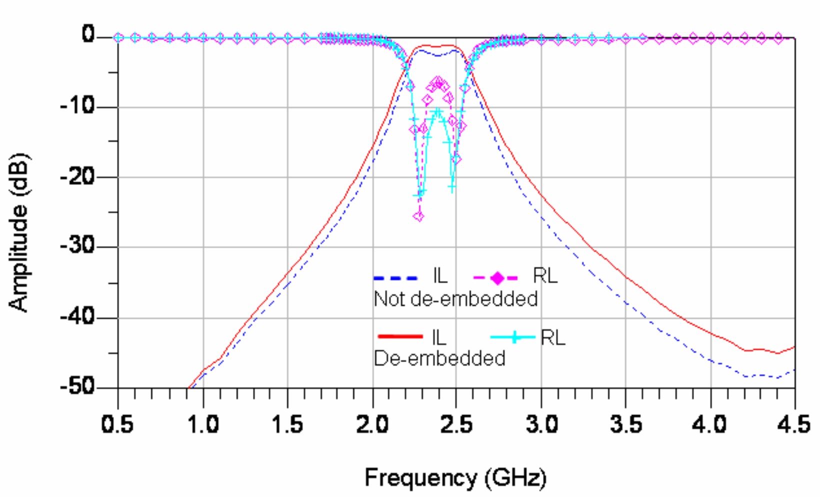

Figure 5. 7 De-embedded and not de-embedded measured results

Figure 5.7 shows the de-embedded and not de-embedded measurement results of bandpass filter C1 in terms of insertion (IL) and return loss (RL). As can be seen, this effect is slightly below 2 dB and can be neglected. The de-embedded return loss as well as insertion loss is improved at the midband frequency in about 6 dB, and 2 dB, respectively. The effect of the de-embedding is in general less noticeable because the adapter structures are much smaller compared to the filter structures in terms of their guide wavelength.

5.4.2 RF Measurements vs. EM Simulations

In order to verify the filter design and modeling approaches, the de-embedded measurement and simulation results of some bandpass filters, listed in Table 5.1, are compared.

Table 5. 1 List of measured and simulated BPFs used for the design methodology verification

Design name	f_0	Topology	Configuration	Order
A1	1950MHz	Tap & short-ended	Vertical with off-set	2-pole BPF
A2	1950MHz	Tap & short-ended	Vertical without off-set	2-Pole BPF
B1	2140MHz	Tap & short-ended	Vertical with off-set	2-Pole BPF
B2	2140MHz	Tap & short-ended	Vertical without off-set	2-Pole BPF
C1	2440MHz	Tap & short-ended	Vertical with off-set	2-Pole BPF
C2	2440MHz	Tap & short-ended	Vertical without off-set	2-Pole BPF
F	5220MHz	Gap & open-ended	Lateral	2-Pole BPF

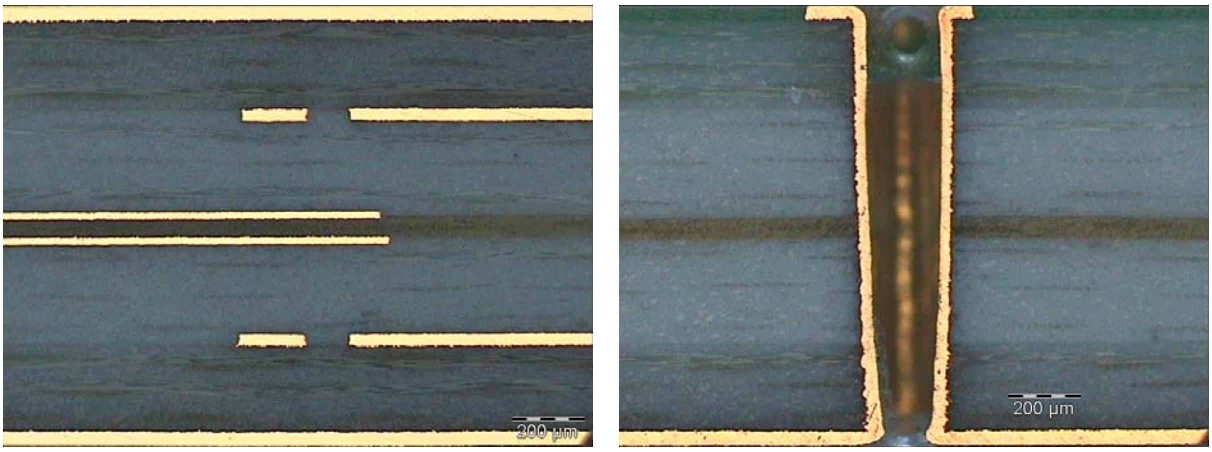

(a) (b)

Figure 5. 8 Photography of the fabricated PCB showing a) the substrate cross-section, and b) the through-via

Figure 5.8 presents the photography of the fabricated PCB showing the substrate cross-section with six metallization layers and through-via connecting the ground layers. The total thickness of the substrate is 53.1 mil.

5.4.2.1. Design Example of a 2.4-GHz Bandpass Filter

This filter was designed to operate at 2440 MHz frequency. Its design consists in two short-terminated resonant inductors, which are capacitively coupled and arranged in vertical configuration. The first inductor was realized on ML2, while the second inductor was realized on ML5. The total length of each inductor is 740 mil. The inductive I/O-ports are realized with tap-lines of length 94 mil, which are located at 109 mil from the short-ended terminal.

This design was implemented in two different configurations: “vertical configuration with off-set between the resonant elements” that we call “filter C1”, and “vertical configuration without off-set between the resonant elements” that we call “filter C2”. Between its resonant elements, ground planes with EM windows of size 60 x 76 mil² (in AB-direction) were inserted in layers ML3, and ML4, in such a way to control the EM flux between the resonant elements. The layouts of both these approaches are shown in Figure 5.9.

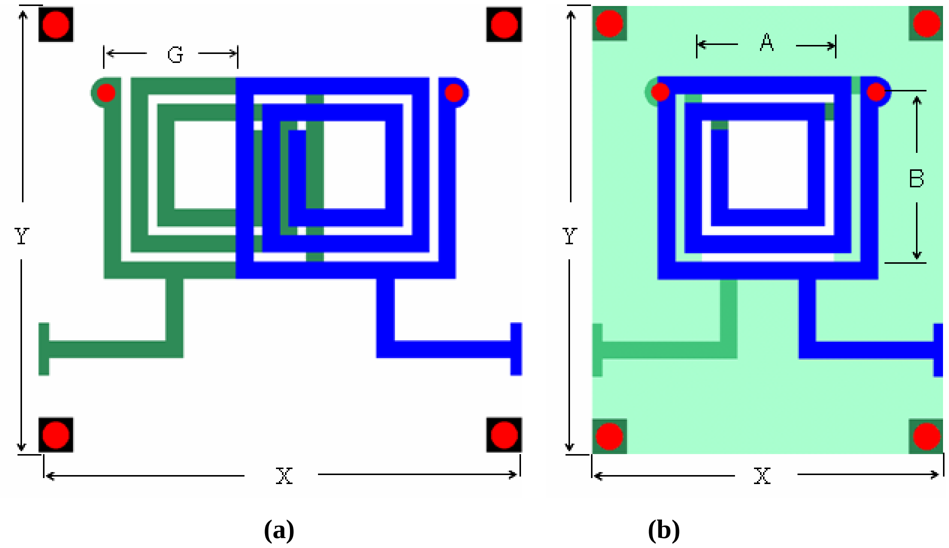

Figure 5. 9 Layout of a) filter C1 and b) filter C2

Both the designs were fabricated using six-metal-layer MCM-L technology and the photography of the top-view of the fabricated filters is shown in Figure 5.10.

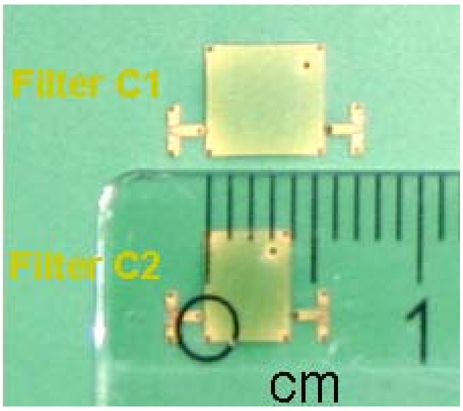

Figure 5. 10 Photography of the top-view of fabricated filter C1 and filter C2

These designs were full-wave EM simulated using the Method of Moments (MoM) codes. The measurement and simulation results of both the design approaches are presented in the following.

Filter C1

The filter size in XY-directions including adapters was 360 x 203 mil² and without adapters was 220 x 203 mil². The off-set between the resonant elements was G = 60 mil. The measurement and simulation results of this filter are shown in Figure 5.11 in terms of IL and RL.

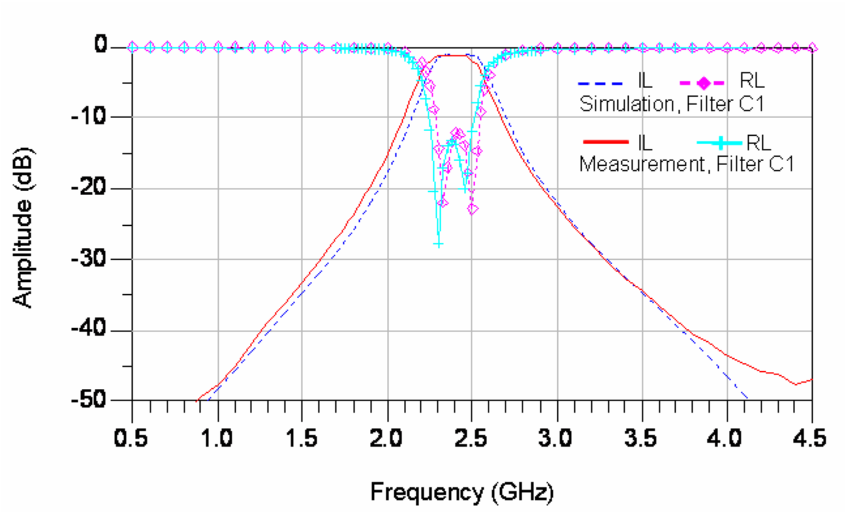

Figure 5. 11 Measured and simulated responses of filter C1

As can be seen in this figure, there is a good correlation between simulation and measurement data. But, there is a slight shift of 10 MHz for the center frequency (f_0). The reason of this shift can be attributed to the technology tolerance occurring during the manufacturing. Furthermore, at frequencies greater than 3.8 GHz, there is a shift between simulation and measurement data. This may be attributed to the measurement/de-embedding accuracy. The midband IL and RL are -1.19 dB and -15.30 dB for the measurement, and -1.15 dB and -13.60 dB for the simulation, respectively. The center frequency and 3-dB-bandwidth are 2.39 GHz and 300 MHz for the measurement and 2.4 GHz and 300 MHz for the simulation, respectively.

Another important parameter for the evaluation of bandpass filters is the filter group delay (τ_d). In some applications such as multiplexing filters for communication systems, it is important to have linear-phase filter response in order to avoid the signal distortion.

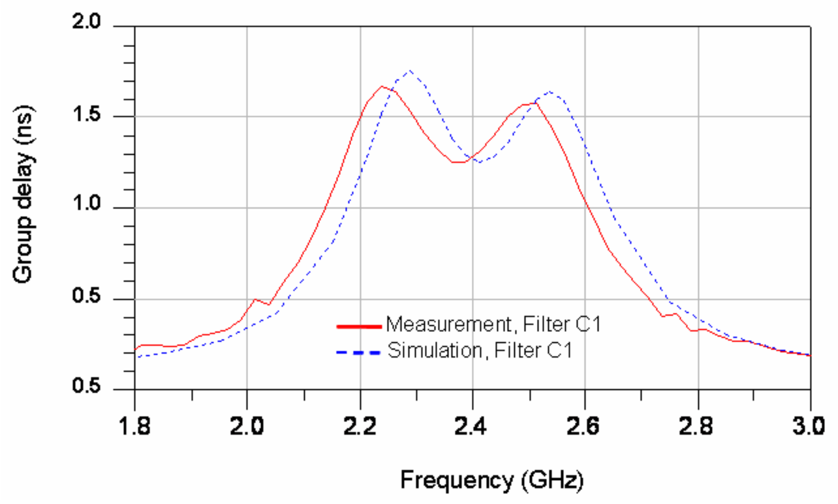

Figure 5. 12 Measured and simulated group delays of filter C1

Figure 5.12 shows the group delays of filter C1. As can be seen from this figure, these group delays present ripples in the passband, which are in the order of a small fraction (27 %).

Filter C2

The size (in XY-directions) of filter C2 including adapters was 290 x 203 mil² and without adapters was 160 x 203 mil². The measurement and simulation results of this filter are shown in Fig. 5.13 in terms of insertion loss (IL) and return loss (RL).

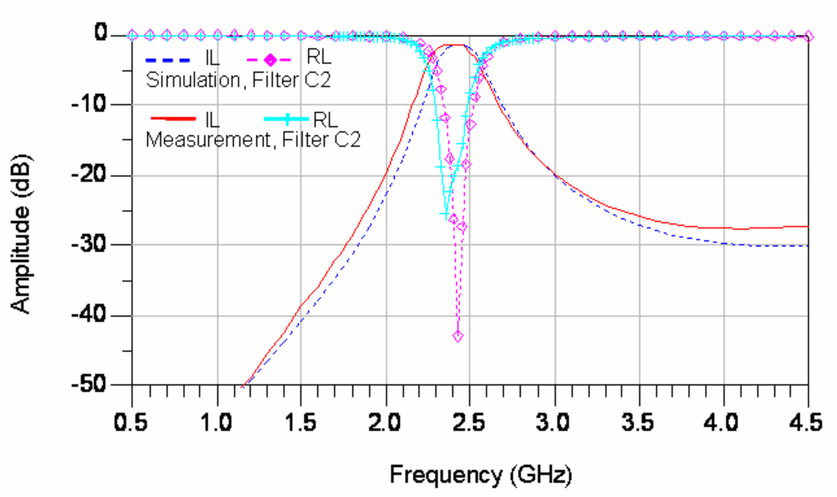

Figure 5. 13 Measured and simulated responses of filter C2

As can be seen in this figure, there is also a good correlation between measurement and simulation data. But for frequencies greater than 3.5 GHz, there is a shift between simulation and measurement in terms of IL. This shift can be attributed to the technology tolerances. There is also a small shift of 20 MHz in terms of the center frequency and of 20 MHz in terms of the bandwidth. The same shift of 20 MHz can also be noticed in terms of return losses. The midband insertion (IL) and return loss (RL) are -1.34 dB and -20.1 dB for the measurement, and -1.54 dB and -21.16 dB for the simulation, respectively. The center frequency and 3-dB-bandwidth are 2380 MHz and 250 MHz for the measurement, and 2400 MHz and 230 MHz for the simulation, respectively. The relative deviations between measurement and simulation for all important parameters amount to a maximum of 15 %.

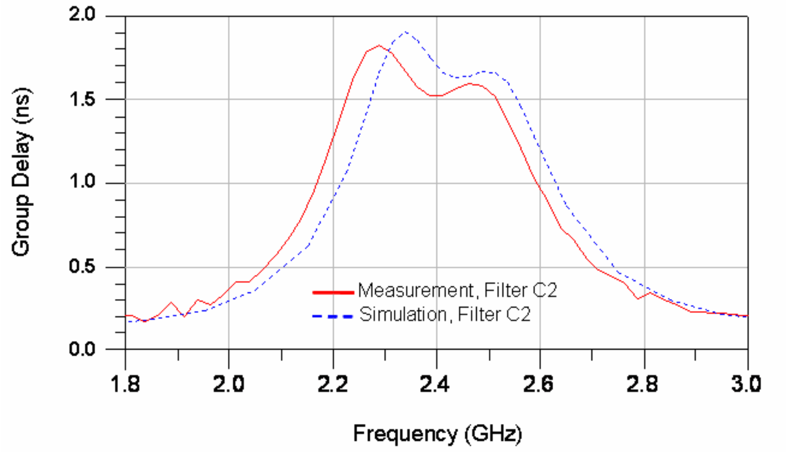

Figure 5. 14 Measured and simulated group delays of filter C2

The group delay of this filter is shown in Figure 5.14. As can be seen, the response of this filter is almost linear-phase in the passband. The ripples are in the order of a small fraction (17 %).

Filter C1 vs. Filter C2

In order to evaluate the efficiency of this design approach in terms of the miniaturization and performance, the measurement data of filter C1 and filter C2 are plotted in Figure 5.15 for the comparison.

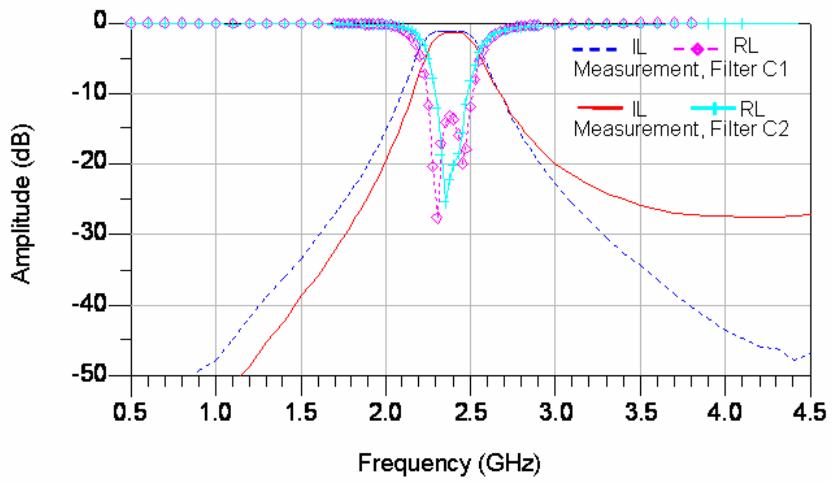

Figure 5. 15 Measurement data of filter C1 versus filter C2

As can be seen from this figure, the center frequencies of the both filters match very well. But, there is a slight shift of 50 MHz in terms of the bandwidth and for frequencies greater than 2.8 GHz, there is an increasing shift between the IL of filter C1 and filter C2. This shift can be attributed to the frequency-dependent coupling between the resonant inductors. For frequencies less than 2.8 GHz, there is no noticeable degradation of filter characteristics. Concerning the RL, there is no important degradation of filter characteristics. The results of this comparison are summarized in Table 5.2 for the most important parameters.

Table 5. 2 Measurement results for the 2-pole bandpass filter C1 versus filter C2

Filter	f_0 (MHz)	IL (dB)	RL (dB)	3-dB-BW (MHz)	Size (mil²)
Filter C1	2380	-1.19	15.30	300	220x203 =(44660)
Filter C2	2380	-1.34	20.10	250	160x203 =(32480)
Deviation	0	-0.15	4.80	50	(15180)
Rel. deviation	0.00%	-12.60%	+26.17%	+16.67%	-27.27%

The difference in terms of IL between filter C1 and filter C2 can be attributed to the copper conductor losses of the inner-metal-layers (ML3 and ML4), which were used to design the EM windows inserted between the resonant inductors in filter C2. As can be seen, the size of filter C2 is reduced by about 27 % without any noticeable degradation of the filter characteristics within the passband.

5.4.2.2. Design Example of a 1.9 GHz Bandpass Filter

This example shows the characterization of a bandpass filter that was designed to operate at 1950 MHz frequency. Its design consists of two short-terminated inductors, which are capacitively coupled and arranged in vertical configuration. The first inductor was realized on the second metal layer (ML2), whereas the second inductor was realized on the fifth metal layer (ML5). The total length of each inductor was 892 mil. The inductive I/O-ports were realized with tap-lines of length 84 mil, which are located at 125 mil from the short-ended terminal.

This design was implemented in two different configurations: “vertical configuration with off-set between the resonant elements” that we call “filter A1” and “vertical configuration without off-set between the resonant elements” that we call “filter A2”. The focus thereby was the design miniaturization and performance improvement.

The layouts of both these approaches are similar to those of filter C, with the only difference in the design parameter values. Therefore, these layouts are not presented here.

The designs of both these filters were also full-wave EM simulated using the MoM codes.

Filter A1

The filter size (in XY-directions) including adapters was 366 x 194 mil² and without adapters was 236 x 194 mil². The off-set between the resonant elements (in X-directions) was 40 mil. The measurement and simulation results of this filter are shown in Figure 5.16 in terms of insertion loss (IL) and return loss (RL).

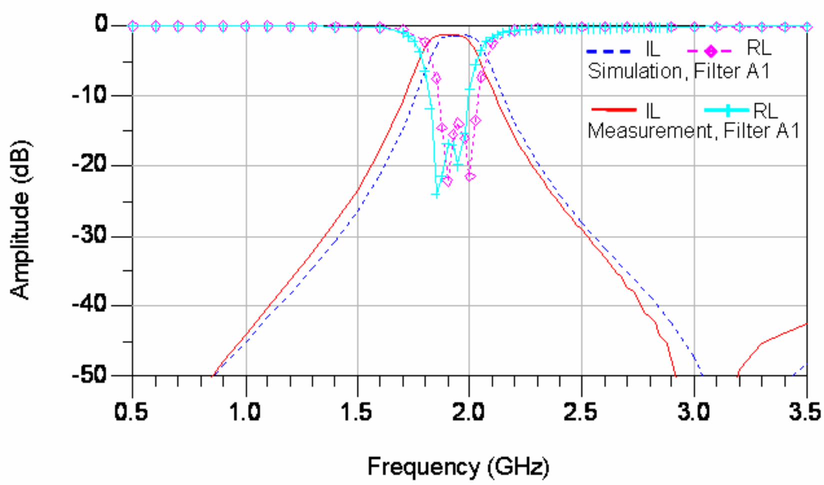

Figure 5. 16 Measured and simulated responses of filter A1

As can be seen in this figure, there is a good correlation between simulation and measurement data. But, there is a slight shift of 25 MHz in terms of the center frequency (f_0). The reason of this shift can be attributed to the technology tolerance occurring during the manufacturing. These filter responses show the presence of transmission zeros on the upper side of the passband, at about 3 GHz; around this frequency, there is a shift between simulation and measurement data. This may be attributed to the technology tolerance occurring during the manufacturing as well as to the measurement or/and the de-embedding accuracy. The midband IL and RL are -1.29 dB and -17.02 dB for the measurement, and -1.35 dB and -13.93 dB for the simulation, respectively. The center frequency and 3-dB-bandwidth are 1.925 GHz and 220 MHz for the measurement and 1.950 GHz and 200 MHz for the simulation, respectively.

Filter A2

The filter size (in XY-directions) including adapters was 278 x 194 mil² and without adapter was 148 x 194 mil². Between its resonant elements, ground planes with EM windows of size 72 x 88 mil² (in AB-directions) were inserted in layers ML3, and ML4, in such a way to control the EM flux between the resonant elements. The measurement and simulation results of this filter are shown in Figure 5.17 in terms of insertion loss (IL) and return loss (RL).

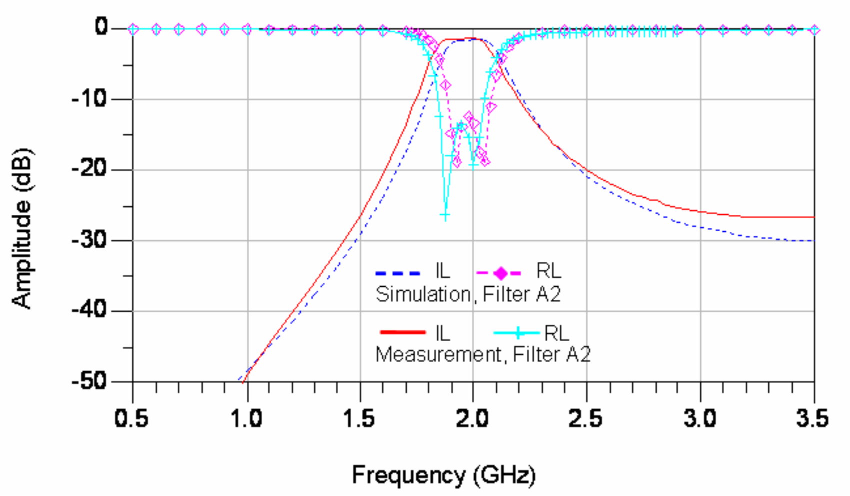

Figure 5. 17 Measured and simulated response of filter A2

As can be seen in this figure, there is also a good correlation between simulation and measurement data. There is a slight shift of 20 MHz in terms of the center frequency (f_0), due to the technology tolerance occurring during the manufacturing. For frequency greater than 2.6 GHz, there is an increasing shift between simulation and measurement. This shift can be attributed to the frequency dependent coupling between the resonant elements. The midband IL and RL are -1.37 dB and -13.47 dB for the measurement, and -1.59 dB and -12.36 dB for the simulation, respectively. The center frequency and 3-dB-bandwidth are 1.95 GHz and 250 MHz for the measurement and 1.97 GHz and 220 MHz for the simulation, respectively.

Filter A1 vs. Filter A2

In order to evaluate the efficiency of this design approach in terms of the miniaturization and performance, the measurement results of filter A1 and filter A2 are plotted in Figure 5.18 for the comparison.

As can be seen from this figure, there is a slight mismatch of 25 MHz in terms of center frequencies, and 30 MHz in terms of 3-dB-bandwidth. The shift in terms of center frequency is due to the differences in terms of the inductor total length. Longer structures lead to lower center frequency and shorter structures lead to the higher center frequency. Wider EM windows lead to stronger coupling, and strong coupling between the resonant elements increases the bandwidth. Smaller EM windows lead to weaker coupling, and weak coupling decreases the bandwidth. For frequencies greater than 2.1 GHz, there is an increasing shift between the IL of filter A1 and filter A2. This shift can be attributed to the frequency dependent coupling between the resonant elements.

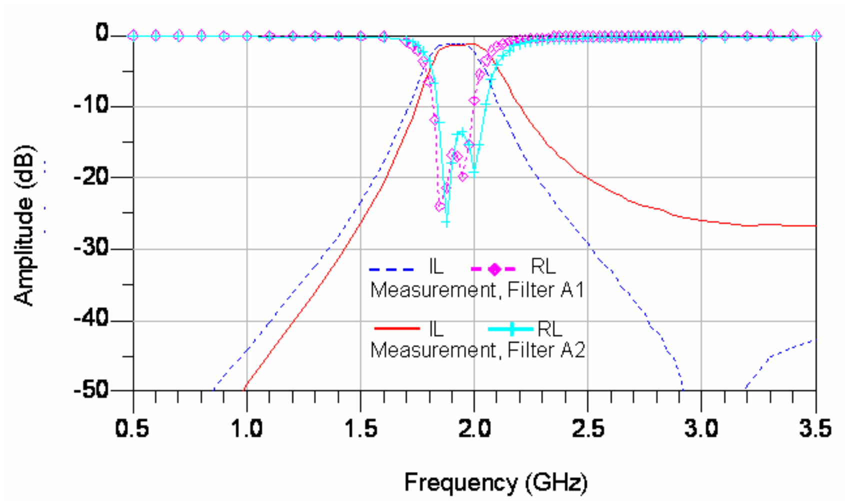

Figure 5. 18 Measured responses of filter A1 versus filter A2

The results of this comparison are summarized in Table 5.3 for the most important parameters.

Although filter A2 has presented a smaller size, and acceptable characteristics within the passband, its electrical performance beyond the passband is slightly degraded compared to the performance of filter A1. The cross-sectional studies of the manufactured devices can contribute to the accurate justification of this deviation.

Table 5. 3 Measurement results for filter A1 versus filter A2

Filter	f_0 (MHz)	IL (dB)	RL (dB)	3-dB-BW (MHz)	Size (mil²)
Filter A1	1925	-1.29	-17.02	220	236 x 194 =(45784)
Filter A2	1950	-1.37	-13.47	250	148 x 194 =(28712)
Deviation	25	0.08	3.55	30	-17072
Rel. deviation	1.30%	-6.20%	-20.86%	+13.64%	-37.2%

5.4.2.3. Design Example of a 2.1 GHz Bandpass Filter

This filter was designed to operate at 2140 MHz frequency. Its design consists of two short-terminated resonant elements, which are capacitively coupled and arranged in vertical configuration. The first inductor was realized on the second metal layer (ML2), while the second inductor was realized on the fifth metal layer (ML5). The total length of each resonator is 792 mil. The inductive I/O-ports are realized with tap-lines of length 91 mil, which are located at 121 mil from the short-ended terminal.

This design was implemented in two different configurations: “vertical configuration with off-set between the resonant elements” that we call “filter B1”, and “vertical without off-set between the resonant elements” that we call “filter B2”.

Both the designs are similar to those of filter C and filter A, with the only difference in the design parameter values. The measurement and simulation results of both the design approaches are presented in the following.

Filter B1

The filter size (in XY-directions) including adapters was 360 x 200 mil² and without adapters was 230 x 200 mil². The off-set (in X-direction) between the resonant elements was G = 64 mil. Figure 5.19 shows the measured and simulated results in terms of insertion loss (IL) and return loss (RL).

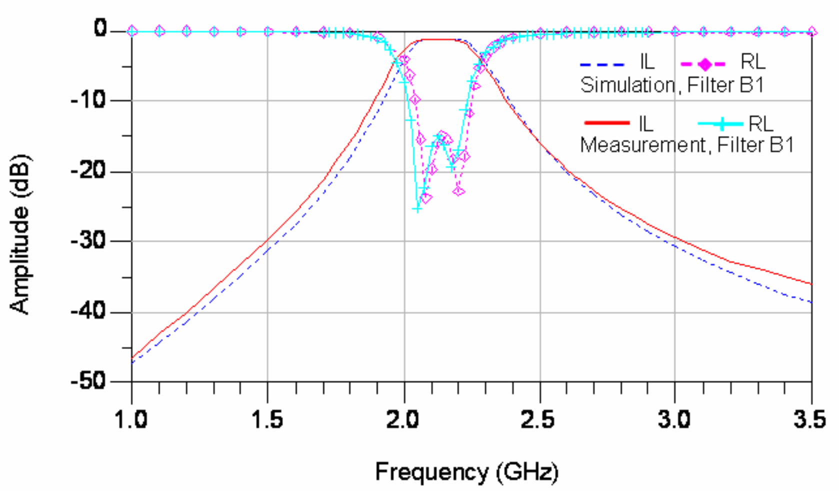

Figure 5. 19 Measured and simulated responses of filter B1

As can be seen in these plots, there is a good correlation between simulation and measurement data. But, there is a slight shift of 10 MHz for the center frequency (f_0). The reason of this shift can be attributed to the technology tolerance occurring during the manufacturing. The midband IL and RL are -1.13 dB and -20.03 dB for the measurement, and -1.21 dB and -14.85 dB for the simulation, respectively. The center frequency and 3-dB-bandwidth are 2.13 GHz and 250 MHz for the measurement, and 2.14 GHz and 260 MHz for the simulation, respectively.

Filter B2

The filter size including adapters was 296 x 200 mil² and without adapter was 166 x 200 mil². Between its resonant elements, ground planes with EM windows of size 87.5 x 88 mil² in (AB-direction) were inserted into ML3 and ML4, in such a way to control the EM flux between the resonant elements.

The measurement and simulation results of this filter are shown in Figure 5.20 in terms of insertion loss (IL) and return loss (RL).

As can be seen in this figure, there is also a good correlation between simulation and measurement data. Also here, there is a slight shift of 10 MHz for the center frequency (f_0). The reason of this shift can also be attributed to the technology tolerance occurring during the manufacturing. The midband IL and RL are -1.20 dB and -14.03 dB for the measurement, and -1.43 dB and -14.05 dB for the simulation, respectively.

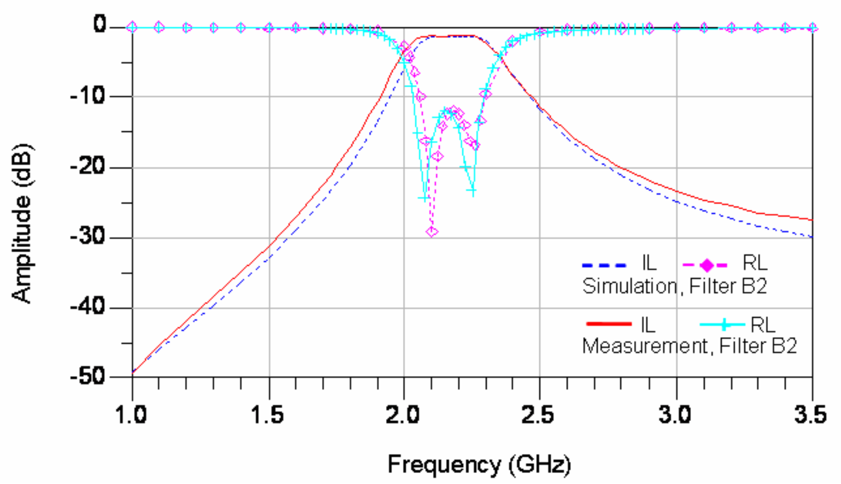

Figure 5. 20 Measured and simulated responses of filter B1

The center frequency and 3-dB-bandwidth are 2.15 GHz and 280 MHz for the measurement, and 2.14 GHz and 250 MHz for the simulation, respectively.

Filter B1 vs. Filter B2

In order to evaluate the efficiency of this design approach in terms of the miniaturization and performance, the measured responses of filter B1 and filter B2 are plotted in Figure 5.21 for the comparison.

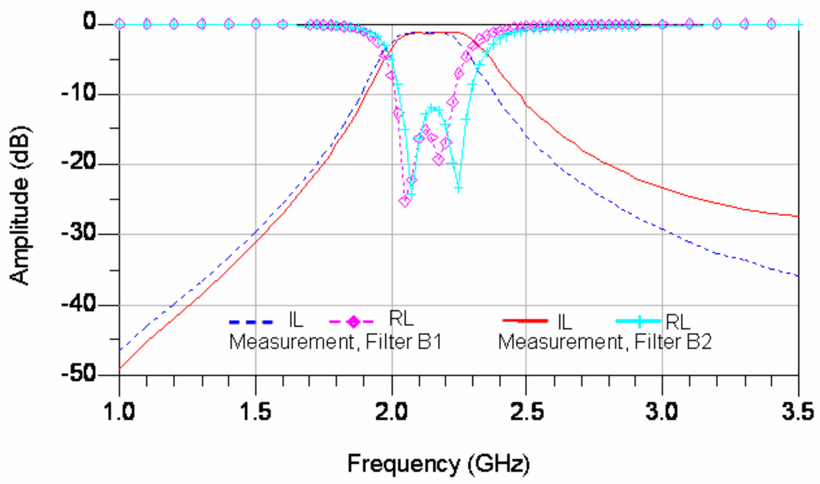

Figure 5. 21 Measured responses of filter B1 versus filter B2

As can be seen from this figure, the center frequencies of the both filters match very well. But, there is a slight shift of 25 MHz in terms of the bandwidth. For frequencies greater than 2.8 GHz, there is an increasing shift between the IL of filter B1 and filter B2. This shift can be attributed to the frequency-dependent coupling between the resonant elements. For frequencies less than 2.8 GHz, there is no noticeable degradation of filter characteristics. Concerning the RL, there is no important degradation of filter characteristics. The results of this comparison are summarized in Table 5.4 for the most important parameters.

Table 5. 4 Measurement results for filter B1 versus filter B2

Filter Analysis	f_0 (MHz)	IL (dB)	RL (dB)	3-dB-BW (MHz)	Size (mil²)
Filter B1	2130	1.13	20.03	250	230 x 200 =(46000)
Filter B2	2150	1.20	14.03	300	166 x 200 =(33200)
Deviation	20	0.07	-6	25	-12800
Rel. deviation	0.94%	+6.20%	-29.96%	+10.0%	-27.8%

The difference in terms of the passband insertion losses between filter B1 and filter B2 can be attributed to the copper-conductor losses of the inner-metal-layers (ML3 and ML4), which were used to design the EM windows. As can be seen, the size of filter B2 is reduced by about 27 % without any noticeable degradation of the filter characteristics within the passband.

5.4.2.4. Design Example of a 5.2 GHz Bandpass Filter

This filter was designed to operate at 5200 MHz. Its design consists of two open-terminated inductors, which are capacitively coupled and arranged in "lateral configuration". Both the inductors are realized on the second metal layer (ML2) and are separated each other by a spacing G. Let us call this design "filter F", the layout of which is shown in Figure 5.22.

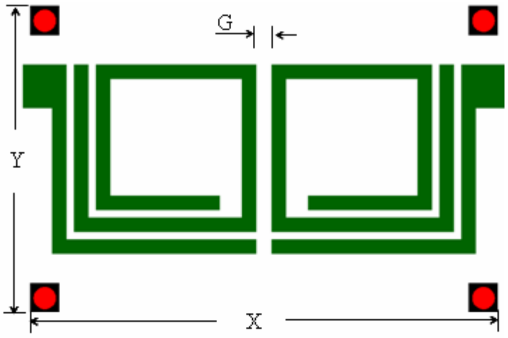

Figure 5. 22 Layout of filter F

The total length of each inductor was 484 mil. The capacitive I/O-ports are realized with gap topology with a gap spacing of 4 mil. The spacing between the inductors was G = 8 mil. The filter size (in XY-directions) including adapters was 386 x 168 mil² and without adapters was 256 x 168 mil².

This design was EM simulated using the Method of Moments (MoM) codes. The measurement and simulation results of this filter are shown in Figure 5.23 in terms of insertion loss (IL) and return loss (RL).

As can be seen in this figure, there is a slight shift of 10 MHz in terms of the center frequency (f_0), and a shift of 70 MHz in terms of the bandwidth. These shifts can be attributed to the technology tolerance occurring during the manufacturing. The responses of this design show two transmission zeros on the left and right sides of the passband. The transmission zeros on the left side match together, while the transmission zeros on the right side mismatch in about 200 MHz and 12 dB. This mismatch may be attributed to the measurement accuracy as well as de-embedding accuracy.

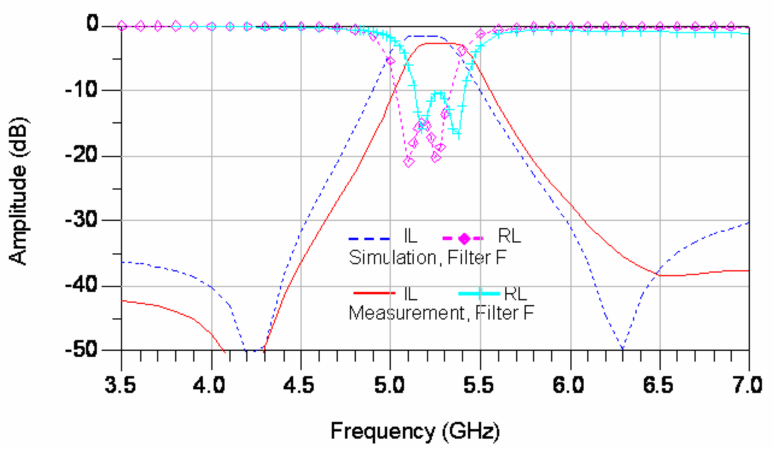

Figure 5. 23 Measured and simulated responses of filter F

The values of the midband IL and RL are -2.63 dB and -11.13 dB for the measurement, and -1.60 dB and -15.43 dB for the simulation, respectively. The center frequency and 3-dB-bandwidth are 5.3 GHz and 230 MHz for the measurement, and 5.2 GHz and 300 MHz for the simulation, respectively. For the accurate evaluation of this behaviour, further investigations in terms of EM simulations and RF characterizations are required.

5.5. Summary

This chapter presented the characterization of bandpass filters through RF measurements. Before performing the measurements, the test-equipment was calibrated using the "line-reflect-reflect-match" (LRRM) calibration method. Different structures on the test-board were selected and their S-parameters were measured in the frequency range from 100 MHz to 10 GHz. The influence of the adapters was removed from the measurement data and the real filters under test were characterized. Finally, the measurement and simulation results were compared. As could be seen, there was a good correlation between measurement and simulation data.

This correlation was very good, particularly within the passband. There was a slight discrepancy in the upper stopband, which could be attributed to the measurement or de-embedding accuracy.

The efficiency of the design approach for the further miniaturization of these filters using "vertical configuration without off-set between the resonant elements" proves well within the passband and lower stopband.

In the upper stopband, there was an increasingly shift in terms of the attenuation, between filters realized in "vertical configuration without off-set between the resonant elements" and those realized in "vertical configuration with off-set between the resonant elements". These discrepancies, which are due to the frequency-dependent coupling, could be improved by better control of the EM fields between the resonant elements. In addition, further investigations in terms of EM simulations are necessary for accurate explanations of this behaviour.

Although there was a slight shift in terms of center frequency, bandwidth, insertion loss, as well return loss, the correlation between simulation and measurement data of filter F is acceptable.

Even here, further investigations in terms of EM simulations are required for lucid explanations of this behaviour.

All in all, a good matching between the measurement and simulation results was obtained. The amount of the deviation between the measurement and simulation data is less than 10 % for all electrical parameters.

Chapter 6

Conclusions

In this work, an efficient methodology developed for the design/integration of miniaturized bandpass filters for RF/wireless applications was presented. Based on the transmission line techniques, the fundamental elements L, C, and LC of filter circuits were approximated using sections of microstrip lines. Microstrip spiral inductors were designed with rectangular-shaped structures, the shortest electrical length of which was π or $\pi/2$ dependent on the design topology. These inductors, which were used to design the bandpass filters, provided the inductances as well as parasitic capacitances due to the inter-winding and ground plane. Using of this parasitic reactance in the filter design led to a substantial reduction in component count as well as in design size.

For the design implementation, an adequate integration medium offering the advantage of reduction of radiation losses and EMI interferences was defined. Different design topologies and configurations were derived for the second order bandpass filters: “gap topology”, “tap topology”, “lateral configuration”, “vertical configuration with off-set between the resonant elements”, and “vertical configurations without off-set between resonant elements”. For the filter design implementation in “vertical configuration without off-set between the resonant elements”, ground planes designed with electromagnetic (EM) windows were placed between the resonant elements in such a way to control the EM coupling happening between the resonant elements.

“Gap topology” offered the realization of selective filters with very narrowband characteristics. “Tap topology” offered the implementation of sensitive filter with narrowband characteristics. “Lateral configuration” presented a capability of realization of sensitive filters, but at the coast of larger bandwidth. “Vertical configuration with off-set between the resonant elements” presented the ability of design miniaturization. “Vertical configuration without off-set between the resonant elements” offered also the ability of design miniaturization, but at the cost of lower steepness on the upper side of the passband. Generally, designs with “gap topology” in “vertical configuration without offset between the resonant elements” offered the realization of filters with narrowband characteristics, due to the easy controllable coupling between the filter elements.

The bandwidth was proved most sensitive against the thickness tolerances (coming from the manufacturing process fluctuations). The impact of dielectric constant tolerances on the filter characteristics was insignificant for the defined integration medium.

Based on this methodology, different second order bandpass filters for various applications such as Wi-Fi, and WIMAX were designed and implemented in multi-chip-modules laminate (MCM-L) based system-in-package (SiP) technology. The design integration in “vertical configuration without off-set between the resonant elements” has exhibited a size reduction of up to 27 %, without noticeable performance degradation within the passband.

The methodology as well as the modeling and analysis approaches were verified and validated, through on-board RF measurements. There were good correlations between simulation and measurement results of the second order bandpass filters.

Downscaling of the filter structures under test showed good agreement for simulation of inductors down to an area of 75 mil^2. Further decrease led to considerable degradation of the filter characteristics IL and RL thus, limiting the miniaturization approach.

Appendix

Table A. 1 Physical constants

Constant	Symbol	Value
Permittivity of Vacuum	ε_0	$8.854\times10^{-12} \cong (1/36\pi)\times10^{-9}$ F/m
Permeability of Vacuum	μ_0	$4\pi\times10^{-7}$ H/m
Impedance of free space	η_0	$373.7 \cong 120\pi\ \Omega$
Velocity of light	c	2.998×10^{8} m/sec
Charge of electron	e	1.602×10^{-19} C
Masse of electron	m	9.107×10^{-31} Kg

Table A. 2 Conductivity of some metals at 25 °C (300 K)

Materials	Electrical conductivity (S/m)	Thermal conductivity K(W/m °C)
Silver (S)	$6.17\text{x}10^{7}$	429
Copper (Cu)	$5.76\text{x}10^{7}$	393
Gold (Au)	$4.10\text{x}10^{7}$	297
Aluminum (Al)	$3.72\text{x}10^{7}$	240
Nickel (Ni)	$1.45\text{x}10^{7}$	92

Table A. 3 Conversion factors and units

dB	$10\log_{10}$(Power ratio)
Power ration	$10^{dB/10}$
1 foot (ft)	0.305 m
1 mil	25.4 µm
1 mile	1.609 km

Bibliography

[1.1] R. K. Ulrich and L. W. Schaper, "Integrated Passive Component Technology", IEEE Press, Wiley-Interscience, New Jersey, 2003, chap.1.

[2.1] E. Shuster, "Wireless Data Access–Technology, Range and Convergence", IntelliClear Inc. free white paper, no. 3, January 2005, pp. 1–18, available at: http://www.intelliclear.com/free_whitepapers.html.

[2.2] M. McMahan, A. Khatzibadeh, and Pradeep Shah, "Wireless Systems and Technology Overview", Texas Instruments internal white paper, 8/95.

[2.3] M. McMahan, "Evolving Cellular Handset Architectures but an Insatiable Desire for DSP MIPS Application", Texas Instruments Technical Journal, vol. 17, no. 1, March 2000.

[2.4] J.E. Padgett, C.G. Gunther, and T. Hattori, "Overview of wireless personal communications", IEEE Communications Magazine, vol. 33, no. 1, January 1995, pp. 28–41.

[2.5] D.J. Goodman, "Trends in cellular and cordless communications", IEEE Communications Magazine, vol. 29, no. 6, June 1991, pp. 31–40.

[2.6] R. Weigel, et. al., "RF Transceiver Architectures for W-CDMA Systems like UMTS: State of the Art and Future Trends", International Symposium on Acoustic Wave Devices, Chiba, Japan, March 2001.

[2.7] B. Razavi, "RF Microelectronics", Prentice-Hall, Upper Saddle River, 1998.

[2.8] Sheng-Fuh R. Chang, et. al., "A Dual-Band RF Transceiver for Multistandard WLAN Applications", IEEE Transactions on Microwave Theory and Techniques, vol. 53, no. 3, March 2005, pp. 1048–1055.

[2.9] R. Levy, R. V. Snyder, and G. Matthaei, "Design of Microwave Filters", IEEE Transactions on Microwave Theory and Techniques, vol. 50, no. 3, March 2002, pp. 783–793.

[2.10] J.N. Burghartz, and B. Rejaei, "On the design of RF spiral inductors on silicon", IEEE Transactions on Electron Devices, vol. 50, no. 3, March 2003, pp. 718–729.

[2.11] Wei-Zen Chen and Wen-Hui Chen, "Symmetric 3D Passive Components for RF ICs Applications", IEEE Radio Frequency Integrated Circuits (RFIC) Symposium, June 2003, pp. 599–602.

[2.12] O.H. Murphy, et. al., "Design of Multiple-Metal Stacked Inductors Incorporating an Extended Physical Model", IEEE Transactions on Microwave Theory and Techniques, vol. 53, no. 6, Part 2, June 2005, pp. 2063–2072.

[2.13] Ju-Ho Son, et. al. "Multi-level monolithic 3D inductors on silicon", Proceedings of the 44th IEEE Midwest Symposium on Circuits and Systems, vol. 2, August 2001, pp. 854–857.

[2.14] H. Feng, et. al., "Super compact RFIC inductors in 0.18 μm CMOS with copper interconnects", IEEE Radio Frequency Integrated Circuits (RFIC) Symposium, June 2002, pp. 443–446.

[2.15] J. Zou, et. al., "Development of Three-Dimensional Inductors Using Plastic Deformation Magnetic Assembly (PDMA)", IEEE Transactions on Microwave Theory and Techniques, vol. 51, no. 4, April 2003, pp. 1067–1075.

[2.16] H.-Y. Tsui, and J. Lau, "An On-Chip Vertical Solenoid Inductor Design for Multigigahertz CMOS RFIC", IEEE Transactions on Microwave Theory and Techniques, vol. 53, no. 6, Part 1, June 2005, pp. 1883–1890.

[2.17] Yan Zhuang, et. al., "Integrated solenoid inductors with patterned, sputter-deposited Cr/Fe/sub 10/Co/sub 90//Cr ferromagnetic cores", IEEE Electron Device Letters, vol. 24, no. 4, April 2003, pp. 224–226.

[2.18] Jr-Wei Lin, et. al., "An optimum design of the micro-machined RF inductor"; IEEE Radio Frequency Integrated Circuits (RFIC) Symposium, June 2004, pp. 639–642.

[2.19] K.J. Chen, et. al., "CMOS-compatible micromachined edge-suspended spiral inductors with high Q-factors and self-resonance frequencies", IEEE Electron Device Letters, vol. 25, no. 6, June 2004, pp. 363–365.

[2.20] C. P. Yue, and S. S. Wong, "On-Chip Spiral Inductors with Patterned Ground Shields for Si-Based RF IC's", IEEE Journal of Solid-State Circuits, vol. 33, no. 5, May 1998, pp. 743–752.

[2.21] Kelin J. Kuhn, et al., "Integration of Mixed-Signal Elements into a High-Performance Digital CMOS Process" Intel Technology Journal vol. 6, no. 2, May 2002, pp. 31–41, available at: http://www.intel.com/sites/corporate/tradmarx.htm.

[2.22] I. D. Robertson, and S. Lucyszyn, "RFIC and MMIC Design and Technology", IEE, London, November 2001, chap. 3.

[2.23] T. Kamgaing, et al., "Future Package Technologies for Wireless Communication Systems", Intel Technology Journal, vol. 09, no. 04, November 2005, pp. 353-364 available :http://developer.intel.com/technology/itj/2005/volume09issue04/art08_futurepackagetech/p01_abstract.htm.

[2.24] N. Dib, J. Ababneh, and A. Omar, "CAD Modeling of Coplanar Waveguide Interdigital Capacitor", International Journal of RF & Microwave Computer-Aided Engineering, vol. 15, no. 6, November 2005, pp. 551–559.

[2.25] M. G. Banciu "Radio Frequency and Microwave Design Methods for Mobile Communications", Ph.D. Dissertation, University of University of New South Wales, Sydney, Australia, 2003.

[2.26] M. Lahti, T. Jaakola, and V. Kondratyev, "Integrated millimeter-wave band-pass filters in LTCC modules", IMAPS Nordic 2003, September 2003, pp. 62–66.

[2.27] Hong-Ming Lee, et al., "Dual-band coupling and feed structure for microstrip filter design", IEEE MTT-S International Microwave Symposium Digest, vol. 3, June 2004, pp. 1971–1974.

[2.28] Sheng Sun, and Lei Zhu, "Compact dual-band microstrip bandpass filter without external feeds", IEEE Microwave and Wireless Components Letters, vol. 15, no. 10, October 2005, pp. 644–646

[2.29] E. Shih, Jen-Tsai Kuo, “A new compact microstrip stacked-SIR bandpass filter with transmission zeros”, IEEE MTT-S International Microwave Symposium Digest, vol. 2, June 2003, pp. 1077–1080.

[2.30] G. L. Matthaei, "Narrow-Band, Fixed-Tuned, and Tunable Bandpass Filters with Zig-Zag Hairpin-Comb Resonators”, IEEE Transactions on Microwave Theory and Techniques, vol. 51, no. 3, March 2003, pp. 1215–1219.

[2.31] Dana Brady, “The Design, Fabrication and Measurement of Microstrip Filter and Coupler Circuits”, Technical Articles in High Frequency Electronics Journal, July 2002, vol. 1, no. 1, pp. 22–30.

[2.32] M. A. Imparato, R. C. Groulx, and R. Matarazzo, “Design of a Microstrip Bandpass Filter Using Advanced Numerical Methods”, Technical Articles in High Frequency Electronics Journal, March 2004, vol. 3, pp. 20–29.

[2.33] C. J. Kikkert, “Designing Low Cost Wideband Microstrip Bandpass Filters”, IEEE Tencon 05, Melbourne, Australia, November 2005.

[2.34] D. D. Nordquist, et al., “X-band RF MEMS tuned combline filter”, Electronics Letters, vol.41, no.2, January 2005, pp.76-77.

[2.35] I.C. Hunter, L. Billonet, B. Jarry, and P. Guillon, “Microwave filters applications and technology”, IEEE Transactions on Microwave Theory and Techniques, vol. 50, no. 3, March 2002, pp. 794–805.

[2.36] M. N.O. Sadiku, "Numerical Techniques in Electromagnetics”, CRC Press, Boca Raton, 1992, chap. 1.

[2.37] D. G. Swanson, Jr., W. J.R. Hoefer, “Microwave Circuit Modeling Using Electromagnetic Field Simulation”, Artech House, Boston, 2003, chap. 4, pp. 81–88

[2.38] M.N.O. Sadiku, "Elements of Electromagnetics", New York: Oxford University Press, 3rd ed., 2001.

[2.39] W.B. Kuhn, “Fully integrated bandpass filters for wireless transceivers-problems and promises”, 45th IEEE Midwest Symposium on Circuits and Systems, vol. 2, August. 2002, pp. II-69–II-72.

[2.40] T. Kamgaing, R. Henderson, M. Petras, “Design of RF filters using silicon integrated passive components”, Digest of Papers, IEEE Topical Meeting on Silicon Monolithic Integrated Circuits in RF Systems, September 2004, pp. 33–36.

[2.41] B. Eisener, K. Buyuktas, A. Migemer, H. Kebinger, C. Herzum, “Monolithic, integrated high-Q inductors for RF applications”; Digest of Papers. 2003 Topical Meeting on Silicon Monolithic Integrated Circuits in RF Systems, April 2003, pp. 107–110.

[2.42] O. Andrei, A. Muller, D. Neculoiu, “Electromagnetic design of lumped components filters on high resistivity silicon substrate”, Proceedings, IEEE International Semiconductor Conference, 2004, vol.2, pp. 405–408.

[2.43] W.Y. Yin, L.W. Li, S.J. Pan, Y.B. Gan, “Experimental characterization of on-chip inductor and capacitor interconnect: Part II. Shunt Case”, IEEE Transactions on Magnetics, vol. 40, no. 3, May 2004, pp. 1657–1663.

[2.44] T.O. Dickson, et al., “30-100-GHz Inductors and Transformers for Millimeter-Wave (Bi)CMOS Integrated Circuits”, IEEE Transactions on Microwave Theory and Techniques, vol. 53, no. 1, January 2005, pp. 123–133.

[2.45] Y. Zhuang, M. Vroubel, B. Rejaei, J. N. Burghartz, “Ferromagnetic RF inductors and transformers for standard CMOS/BiCMOS”, IEDM 02. Digest. International Electron Devices Meeting, December 2002, pp. 475–478.

[2.46] J.-W. Lin, C.C. Chen, Y.-T. Cheng, “A Robust High-Q Micromachined RF Inductor for RFIC Applications”, IEEE Transactions on Electron Devices, vol. 52, no. 7, July 2005, pp. 1489–1496.

[2.47] J. Sun, and J. Miao, “High performance MEMS inductors fabricated on localised and planar thick SiO2 layer”, Electronics Letters, vol. 41, no. 7, March, pp. 446–447.

[2.48] J. N. Burghartz, B. Rejaei, and H. Schellevis, “Saddle add-On metallization for RF-IC Technology”, IEEE Transactions on Electron Devices, vol.51, no. 3, March 2004, pp. 460–466.

[2.49] Z. Ma, and Y. Kobayashi, “Miniaturized High-Temperature Superconducting Microstrip and Coplanar Waveguide Filters”, IEICE Tans. Electron., vol.E88-C, no.7, July 2005, pp. 1406–1411.

[2.50] M.V. Jacob, J. Mazierska, S. Takeuchi, “Miniaturized superconducting filter for mobile communications”, TENCON Conference on Convergent Technologies for Asia-Pacific Region, October 2003, vol. 2, pp. 631–634.

[2.51] H. Knaya, K. Kawakami, K. Yoshida, “Design of Miniaturized Superconducting Bandpass Filter by Evaluating the Kinetic Inductance in the K-Inverter”, IEICE Tans. Electron., vol.E89-C, no.2, February 2006, pp. 145–150.

[2.52] H. Kanaya, R. Oba, K. Kawakami, and K. Yoshida, “Miniaturization of superconducting coplanar waveguide bandpass filters by cross coupling”, Institute of Physics Conference Series, vol.181, March 2005, pp.2759–2763.

[2.53] R. Simon, “High-temperature superconductor filter technology breaks new ground”, available at: http://rfdesign.com/images/archive/308RF_Simon28.pdf.

[2.54] R. B. Greed, B. D. Hunt, R. F. Jeffries, D. C. Voyce, “Microwave Applications of High Temperature Superconductors”, GEC REVIEW, vol. 14, no. 2, 1999, pp. 104–114.

[2.55] Jia-Sheng Hong and Eamon P. McErlean, "Narrow-Band HTS filter on Sapphire Substrate," IEEE MTT-S International Microwave Symposium Digest, June 2004, pp. 1105-1108.

[2.56] Chih-Yuan Lee, et al., “A simple systematic spiral inductor design with perfected Q improvement for CMOS RFIC application”, IEEE Transactions on Microwave Theory and Techniques, vol. 53, no. 2, February 2005, pp. 523 – 528.

[2.57] Geert J. Carchon, Walter De Raedt, and Eric Beyne, “Wafer-Level Packaging Technology for High-Q On-Chip Inductors and Transmission Lines”, IEEE Transactions on Microwave Theory and Techniques, vol. 52, no.41, April 2004, pp. 1244–1250.

[2.58] H.J. De Los Santos, “Applications of MEMS technology to RF/microwave systems”, 33rd European Microwave Conference, vol. 3, October 2003, pp. 1439–1442.

[2.59] B. Pillans, G. Rebeiz, J.-B. Lee, “Advances in RF MEMS technology”, 25th IEEE Gallium Arsenide Integrated Circuit (GaAs IC) Symp. Digest, 2003, pp. 17–20.

[2.60] C. T.-C. Nguyen, “High-Q micromechanical oscillators and filters for communications”, Proceedings, IEEE International Symposium on Circuits and Systems, Hong Kong, June 1997, pp. 2825–2828.

[2.61] S. Lucyszyn, “Review of radio frequency microelectromechanical systems technology”, IEE Proceedings- Science, Measurement and Technology, vol. 151, no. 2, March 2004, pp. 93–103.

[2.62] E. Quevy, et. al., “IF MEMS filters for mobile communication”, 8th IEEE Interna-tional Conference on Emerging Technologies and Factory Automation, Proceedings, vol. 2, October 2001, pp. 733–736.

[2.63] L.P.B. Katehi, J.F. Harvey, E. Brown, “MEMS and Si micromachined circuits for high-frequency applications”, IEEE Transactions on Microwave Theory and Techniques, vol. 50, no. 3, March 2002, pp. 858–866.

[2.64] M. G. Allen, “MEMS Technology for the Fabrication of RF Magnetic Components”, IEEE Transaction on Magnetic Components”, vol. 39, no. 5, September 2003, pp. 3073–3078.

[2.65] C.T.-C. Nguyen, “RF MEMS in wireless architectures”, 2005, Proceedings, 42nd Design Automation Conference, June 2005, pp. 416–420.

[2.66] Chen-Yu Chi, Gabriel M. Rebeiz, “Planar Microwave and Millimeter-Wave. Lumped Elements and Coupled-Line Filters Using Micro-Machining Techniques”, IEEE Transactions on Microwave Theory and Techniques, vol. 43, no. 4, April 1995, pp. 730–738.

[2.67] H. J. De Los Santos, “On the Ultimate Limits of IC Inductors — An RF MEMS Perspective”, Proceedings of the 52nd IEEE Electronic Components and Technology Conference, May 2002.

[2.68] T. Gryba, A. Haddou, V. Sadaune, V. Zhang, J.E. Lefebvre, E. Doghech, E. Cattan, D. Remiens, “Integration of RF filters on GaAs substrate”, IEEE Ultrasonics Symposium, vol. 1, October 2001, pp. 57–60.

[2.69] P. T. M. van Zeijl, J. H. Visser, and L. K. Nanver, “FM Radio Receiver Front-End Circuitry with On-Chip SAW Filters”, IEEE Trans. on Consumer Electronics, vol. 35, no. 3, August 1989, pp. 512–519.

[2.70] J.F. Carpentier et al. “A SiGe:C BiCMOS WCDMA Zero-IF RF Front-End Using an Above-IC BAW Filter”, 2005 IEEE International Solid-State Circuits Conference, Februar 2005, pp. 394–395.

[2.71] H.P. Loebl, et. al., “Narrow Band Bulk Acoustic Wave Filters”, 2004 IEEE International Ultrasonics, Ferroelectrics, and Frequency Control Joint 50th Anniversary Conference, October 2004, pp. 411–415.

[2.72] R. Aigner, et al. “Bulk-acoustic-wave filters: performance optimization and volume manufacturing”, IEEE MTT-S International Microwave Symposium Digest, vol. 3, June 2003, pp. 2001–2004.

[2.73] P. Ancey, G.Bouche, “System Integration of BAW filters”, MEMSWAVE 2004 Conference, June 2004, Upsala, Available at: http://www.isen.fr/martina/pages/publications.html.

[2.74] Chunbing Guo, et al., “A fully integrated 900-MHz CMOS wireless receiver with on-chip RF and IF filters and 79-dB image rejection”, IEEE Journal of Solid-State Circuits, vol. 37, no. 8, August 2002, pp. 1084–1089.

[2.75] P. Andreani, S.Mattisson, “A CMOS gm-C IF filter for Bluetooth”, Proceedings of the IEEE 2000 Custom Integrated Circuits Conference, May 2000, pp. 391–394.

[2.76] Xin He, W.B. Kuhn, “A 2.5-GHz low-power, high dynamic range, self-tuned Q-enhanced LC filter in SOI”, IEEE Journal of Solid-State Circuits, vol. 40, no.8, August 2005, pp. 1618–1628.

[2.77] Shengyuan Li, S. Sengupta, H. Dinc, P.E. Allen, “CMOS High-Linear Wide-Dynamic Range RF On-Chip Filters Using Q-enhanced LC Filters” IEEE International Symposium on Circuits and Systems, May 2005, pp. 5942–5945.

[2.78] T. Soorapanth, S.S. Wong, “A 0-dB IL 2140±30 MHz bandpass filter utilizing Q-enhanced spiral inductors in standard CMOS”, IEEE Journal of Solid-State Circuits, vol. 37, no. 5, May 2002, pp. 579–586.

[2.79] Xin He, W.B. Kuhn, “A fully integrated Q-enhanced LC filter with 6 dB noise figure at 2.5 GHz in SOI”, IEEE Radio Frequency Integrated Circuits (RFIC) Symposium, June 2004, pp. 643–646.

[2.80] W.B. Kuhn, D. Nobbe, D. Kelly, A.W. Orsborn, “Dynamic range performance of on-chip RF bandpass filters”, IEEE Transactions on Circuits and Systems II: Analog and Digital Signal Processing, vol. 50, no. 10, October 2003, pp. 685–694.

[2.81] A.N. Mohieldin, E. Sanchez-Sinencio, J. Silva-Martinez, “A 2.7-V 1.8-GHz fourth-order tunable LC bandpass filter based on emulation of magnetically coupled resonators”, IEEE Journal of Solid-State Circuits, vol. 38, no. 7, July 2003, pp. 1172–1181.

[2.82] W.B. Kuhn, N.K. Yanduru, A.S.Wyszynski, “Q-enhanced LC bandpass filters for integrated wireless applications”, IEEE Transactions on Microwave Theory and Techniques, vol. 46, no. 12, Part 2, December 1998, pp. 2577–2586.

[2.83] A.N. Mohieldin, E. Sanchez-Sinencio, J. Silva-Martinez, “Design considerations of bandpass LC filters for RF applications”, 45th IEEE Midwest Symposium on Circuits and Systems, vol. 2, August 2002, pp. II-73–II-76.

[2.84] D. Li, Y.Tsividis, “Active LC filters on silicon”, IEE Proceedings Circuits, Devices and Systems, vol. 147, no. 1, February 2000, pp. 49–56.

[2.85] R. Tumala, “Fundamental of Microsystems Packaging”, McGraw-Hill, New York, 2000, chap. 8, pp. 315-333.

[2.86] V. Palazzari, et. al., “Design of an asymmetrical dual-band WLAN filter in liquid crystal polymer (LCP) system-on-package technology”, IEEE Microwave and Wireless Components Letters, vol. 15, no. 3, March 2005, pp. 165–167.

[2.87] Mekita F. Davis, et. al., “Integrated RF Architectures in Fully-Organic SOP Technology”, IEEE Transaction on Advanced Packaging, vol. 25, no. 2, May 2002, pp. 136–142.

[2.88] Sidharth Dalmia, Sung Hwan Min, Seock-Hee Lee, Venky Sundaram and Madhavan Swaminathan, “Design and Optimization of Embedded RF Filters using a Hybrid Approach”, IEEE RAWCON Conference, August 2001, pp. 145–148.

[2.89] S. Dalmia, V. Sundaram, G. White, M. Swaminathan, “Liquid crystalline polymer (LCP) based lumped-element bandpass filters for multiple wireless applications”, IEEE MTT-S International Microwave Symposium Digest, vol. 3, June 2004, pp. 1991–1994.

[2.90] Souvik Mukherjee, Bhyrav Mutnury, Sidharth Dalmia, and Madhavan Swaminathan, “Layout-Level Synthesis of RF Inductors and Filters in LCP Substrates for Wi-Fi Applications”, IEEE Transaction on Microwave Theory and Techniques, vol. 53, no. 6, June 2005, pp. 2196–2210.

[2.91] Min-Hung WENG, Cheng-Yuan HUNG, and Hung-Wei WU, “Fabrication of an X-Band Dual Mode Bandpass Filter Using Low Cost FR4 Substrate”, IEICE Trans. Electron., vol. E88–C, vo. 1, January 2005, pp. 143–145.

[2.92] Gye-An Lee, M. Megahed, F. De Flaviis, “Design and analysis of novel compact inductor resonator filter”, 2002 IEEE MTT-S International Microwave Symposium Digest, vol. 3, June 2002, pp. 1621–1624.

[2.93] Gye-An Lee, M. Megahed, F. De Flaviis, “Design of multilayer spiral inductor resonator filter and diplexer for system-in-a-package”, 2003 IEEE MTT-S International Microwave Symposium Digest, vol. 1, June 2003, pp. 527–530.

[2.94] Gye-An Lee; Megahed, M.A.; De Flaviis, F.; “Low-cost compact spiral inductor resonator filters for system-in-a-package”, Advanced Packaging, IEEE Transactions on [see also Components, Packaging and Manufacturing Technology, Part B: Advanced Packaging, IEEE Transactions on], vol. 28, no. 4, November 2005, pp. 761–771.

[2.95] M.-L. Chuang, “Concurrent dual band filter using single set of microstrip open-loop resonators”, Electronics Letters, vol. 41, no. 18, September 2005, pp. 1013–1014.

[2.96] University of Oulu, FINLAND, September 1999, available at:

http://www.infotech.oulu.fi/GraduateSchool/LSeries/1999/LS99_06.html.

[2.97] Cheng-Chung Chen; “Dual-band bandpass filter using coupled resonator pairs”, IEEE Microwave and Wireless Components Letters, vol. 15, no. 4, April 2005, pp. 259–261.

[2.98] A.A.A. Apriyana, Z. Y. Ping; “A dual-band BPF for concurrent dual-band wireless transceiver”, 5th (EPTC 2003) Electronics Packaging Technology Conference, December 2003, pp. 145–149.

[2.99] H. Miyake, S. Kitazawa, T. Ishizaki, T. Yamada, and Y. Nagatomi, “A miniaturized monolithic dual band filter using ceramic lamination technique for dual mode portable tele-phones”, IEEE MTT-S Digest, pp. 789–792.

[2.100] Wing-Yan Leung; Cheng, K.-K.M.; Ke-Li Wu; “Multilayer LTCC bandpass filter design with enhanced stopband characteristics”, IEEE Microwave and Wireless Components Letters, vol. 12, no. 7, July 2002, pp. 240–242.

[2.101] Young-Joon Ko, et. al., “A miniaturized LTCC multi-layered front-end module for dual band WLAN (802.11 a/b/g) applications”, 2004 IEEE MTT-S International Microwave Symposium Digest, vol. 2, pp. 563–566.

[2.102] Yasir Amin, Xinzhong Duo, Li-Rong Zheng, Hannu Tenhunen, “Integration of Passives for receiver front end of 5GHz wireless LAN Applications” National Conference on Emerging Technologies (NCET 2004), December 2004, pp. 24–29.

[2.103] K. Zoschke, J. Wolf, M. Topper, O. Ehrmann, T. Fritzsch, , K. Scherpinski, H. Reichl, F.-J. Schmuckle, “Thin film integration of passives - single components, filters, integrated passive devices”, ECTC 04. Electronic Components and Technology Conference, Proceedings, vol. 1, June 2004, pp. 294–301.

[2.104] G. Prigent, et. al., “Design of narrow-band DBR planar filters in Si-BCB technology for millimeter-wave applications”, IEEE Transactions on Microwave Theory and Techniques, vol. 52, no. 3, March 2004, pp. 1045–1051.

[2.105] C. Quendo, E. Rius, Y. Clavet, C. Person, F. Bouchriha, L. Bary, K. Grenier, “Miniaturized and out-of-band improved bandpass filter in Si-BCB technology”, 2004 IEEE MTT-S International Microwave Symposium Digest, vol. 3, June 2004, pp. 1475–1478.

[2.106] J. Hartung, “Integrated passive components in MCM-Si technology and their applications in RF-systems”, 1998 7th International Conference on Multichip Modules and High Density Packaging, Proceedings, April 1998, pp. 256–261.

[3.1] G. L. Matthaei, L. Young, and E. M. T. Jones, “Microwave Filters, Impedance-Matching Networks and Coupling Structures”, Artech House, Norwood, MA, 1980.

[3.2] Wai-Kai Chen, “Passive and Active Filters: Theory and Implementations”, John Wiley & Sons, March 1986, chap. 2.

[3.3] Jia-Sheng Hong and M. J. Lancaster, “Microstrip Filter for RF/Microwave Applications”, Wiley, New York, 2001.

[3.4] Ralph Levy, Richard V. Snyder, and George Matthaei, “Design of Microwave Filters”, IEEE Transactions on Microwave Theory and Techniques, vol. 50, no. 3, March 2002, pp. 783–793.

[3.5] Rogers Corporation, “Rogers High Frequency Circuit Materials Data Sheet”, 2006, available at: www.rogerscorporation.com.

[3.6] www.isola.de.

[4.1] Leo G. Maloratsky, “Reviewing The Basics Of Microstrip Lines”, Microwave & RF Journal, vol. 39, no. 3, March 2000, pp. 78-88, available at: http://www.cadoe.com/industries/mems/mems-downloads/maloratsky_micostrip.pdf

[4.2]. E. Belohoubek, and E. Denlinger, “Loss Considerations for Microstrip Resonators ”, IEEE Transactions on Microwave Theory and Techniques, June 1975, vol. 23, no. 6, pp. 522- 526

[4.3] David Pozar, “Microwave Engineering,” 2nd Ed., John Wiley and Sons, 1998, chap 3, pp. 163

[4.4]. R. K. Ulrich, W. D. Brown, “Advanced Electronic Packaging, 2nd Edition”, Wiley-IEEE Press, May 2006, chap. 4

[4.5] C. A. Balanis, "Advanced Engineering Electromagnetics”, Wiley, USA, 1989, chap.8

[4.6] WiMAX Forum, available at: www.wimaxforum.org

[5.1]. S. Wartenberg, “RF Measurements of Die and Packages”, Artech House, 2002.

[5.2] L. Martens, “High-Frequency Characterization of Electronic Packaging”, Kluwer Academic Publishers, 1998.

[5.3] A. J. Lord, “Comparing the Accuracy and Repeatability of On-Wafer Calibration Techniques to 110 GHz”, Cascade Microtech Application Note.

[5.4] A. M. E. Safwat, L. Hayden, “Sensitivity Analysis of Calibration Standards for SOLT and LRRM”, 58th ARFTG Conference Digest-Fall, November 2001, vol. 40, pp. 1-10.

[5.5]. Cascade Microtech Inc., "Layout rules for GHz-probing," Application Note, 1988.

[5.6]. D. Ballo, “Network Analyzer Basics”, Hewlett-Packard Company, 1998.

[5.7]. M. Farina, and T. Rozzi, “A short-open deembedding technique for method-of-moments-basedelectromagnetic analyses” IEEE Transactions on Microwave Theory and Techniques, vol. 49, no. 4, April 2001, pp. 624 – 628.

[5.8] J. Song, et al., “De-embedding and EM Simulations for Microstrip over Lossy Silicon”, IEEE International Symposium on Antennas and Propagation Society, vol. 3, June 2003, pp. 973–976.

Published Papers

[1] M. Baba, S. Guttowski, H. Reichl, “An Efficient Methodology for Design and Implementation of Embedded Bandpass Filters for RF/Wireless Applications”, accepted for the 9th International IEEE EPTC Conference, Singapore, 10th – 12th December 2007.

[2] M. Baba, S. Guttowski, H. Reichl, “A Design Approach for the Miniaturization of Embedded RF Filters for System-in-Package (SiP) Applications”, IMAPS Advanced Technology Workshop on Integrated/Embedded Passives, San Jose, CA, USA, 15th − 16th November, 2007.

[3] M. Baba, W. Klein, W. Riedl, W. John, H. Reichl, “Impact of Illumination on the Behavior of On-Chip Inductor during RF Measurements”, 5th International Workshop on Electromagnetic Compatibility of Integrated Circuits, Munich, Germany, November 2005, pp. 261-264.

[4] G. Sommer, M. Petras, M. Baba, F. Salhi, S. Korf, G. Fotheringham, R. Henderson, W. Blood, L-T. Hwang, R. Croswell, R. Lempkowski, J. Savic, M. Miller, W. John, H. Reichl, “Development of a Design Library for Embedded Passive RF Components in HDI Organic Substrate Material“, IEEE International Symposium on Electromagnetic Compatibility, Vol. 2, May 2003, pp. 852–855.

Biographical Sketch

Personal Data:

First Name: Mohamadou

Family Name: Baba

Date of Birth: 16. July 1972

Place of Birth: Douala, Cameroon

Status: Single

Education:

10/1993 – 10/2000: Electrical engineering at the Technische Universität (TU) Berlin, Germany

Degree Obtained: Diplom-Ingenieur

Specialization: Microelectronics

Thesis: „Messtechnische Charakterisierung von gesputterten Aluminium-Kontakten auf Silizium“ (Advisor: Professor Wagemann).

Work Experience:

10/ 2000 – 04/ 2001: Research Engineer at the TU Berlin, Germany.

Since 04/2001: Research Engineer at the Fraunhofer Institute for Reliability and Microintegration (FhG-IZM) in Berlin, Germany (Supervisor: Professor Reichl).